UNIVERSITÀ DI PISA

DIPARTIMENTO DI INGEGNERIA CIVILE E INDUSTRIALE

Master's degree in Materials and Nanotechnology

Supercurrent manipulation in InSb nanoflag-based Josephson Junctions by Scanning Gate Microscopy

Relatore:

Prof. Stefan Heun

Prof. Lucia Sorba

Candidato:

Antonio Lombardi

ANNO ACCADEMICO 2023/2024

[November 22, 2024 at 16:53 – version 1]

ABSTRACT

In this Master's thesis work we report the first Scanning Gate Microscopy experiments on superconducting weak links, demonstrating the possibility of manipulating the supercurrent flow across a semiconductor-superconductor heterostructure through the charged tip of an atomic force microscope at a local level. To this end, we have employed a new generation of Nb-contacted ballistic InSb nanoflag-based Josephson junctions. We performed a full magneto-transport characterization of these devices at 300 mK. Fully gate-tunable Josephson effect as well as larger switching currents with respect to the previous Nb/Ti contact design have been observed. Furthermore, we report evidence of fully developed Fraunhofer side lobes, as well as observation of Multiple Andreev Reflections, demonstrating the high transparency of the superconductor/semiconductor interfaces. Scanning Gate Microscopy measurements on superconducting junctions clearly show tip-induced modulation of critical current due to the local charge carrier depletion of the semiconducting region. Our experimental findings are consistent with theoretical simulations and establish a new way of investigating the behavior of superconducting weak links, with a view to supercurrent flow imaging and local investigation of topological samples.

ACKNOWLEDGEMENTS

I would like to thank my supervisors, Prof. Stefan Heun and Prof. Lucia Sorba, for their continuous support during this year-long journey. Dear Stefan, thank you for your attention to details, patience and perseverance: you taught me how much these qualities are fundamental in our field.
I am thankful to Dr. Sedighe Salimian, Dr. Gaurav Shukla, and Dr. Giada Bucci for their fundamental contributions to device fabrication, as well as Prof. Lucia Sorba and Dr. Valentina Zannier for growing the InSb nanoflags: this thesis work would not have been possible without your help. Thanks should also go to Dr. Sergio Pezzini and Dr. Stefano Veronesi for their support during my experimental activities, and to Dr. Matteo Carrega for useful discussions, theoretical support and for having reviewed this manuscript. I would also like to thank Dr. Giorgio De Simoni for letting me borrow instrumentation that has been fundamental for the SGM measurements.
Finally, I would like to thank Dr. Ivan Villani, Dr. Matteo Pioldi, and Dr. Andrea Chieppa, my lab-mates during this journey.

CONTENTS

1 INTRODUCTION

Modern electronics is based on a component, the field effect transistor (FET), which behaves as a voltage-operated valve for electrical currents. This is made possible by the fundamental property of semiconductor-based devices: the capacity of tuning their charge carrier density and, therefore, their electrical resistance by changing the voltage applied to control electrodes called gates.
FET-based technology permeates our every day life in the form of laptops and smartphones, in addition to being crucial for industrial applications and scientific research. However, with the ever increasing request for more computational power, this paradigm is facing its limitations in terms of energy dissipation and communication speed. For this reason, several companies and research groups are focused on experimenting alternative routes, such as superconducting electronics [1].
Superconductors are materials that, under specific conditions, let electrical currents flow through them without energy dissipation (supercurrents), making them ideal platforms for the development of high-speed and low-dissipation devices for classical computation. Furthermore, they display quantum behaviour at a macroscopic scale: since the dawn of the second quantum revolution, superconductor-based designs are among the frontrunners in the development of quantum technologies [2].
The possibility to integrate superconductivity into conventional semiconductor-based architectures is of pivotal importance to retain the advantages of both approaches. This led to the rise of superconductor-semiconductor hybrid devices, the most common of which is the superconducting weak link [3]. This consists in a junction between two superconducting leads that are put electrically in contact through a semiconducting region. The influence of the leads induces the device to acquire superconducting properties, making it possible for a supercurrent to flow through the junction. On the other hand, such dissipationless flow can be completely suppressed by depleting the semiconducting region from charge carriers through gating. This way, it is possible to obtain the Josephson Field Effect Transistor (JoFET), which acts as a voltage-operated valve for supercurrents, that is the equivalent of the FET for superconducting electronics.
The study of superconducting weak links is the object of a branch of solid state physics that has been prolific in the last two decades. Nevertheless, novel ways of characterizing and controlling these systems still have to be investigated. In particular, their limited size makes collecting information about their local electrical behaviour a daunting task.
A new generation of planar superconducting weak links, where semiconducting regions remain exposed, open up the possibility of manipulating the device via local gating by Scanning Gate Microscopy (SGM) [4]. This technique, which consists in scanning semiconducting regions with an electrically polarized tip, has been widely used on non-superconducting devices to investigate electrical current flow at a local level. In fact, the tip acts as a local gate, which can deplete the

semiconducting region beneath it from charge carriers, effectively preventing the flow of electrical current within said region. In the same way, such local gate can suppress the supercurrent flow across a superconducting weak link; however, so far no research group had experimentally investigated this possibility.
In this work we present the first Scanning Gate Microscopy measurements performed on superconducting weak links, demonstrating the potentiality of a currently unexplored way to study the behaviour of hybrid systems at a local level.
To this end, we have employed junctions based on a planar indium antimonide (InSb) nanostructure, the *nanoflag*, which has proven to be an excellent platform to obtain transparent semiconductor-superconductor interfaces [5].
During this thesis, we have fully characterized the behaviour of a new generation of Nb-contacted InSb nanoflag-based devices by electrical transport experiments in the superconducting regime, confirming their state-of-the-art quality. Next, after having optimized the relative measurements protocol, we performed SGM experiments on nanoflag-based devices in the normal regime, unveiling the potentialities of the technique as a diagnostic tool to visualize defects in these nanostructures. Finally, we acquired the first SGM measurements in the superconducting regime, leading to the observation of clear tip-induced manipulation of the superconducting behaviour of the sample.
This thesis was carried out at the NEST Laboratory, under the supervision of Prof. Stefan Heun from CNR-Instituto Nanoscienze. SGM measurements were carried out in a dedicated setup made available by Scuola Normale Superiore. InSb nanoflags were grown by the group of Prof. Lucia Sorba. This thesis is organized as follows:

Chapter 2 theoretical introduction on the physics of superconducting weak links;

Chapter 3 discussion of the state of the art of InSb-based nanostructures and Scanning Gate Microscopy;

Chapter 4 description of device fabrication, experimental apparatus and measurement techniques;

Chapter 5 experimental result of conventional electrical transport experiment on InSb nanoflag-based junctions;

Chapter 6 experimental results of Scanning Gate Microscopy experiments, including tip-induced supercurrent modulation;

Chapter 7 concluding remarks on the thesis work and an outlook on future developments.

2 THEORY OF SUPERCONDUCTIVITY

2.1 INTRODUCTION

Superconductivity and its applications

Superconductivity is an effect that takes place in a wide range of materials spanning from common metals like aluminium or niobium to advanced ceramics like cuprates [6]. Although the nature of the underlying mechanism can differ from case to case, all of these materials share the same behaviour:

- perfect diamagnetism;
- dissipationless electrical transport;
- said characteristics are present up to a critical temperature and are suppressed in presence of a sufficiently intense magnetic field.

This phenomenology was first discovered by Heike Kamerlingh Onnes [6] in 1911, who received a Nobel prize for it in just two years time: sign of the immediate recognition of a discovery that would have influenced both scientific research and industrial applications for the years to come.
For instance, the possibility of having large electrical currents flowing witout dissipation inside of metal coils allowed advancements in fields ranging from experimental physics (e.g. particle accelerators) to analytical chemistry (nuclear magnetic resonance), from medical to transportation applications.
However, this is just scratching the surface of the set of possibilities that superconductors provide: there is a lot more than just dissipationless transport. To better understand, it is necessary to dive into the real nature of superconductivity: quantum mechanics.
Superconductivity is an intrinsically quantum phenomenon, i.e., it can be explained only by taking quantum correlation effects into account. Its key feature is the so-called macroscopic quantum phase coherence, that is the display of quantum interference effects at a macroscopic level.
In the last century researchers learnt to harness these quantum properties for technological applications ranging from sensors (bolometers, SQUID magnetometers...) to quantum computation (superconducting QuBits).
What's more, superconductors can be used to induce correlations (and therefore superconductor-like properties) into other materials placed in contact with them thanks to the superconducting proximity effect (whose schematic visualization is displayed in Fig. 1).
One of the most promising ways of engineering quantum devices is the design of Superconductor-Semiconductor heterostructures [8], which combine the quantum correlations of the superconductor with the possibility of tuning the behaviour of the semiconductor by field effect like in the conventional field effect transistor (FET),

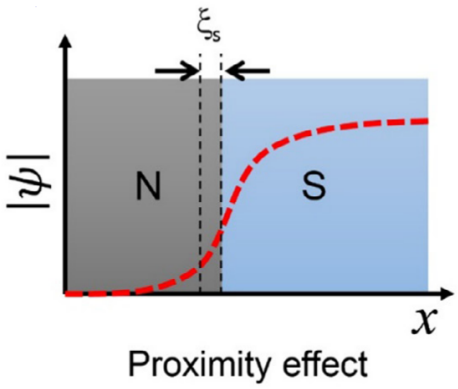

Figure 1: Visual representation of the superconducting proximity effect: the superconducting order parameter Ψ (indicated by the red line) penetrates across a normal(N)-superconductor(S) interface inducing correlations into the neighbouring material. The typical penetration length is labelled as ξ_s. Adapted form [7].

the basis of modern electronics.
The possibility of having a voltage-operated tuning knob makes such devices integrable into existing conventional electronics architectures, paving the way to their upcoming step into the commercial applications world.
However, in order to produce a working quantum device, we must be able to select suitable semiconductor-based platforms, clean enough to preserve the superconductor-induced correlations.

2.2 FUNDAMENTALS OF SUPERCONDUCTIVITY

Diving into the details of the microscopic mechanisms that can explain superconductivity goes far beyond the scope of this thesis project; however, in order to understand the physics behind the system under study, it is essential to review the main theoretical results in the history of research into this subject. The contents of this section is an adaptation of the following references: [3, 6, 9]

2.2.1 *Ginzburg-Landau theory*

The first theory able to describe superconductivity was presented by Landau and Ginzburg in 1950 [10]. Although it is based on a purely phenomenological approach (i.e. it is not based on first principles), it is still considered one of the most versatile frameworks available due to the fact that it is based on an extremely limited set of widely general assumptions.

- The thermodynamics of the system is fully described by its free energy F, which depends on the system's temperature T but also on a quantity called order parameter $\psi(\vec{x})$ that describes the correlations in the system.
- $\psi(\vec{x})$ is close to zero. Therefore, we can consider a perturbation expansion of the free energy in $\psi(\vec{x})$.

$$F(\psi, T) = \int d\vec{x} \left[a(T)|\psi(\vec{x})|^2 + b(T)|\psi(\vec{x})|^4 + ... \right]. \tag{1}$$

The system in thermodynamic equilibrium minimizes its free energy.

- There is a critical temperature T_c above which $\psi = 0$ is the global minimum of the free energy. However, below T_c this single global minimum splits into many and $\psi = 0$ does not correspond to the thermodynamic equilibrium configuration anymore. This can be expressed by the following conditions on the free energy parameters a and b (Eq. (1)):

$$\begin{cases} a(T) \geqslant 0 & T \geqslant T_c \\ a(T) \leqslant 0 & T \leqslant T_c \\ b(T) > 0 & \forall\, T \end{cases} . \tag{2}$$

This phenomenological theory is able to describe efficiently every system close to a phase transition which involves the creation of correlation: not only superconductivity, but also ferromagnetism and ferroelectricity. In the latter systems, the identification of the correlations and of the corresponding order parameter is straightforward: a ferromagnetic system is the more ordered, the more it is magnetized. Therefore, its order parameter is naturally its magnetization.
But what is the order parameter for a superconducting phase transition? The key insight of Landau and Ginzburg is acknowledging the quantum nature of superconductivity and interpreting the supercurrent stream as the coherent flow of charge carriers.
Their idea is to use a "wavefunction-like" (not normalized) complex order parameter $\Psi(\vec{x})$, that can be interpreted as the wavefunction of the charge carriers[1] the supercurrent is constituted of. In particular, we can rewrite $\Psi(\vec{x}) = \sqrt{n(\vec{x})}e^{\phi(\vec{x})}$, where we define $n(\vec{x})$ as the superconducting charge carrier density and $\phi(\vec{x})$ as a new quantity called superconducting phase, whose manipulation is the key of superconducting devices engineering.
Applying elementary quantum mechanics theorems it is possible to obtain the following equation for the charge current density associated to a state with wavefunction $\Psi(\vec{x})$, the second Ginzburg Landau equation:

$$\vec{J}(\vec{x}) = \frac{q}{2mi}\left(\hbar\Psi^\star(\vec{x})\,\vec{\nabla}\Psi(\vec{x}) - \hbar\Psi(\vec{x})\,\vec{\nabla}\Psi^\star(\vec{x}) - 2qi|\Psi|^2\vec{A}(\vec{x})\right) \tag{3}$$

where $\vec{A}(\vec{x})$ is the magnetic vector potential in the system, i is the imaginary unit, and m and q are respectively the mass and the charge of a single superconducting charge carrier.
This relation, alongside the first Ginzburg Landau equation

$$a(T)\psi(\vec{x}) + b(T)\psi(\vec{x})\,|\psi(\vec{x})|^2 + \frac{1}{2m}\left(-i\hbar\vec{\nabla} - q\vec{A}(\vec{x})\right)^2\psi(\vec{x}) = 0 \tag{4}$$

and Maxwell's equations completely describe the behaviour of the system at a temperature T immersed in an external magnetic field $\vec{B}$.
The previous equations Eq. (3) and Eq. (4) allow a finite current density to be

1 Electrons are fermions, but this phenomenological approach does not take fermion statistics (Pauli's principle) into account; however, this does not create issues because we will find out that isolated electrons are not the charge carriers responsible for supercurrent.

present inside the system. Since we are at thermodynamic equilibrium, there cannot be dissipation due to this current density: this model can therefore describe supercurrent. In particular, Eq. (3) can be rewritten in the following form

$$\vec{J}(\vec{x}) = \frac{q}{m}\left(\hbar n(\vec{x})\,\vec{\nabla}\phi(\vec{x}) - q n(\vec{x})\,\vec{A}(\vec{x})\right), \tag{5}$$

which states that there is a finite supercurrent in absence of magnetic fields whenever the complex phase of the superconducting order parameter is not uniform in the system.
Despite its terrific power in describing real physical systems in which superconductivity is present, this model cannot explain the underlying microscopic processes from where superconductivity stems out. We therefore must take a step further and introduce BCS theory.

2.2.2 *BCS theory*

Bardeen, Cooper and Schrieffer in 1957 were finally able to explain superconductivity in 3D bulk metallic materials from first principles [11].
The main idea introduced by BCS is the concept of Cooper pairs: they noticed that, in presence of an attractive interaction between electrons described by the following Hamiltonian[2]

$$H = \sum_{\vec{k},\sigma} \varepsilon_{\vec{k},\sigma} c^{\dagger}_{\vec{k},\sigma} c_{\vec{k},\sigma} + \sum_{\vec{k},\vec{l}} V_{\vec{k}\vec{l}} c^{\dagger}_{\vec{k},\uparrow} c^{\dagger}_{-\vec{k},\downarrow} c_{-\vec{l},\downarrow} c_{\vec{l},\uparrow}, \tag{6}$$

the non-interacting electronic ground state (the familiar Fermi sphere) is unstable under the formation of bound states between pairs of electrons close to the Fermi energy with opposite momenta and spins. One astonishing feature of this prediction is that, at zero temperature, these bound state are energetically convenient independently of the strength of the attractive interaction, i.e., this phenomenon cannot be described via a perturbation theory approach.
But what is the source of this attractive interaction? Bardeen, Cooper, and Schrieffer identify it as low-temperature electron-phonon coupling: electrons induce deformations in the crystal lattice, forming a region of positive charge density in the trail of their path, which can interact with other electrons generating an attractive interaction between charge carriers.
Explaining BCS theory in a thorough way would imply to describe a lot of clever assumptions and cumbersome calculations that go well beyond the scope of this experimental work. I will just report its main results:

- The ground state of the system is described as a condensate of Cooper pairs;
- The Hamiltonian of the system close to its ground state can be approximated up to a global energy shift with the following Hamiltonian

$$H_{BCS} = \sum_{\vec{k},\sigma} \xi_{\vec{k},\sigma} c^{\dagger}_{\vec{k},\sigma} c_{\vec{k},\sigma} + \sum_{\vec{k}} \left(\Delta c^{\dagger}_{\vec{k},\uparrow} c^{\dagger}_{-\vec{k},\downarrow} + \Delta^{\star} c^{\dagger}_{-\vec{k},\downarrow} c^{\dagger}_{\vec{k},\uparrow}\right), \tag{7}$$

2 Here $c_{\vec{k},\sigma}$ and $c^{\dagger}_{\vec{k},\sigma}$ are the electronic plane wave of momentum $\vec{k}$ and spin σ destruction and creation operators in the second quantisation formalism. The first summation is the non-interacting electron Hamiltonian and the second describes the particle interactions.

where $\xi_{\vec{k},\sigma}$ is the energy of a free electron referred to the chemical potential of the system and Δ is a temperature-dependent quantity that describes the superconducting state. The system is not superconducting when Δ is zero;

- There is an energy gap between the ground state and the excitation spectrum of the system, which is equal to Δ; in particular, the excited states of the system can be interpreted in a single particle framework as coherent superpositions of electrons and holes.

- This theory is able to describe the presence of a critical temperature and the diamagnetic behaviour of superconductors. In particular, the critical temperature T_c of the system is connected to the zero temperature energy gap Δ_0 by the relation
$$\Delta_0 = \frac{\pi k_B T_c}{e^\gamma} \tag{8}$$
where Gamma is the Euler constant, $\gamma \approx 0.577$.

However, this formalism only describes the behaviour of isotropic and homogeneous bulk materials; in order to be able to explain supercurrent flow and other interesting phenomena we must take a step further and introduce the results of the work of Bogolyubov and De Gennes.

2.2.3 *Bogolyubov-De Gennes equations*

Real systems are not homogeneous nor infinite: Bogoliubov and De Gennes were able to develop a way to decline BCS theory in realistic situations [9].
The main idea of their approach consists in treating the phonon-mediated electron-electron interactions in mean field approximation, by assuming that every electron feels only an effective potential obtained by averaging the interactions with the other carriers over the ground state of the system. In particular, by assuming that the superconducting pairing is due to a short range "pointlike" interaction, this approach can describe also the boundaries and interfaces between superconducting and non-superconducting materials.
This results in the Bogolyubov-De Gennes equations[3]

$$E\Psi(\vec{x}) = \begin{pmatrix} H_e(\vec{x}) & \Delta(\vec{x}) \\ \Delta^\star(\vec{x}) & H_h(\vec{x}) \end{pmatrix} \Psi(\vec{x}). \tag{9}$$

which are Schroedinger equations for the quasiparticles that correspond to the excited states of the system. The electron Hamiltonian H_e is the single particle Hamiltonian for the electrons in the system, including their kinetic energy and the electrostatic interactions with their environment.[4] Differently from plain BCS

3 These equations are expressed in a useful, but redundant, notation by describing the coherent superposition of a hole and electron state as a two dimensional spinor whose first component is the electron wave function and the second is the hole wave function $\Psi(\vec{x}) = \begin{pmatrix} u(\vec{x}) \\ v(\vec{x}) \end{pmatrix}$. The excitation spectrum of the system is described by just the positive eigenvalues of the equations.

4 The hole Hamiltonian is equal to $H_h(\vec{x}) = -H_e^\star(\vec{x})$, being a hole nothing other than the time-reversed absence of an electron.

theory, in the BdG equations Δ is position-dependent and must be derived in a self-consistent way[5] taking into account not only the temperature and the local strength of the attractive electron-electron interaction in the system, but $H_e(\vec{x})$ as well.
These equations, derived from the microscopic theory, provide a much more complicated way to study superconducting systems compared to the macroscopic Ginzburg-Landau theory: what is the connection between the two?
Gorkov in 1959 [12] was able to demonstrate that the Ginzburg-Landau equations can be derived from the BdG equations by assuming $\Delta(\vec{x})$ to be small with respect to the thermal energy $k_B T$ of the system and linearizing its self-consistency equation.
This leads to the following results:

- $\Delta(\vec{x}) = k\Psi(\vec{x})$ is the superconducting order parameter described by the G-L equations up to a dimensional constant.
- The G-L equations are able to describe the macroscopic behaviour of a superconducting system close to its critical temperature in a way consistent with the microscopic theory, which can be used to derive the phenomenological parameters of the macroscopic theory: in particular superconducting charge carriers are identified with Cooper pairs and therefore $q = -2e$.
- If the superconducting pairing potential $\Delta(\vec{x})$ possesses a position-dependent complex phase, then a supercurrent is present in the system.

2.2.4 *Characteristic length scales*

In order to be able to study superconducting heterostructures, it is essential to know how to describe the physics at the interface between a superconductor and another material.
To begin with, let us have a look at Eq. (4) and let us define $\Psi_\infty = \sqrt{\frac{a(T)}{b(T)}}$ as the equilibrium value of the superconducting order parameter at temperature T in an homogeneous bulk material in absence of external magnetic fields. By considering the equation for the adimensional quantity $f(\vec{x}) = \frac{\Psi(\vec{x})}{\Psi_\infty}$ we obtain

$$\xi^2 \nabla^2 f + \left(1 - \xi^2 \left(\frac{2\pi}{\Phi_0}\right)^2 \left|\vec{A}\right|^2\right) f - f|f|^2 = 0, \tag{10}$$

here $\Phi_0 = \frac{h}{2e}$ is the superconducting magnetic flux quantum and $\xi = \sqrt{\frac{\hbar^2}{2m|a(T)|}}$ is a typical length scale of the system: the Superconducting Coherence Length.[6] This length scale has two possible interpretations:

- At the interface between a superconductor and an insulating material, it corresponds to the typical distance that takes $f(\vec{x})$ to vary from zero to one. In other words, that is the distance that separates a completely uncorrelated region from the bulk of the superconductor (see Fig. 1).

5 The self-consistent derivation is necessary since the ground state of the system depends on $\Delta(\vec{x})$ and vice versa.

6 In other references, ξ is defined as $\xi = \sqrt{\frac{\hbar^2}{4m|a(T)|}}$, but it is just conventional.

- BCS theory predicts that this length corresponds to $\xi = \frac{\hbar v_F}{\pi \Delta}$, where v_F is the Fermi velocity of the material; this quantity can be interpreted as the typical dimension of a Cooper pair.

By performing the same trick on Eq. (3) we obtain [7]

$$\vec{\nabla} \times \vec{\nabla} \times \vec{A} = \frac{\Phi_0}{4\pi\lambda^2} \left(f^\star(\vec{x}) \vec{\nabla} f(\vec{x}) - f(\vec{x}) \vec{\nabla} f^\star(\vec{x}) \right) - \frac{1}{\lambda^2} |f|^2 \vec{A}(\vec{x}) \tag{11}$$

where $\lambda = \sqrt{\frac{m \mu_0 \Phi_\infty^2}{q^2}}$ is a quantity called London penetration length, that describes the typical transient distance between a completely shielded superconducting region and a region in which a magnetic field is present.
The ratio between ξ and λ splits superconducting materials into two categories:

- If $\xi \gg \lambda$, then at any point below its T_c and $H_c(T)$ it is energetically convenient for a bulk superconducting sample to completely expel the magnetic field from its insides, thus displaying a uniform superconducting order parameter in its bulk.
  This class of superconductors is called type 1 superconductors. Aluminium, lead, and mercury fall into this category.

- If $\xi \ll \lambda$, then for any temperature $T < T_c$ there is an interval of magnetic field values $H_{c1} < H < H_{c2}$ in which for the system it is not energetically convenient to expel all of the magnetic field nor to remain completely in the normal phase, that is, they are superconductors that can display incomplete Meissner effect.
  In this regime, the material's bulk is not uniform and presents some regions where the magnetic field is completely expelled and others where a finite magnetic field is present. For magnetic field values close to H_{c1}, the latter take a vortex-like shape and are called Abrikosov vortices. From Eq. (4) and Eq. (3) we can derive that in each vortex the amount of magnetic flux is quantised in units of Φ_0. This class of superconductors is called type 2 superconductors. Niobium and vanadium fall into this category.

2.3 THEORY OF SUPERCONDUCTING WEAK LINKS

2.3.1 *Superconducting devices: Josephson Junctions*

Superconductivity-based devices display macroscopic quantum phase coherence; therefore, an additional tuning knob to control their behaviour is present: the superconducting phase, that is the complex phase of the wave function of the Cooper pair condensate.
The most simple superconducting device that allows access to this degree of freedom is the Josephson junction (schematically depicted in Fig. 2), which consists of two superconducting regions separated by a gap section made of a normal metal, a semiconductor or an insulator (including, in principle, vacuum).
If the gap is sufficiently short and the materials and interfaces have good quality,

7 This follows from the Maxwell's equation $\vec{\nabla} \times \vec{B} = \mu_0 \vec{J}$ and from the definition of the vector potential $\vec{\nabla} \times \vec{A} = \vec{B}$.

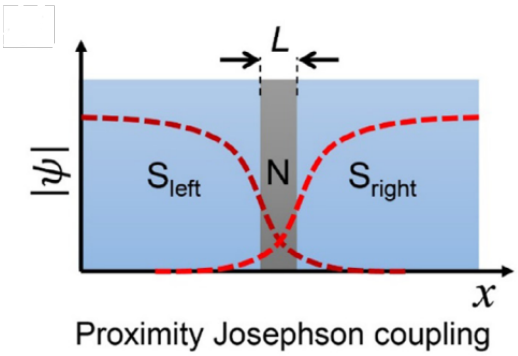

Figure 2: Visual representation of a superconducting weak link: the superconducting order parameter Ψ (dashed red lines) penetrates into the normal region allowing supercurrent flow. Adapted form [7].

a supercurrent flow can cross the junction: the effect responsible for this varies depending on the kind of material the junction is made of:

- in the case of Superconductor-Insulator-Superconductor junctions, the flow of supercurrent is due to Cooper pair quantum tunnelling effects and thus these devices take the name of Tunnel Junctions[8];
- instead, in the case of superconductor-semiconductor-superconductor or superconductor-normal metal-superconductor junctions, the main effects at play are proximity effect and Andreev reflection; such devices take often the name of superconducting weak links.
  The behaviour of semiconductor-based weak links can be controlled through Field Effect by applying a gate voltage to control their charge carrier density [8].

Furthermore, superconducting weak links can fall into different categories depending on their spatial dimensions and the properties of the material they are made of:

- planar junctions: superconducting weak links fall into this category when one of their transversal spatial dimensions (their thickness t) is small with respect to the other (their width W): $t \ll W$; this condition is typical of junctions based on nanostructures that display planar quantum confinement;
- short/long junctions: a superconducting weak link is said to be short when the length of it normal region L (see Fig. 2) is small compared to the superconducting coherence length of the electrodes ξ: $\xi \gg L$; vice versa, the opposite limit defines the long junctions category;
- ballistic/diffusive junctions: the amount of disorder in the normal region of a weak link is quantified by its mean free path ℓ_e, defined as the typical distance that a charge carrier travels between two consecutive scattering events. In a diffusive junction (also referred to as "junction in the dirty limit") the mean

8 These devices are at the basis of the most common superconducting quantum computer architectures [2].

free path is small with respect to the junction spatial dimensions; on the other hand, in a ballistic junction (also referred to as "junction in the clean limit"), the mean free path is large with respect to the junction length L, ensuring that charge carriers hardly ever experience scattering events while travelling across the normal region.

In this paragraph, the features common to every kind of Josephson junction will be presented, but the rest of this thesis will focus only on planar, short, ballistic superconducting weak links.
Far in the bulk of the superconducting leads, in absence of magnetic fields, the superconducting phase has a well defined value $\phi_{L,R}$ that can differ between the left and the right lead: $\phi_L \neq \phi_R$.
Due to the close relationship that joins a superconducting phase gradient to a supercurrent flow (Eq. (5)), a given superconducting phase difference across the junction can be imposed by current biasing the device and vice versa: this takes the name of DC Josephson effect. The dependence of the supercurrent across the junction on the superconducting phase difference takes the name of current-phase relationship (CPR) and differs from system to system.
In the case of tunnel junctions, the CPR takes the form given by the first Josephson equation [6]

$$I = I_c \sin(\phi_L - \phi_R), \tag{12}$$

where I_c is the critical current of the junction, that is the maximum supercurrent that can flow across it, which depends on the composition, geometry, and temperature of the system[9].
Josephson junctions behave like non-linear inductors and for this reason they can be used to fabricate non-linear LC resonators, which constitute the basic architecture for conventional superconducting QuBits. In fact, a non-linear inductance is needed to induce anharmonicity in the system and, therefore, suppress transitions between its two energy levels of interest for quantum computation and all of its additional excited states [2].
A paramount result is that Josephson junctions in the dirty limit or close to their critical temperature (above which no supercurrent can flow across the junction) behave as a tunnel junction [3]; however, due to the much richer underlying physics, in clean superconducting weak links at low temperatures and in presence of transparent interfaces, the current phase relationships can differ a lot from the sinusoidal one [3].
The potentialities of superconducting weak links span from their bare inclusion in conventional superconducting QuBit designs [13, 14] to the study of topological effects [15–18] and the implementation of novel devices like Andreev Spin QuBits [19, 20].

9 So far we are not considering any effects due to the presence of magnetic fields.

2.3.2 *Current phase relationship*

The microscopic theory that describes the behaviour of superconducting systems is summarized by the Bogolyiubov-De Gennes [9] equations (see Section 2.2.3)

$$E\Psi(\vec{x}) = \begin{pmatrix} H_e(\vec{x}) & \Delta(\vec{x}) \\ \Delta^\star(\vec{x}) & H_h(\vec{x}) \end{pmatrix} \Psi(\vec{x}). \tag{13}$$

In a Josephson Junction, the superconducting phase in a lead corresponds to the complex phase of the pair potential $\Delta(\vec{x}) = \Delta_0(\vec{x})\, e^{i\phi(\vec{x})}$ in said lead; let us assume the amplitude of the pair potential to be the same on the two sides of the junction $\Delta_{0R} = \Delta_{0L}$ and let us call the phase difference across the junction $\phi = \phi_L - \phi_R$.
At thermal equilibrium, the total supercurrent that flows across a superconducting weak link can be derived from the excitation spectrum of the system by making use of the fundamental relation[10]

$$I = \frac{2e}{\hbar}\frac{\partial F}{\partial \phi}, \tag{14}$$

where F is the Helmholtz free energy of the system.
The following definitions are taken as a starting point:

$$F = U - TS \tag{15}$$

$$U = \langle H_e \rangle - \int \frac{|\Delta(\vec{x})|^2}{g(\vec{x})} d\vec{x} \tag{16}$$

$$S = 2k_B \sum_{\varepsilon>0} (f(\varepsilon)\log(f(\varepsilon)) + (1-f(\varepsilon))\log(1-f(\varepsilon))); \tag{17}$$

here, S is the entropy of the system, U its internal energy, $g(\vec{x})$ is the local BCS interaction constant, $\langle H_e \rangle$ the expected value of the single electron Hamiltonian, $f(\varepsilon)$ the Fermi-Dirac distribution; the summation is carried out over the positive eigenvalues of the Bogolyubov-De Gennes Hamiltonian, and the factor 2 is due to spin degeneracy.
After some cumbersome calculations [9, 21], the following results are obtained:

$$F = -k_B T \sum_{\varepsilon>0} \log\left(2\cosh\left(\frac{\varepsilon}{2k_B T}\right)\right) + \int \frac{|\Delta(\vec{x})|^2}{g(\vec{x})} d\vec{x} + \mathrm{Tr}(H_e) \tag{18}$$

The following aspects can be noted [21]:

- The trace of the single particle Hamiltonian ($\mathrm{Tr}(H_e)$)is independent of the phase difference across the junction. Therefore, this term does not contribute to the supercurrent.
- The integrand in the second term displays a dependence on ϕ just inside the junction region ($g(\vec{x})$ is phase independent as well as $|\Delta(\vec{x})|^2$ in the bulk of each lead); the contribution to the supercurrent due to this term scales like L/ξ, where ξ is the superconducting coherence length of the electrodes and L is the junction length; in the short junction limit, the contribution due to this term is negligible.

10 This relation can be readily derived from Ginzburg-Landau theory Eq. (3), but it far more general [21].

- As a result, in the short junction limit, the most relevant contribution to the supercurrent flow is given by the first term in the free energy expression.

In the short junction limit the supercurrent flow is thus described by the following expression

$$I = -\frac{2e}{\hbar}\sum_{\varepsilon_p>0}\tanh\left(\frac{\varepsilon_p}{2k_BT}\right)\frac{\partial\varepsilon_p}{\partial\phi} - \frac{4ek_BT}{\hbar}\int_{\Delta_0}^{\infty}\log\left(2\cosh\left(\frac{\varepsilon}{2k_BT}\right)\right)\frac{\partial\rho}{\partial\phi}d\varepsilon \quad (19)$$

where we have separated the contribution of the discrete energy spectrum of the system (described by a discrete set of energies ε_p) from the continuous one (described by the out-of-gap energy density of states $\rho(\varepsilon)$). In the short junction limit, the continuous spectrum constribution scales like L/ξ, [21], thus it is negligible with respect to the supercurrent carried by the discrete spectrum.
Finally, the expression for the supercurrent in a short superconducting weak link at thermal equilibrium is

$$I = -\frac{2e}{\hbar}\sum_{\varepsilon_p>0}\tanh\left(\frac{\varepsilon_p}{2k_BT}\right)\frac{\partial\varepsilon_p}{\partial\phi} \quad (20)$$

and therefore the junction's current-phase relationship is fully determined by its discrete energy level spectrum [21]. The following paragraphs aim at descibing a well-established model used to describe superconducting weak links and retrieve such spectrum.

2.3.3 *Andreev reflection and BTK formalism*

In order to understand the physics of hybrid devices, it is necessary to comprehend the phenomenology that takes place at the interface between a superconductor and a normal material placed in electrical contact with one another.
In 1982 Blonder, Tinkham, and Klapwijk [22] formulated a Boltzmann equation-based approach to describe the current-voltage curves across a normal-superconductor interface: the BTK formalism.
Such description is built on the solution of the BdG equations in 1D at the interface between two defect free-regions, one of which displays a superconducting pairing Δ_R; the other region is assumed to be a normal conductor with $\Delta_L = 0$; such regions are separated by a delta-like barrier of strength Z to describe the non-ideality of the interface (disorder, Schottky barriers, and impurities).
Let us assume the zero of the energy scale to be the chemical potential in the superconducting region, i.e. the energy of the Cooper pair condensate. For the scattering of an electron of given energy impinging from the normal side of the interface, the following possible outcomes have to be considered:

- the electron can get reflected back: this process is always possible at a potential barrier and takes the name of normal reflection (depicted in the left side of Fig. 3); the probability associated to this process is labelled as $B(E)$;

- the energy of the electron lies inside the superconducting energy gap. Then it cannot scatter into the superconductor as a single particle excitation; however,

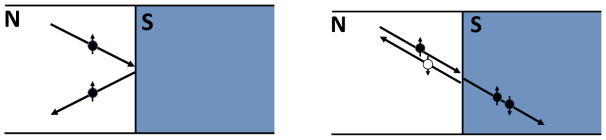

Figure 3: On the left: normal reflection at a normal-superconductor interface; on the right: Andreev reflection taking place at the same interface.

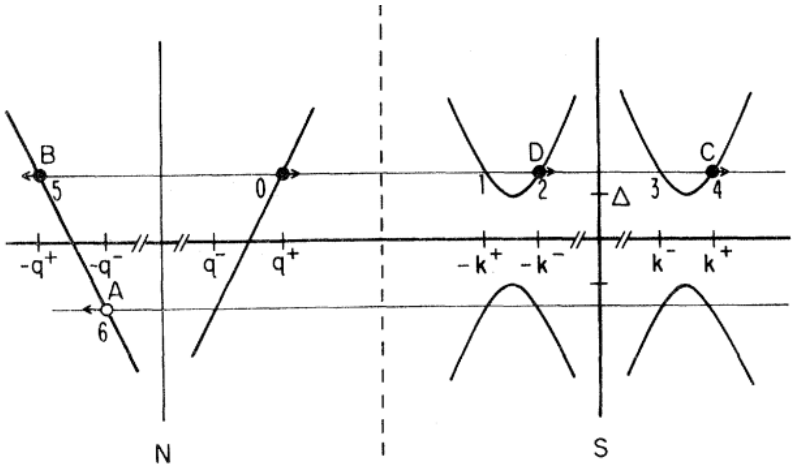

Figure 4: Possible scattering processes occurring at a Normal-Superconductor interface: an electron in the state 0 impinging from the normal side can either experience normal reflection (B), Andreev reflection (A) or transmission as a quasiparticle excitation in the superconductor (C,D); adapted from [22].

it can bind to a counter-propagating electron to form a Cooper pair and together they can tunnel into the superconducting region. In the normal region, this is equivalent to an electron of energy E being backscattered as a time reversed hole of energy $-E$. This process takes the name of Andreev reflection[11] (depicted in the right quadrant of Fig. 3) and is strongly suppressed in presence of a high barrier strength Z; the probability associated to this process is labelled as $A(E)$;

- if the energy of the electron lies outside the superconducting energy gap, it can tunnel into the superconductor as a single particle excitation; at a given energy, there are two possible single particle states with the proper group velocity in which the electron can scatter into; the probabilities associated to these process are labelled as $C(E)$ and $D(E)$

All of this scattering outcomes are depicted in Fig. 4. By solving the BdG equations in this system it is possible to determine the expressions for the scattering probabilities $A(E)$, $B(E)$, $C(E)$, and $D(E)$ (Fig. 5) which can be implemented in a Boltzmann equation approach to completely determine the I-V characteristics of the normal-superconductor interface.

11 Andreev reflection is present also when the energy of the impinging electron lies outside of the superconducting energy gap, but gets less and less probable the higher the difference between the energy of the electron E and the superconducting gap Δ is.

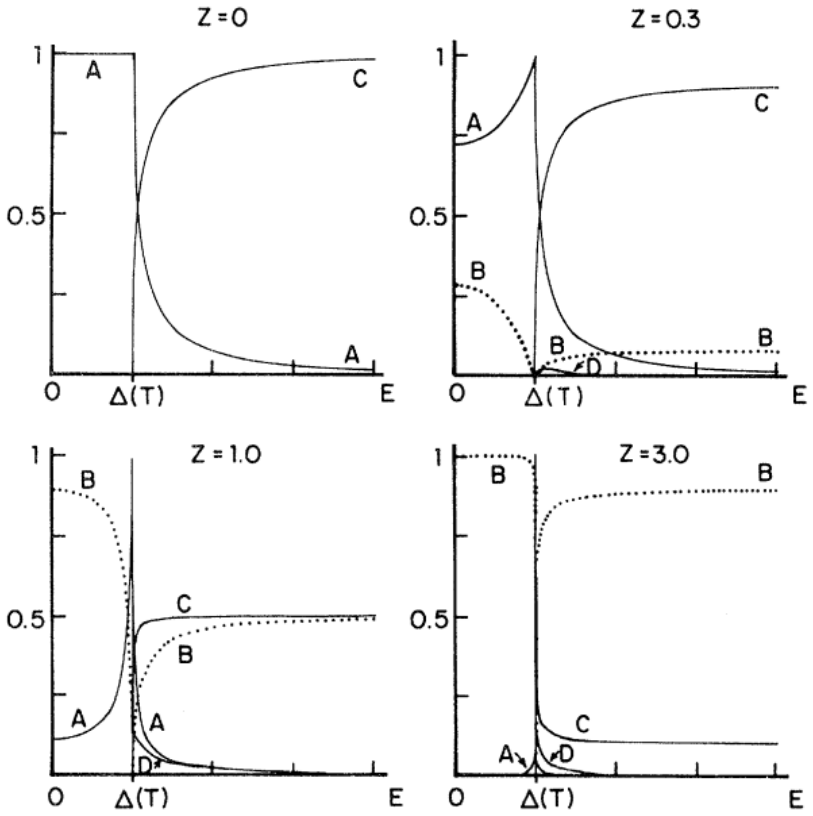

Figure 5: Dependence of the scattering probabilities on the energy of the impinging electron at various barrier strength; adapted from [22].

2.3.4 *Superconducting weak links: Andreev Bound States*

Once able to describe the scattering of charge carriers at an N-S interface by computing the relative scattering amplitudes, Tang et al. [23] were able to describe the behaviour of an S-N-S system by adopting a scattering matrix-based approach. The easiest case to treat corresponds to a 1D system in the absence of any interface potential barrier, Fermi velocity mismatch, or Fermi wavelength mismatch between the normal and the superconducting regions. In these conditions, at energies inside the superconducting gap, only Andreev reflections are allowed (see Fig. 5). By imposing a good definition of the wavefunction, i.e., its hole and electron components are single valued, it can be shown that the in-gap energy spectrum is composed of discrete eigenvalues (in a similar fashion as a particle in a box).
Such self-consistency relation results in the following quantization condition [8] (Fig. 6):

$$\frac{EL}{\Delta\xi} = 2\arccos\left(\frac{E}{\Delta}\right) \pm \phi + 2\pi n; \quad n \in \mathbb{Z}; \quad |E| \leqslant \Delta, \tag{21}$$

where E is the eigenstate energy, Δ the superconducting energy gap of the leads, ϕ the superconducting phase difference between the leads, ξ the superconducting coherence length of the leads, and L the junction length.
These eigenstates, whose wavefunctions are localized in the normal region and fade exponentially into the superconducting leads, take the name of Andreev bound states and constitute the discrete energy spectrum referred to in Eq. (20).
In the short junction limit, the left hand side of Eq. (21) can be neglected: only two Andreev bound states[12] are therefore present in the short junction limit, corresponding to [8]

$$E_{\pm} = \pm\Delta\cos\left(\frac{\phi}{2}\right), \tag{22}$$

which implies that, by inserting this result into Eq. (20) and taking the low temperature limit $|E_{\pm}| \gg k_B T$, the current phase relationship of an ideal junction is [8]

$$I = I_c \sin\left(\frac{\phi}{2}\right); \quad \phi \in [-\pi;\pi]. \tag{23}$$

Once we take into account also a delta-like potential barrier at each interface,[13] we obtain the following equations [8]:

$$E_{\pm} = \pm\Delta\sqrt{\frac{\cos^2\left(\frac{\phi}{2}\right) + 4Z^2}{4Z^2+1}} \tag{24}$$

$$I = I_c \frac{\sin(\phi)}{\sqrt{\cos^2\left(\frac{\phi}{2}\right) + 4Z^2}}; \quad \phi \in [-\pi;\pi], \tag{25}$$

where Z is the strength of the delta-like interface potential barriers.
By looking at the current-phase relationship dependence for different interface

12 Each with spin degeneracy.
13 Still assuming low temperature, short junction limit, and no Fermi wavelength nor Fermi velocity mismatch at the interfaces.

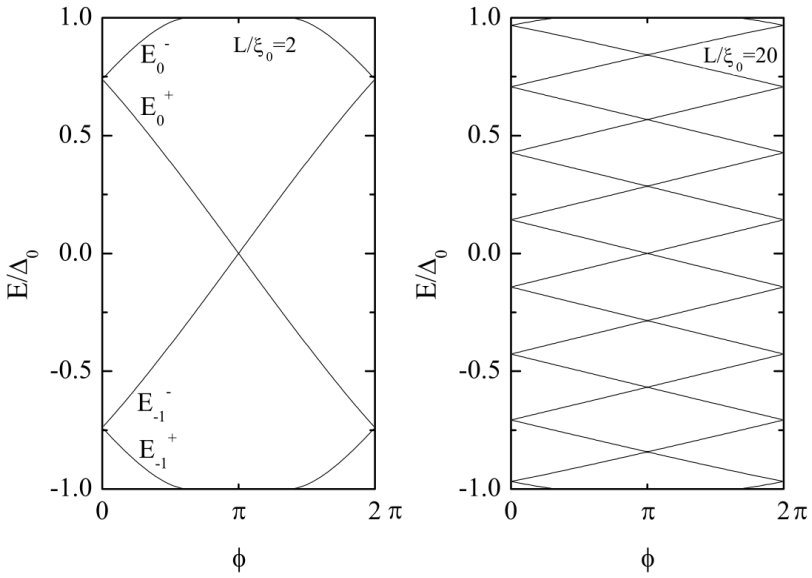

Figure 6: Andreev bound states energies as a function of the superconducting phase difference across an ideal junction of length $L = 2\xi$ (left) and $L = 20\xi$ (right); adapted from [8]

barriers, it can be noticed that the more transparent they get, the more skewed the CPR is (Fig. 7).

All of the previous equations assume the system to be one dimensional: in order to describe a more realistic situation, the transversal dimensions of the system must be taken into account.

More complex models can take into account intersubband scattering, junction length equaling its width, and Fermi velocity mismatch between transport channels in the normal region and the leads [8]. Nevertheless, the following pages aim at underlining how the results of this one-dimensional toy model are far more general than expected.

The problem in its most general form can be attacked analytically or numerically by scattering matrix approach in the normal region [24], taking into account all of the properties of the normal material (spin orbit coupling, presence of defects, Fermi velocity...).

This approach consists in the following wavefunction matching condition

$$S_A(E)S_N(E)\Psi_{in} = \Psi_{in}; \quad \Delta > E > 0, \tag{26}$$

where $\Psi_{in} = (\Psi_e, \Psi_h)$ is the normal region eigenstate wavefunction expressed in the normal region scattering basis. $S_A(E)$ is the scattering matrix relative to Andreev reflection at the interfaces, and $S_N(E)$ the scattering matrix across the normal region.

By assuming ideal interfaces[14] and no Andreev-reflection induced scattering be-

14 This is a valid assumption since any interface potential barrier can be taken into account as part of the normal scattering region.

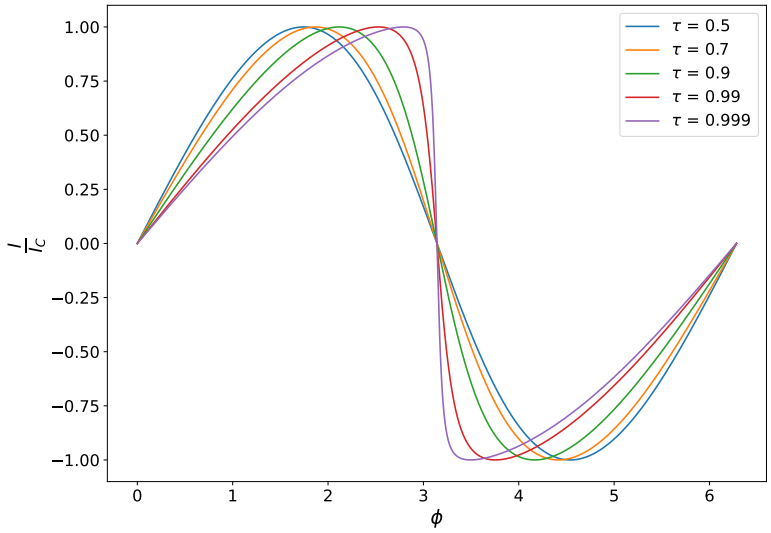

Figure 7: Current-phase relationship at various junctions transmittivities as obtained from Eq. (33).

tween different modes, in the short junction limit, the following expression for Andreev reflection holds

$$S_A(E) = e^{-i \arccos\left(\frac{E}{\Delta}\right)} \begin{pmatrix} 0 & r_A^\star \\ r_A & 0 \end{pmatrix}, \tag{27}$$

where

$$r_A = \begin{pmatrix} i\mathbb{1} & 0 \\ 0 & ie^{-i\phi}\mathbb{1} \end{pmatrix}. \tag{28}$$

By solving this matrix equation, the Andreev state spectrum can be obtained, and by plugging it into Eq. (20), the current-phase relationship can be obtained. If trivial scattering across the normal region ($S_N(E) = \mathbb{1}$) is assumed, then the matrix can be rearranged into n independent 2 by 2 blocks (n is the number of active scattering channels) that produce exactly the same equation as the one-dimensional case in the short junction limit.
In the most general case, the normal region scattering matrix can be written in the following form

$$S_N(E) = \begin{pmatrix} S_0(E) & 0 \\ 0 & S_0^\star(-E) \end{pmatrix}, \tag{29}$$

$$S_0(E) = \begin{pmatrix} r_{LL} & t_{LR} \\ t_{RL} & r_{RR} \end{pmatrix}. \tag{30}$$

The scattering matrix must be computed numerically from the normal region single particle Hamiltonian, which can be no easy task, but for the sake of this derivation let us assume that this computation has been performed. Since the energy range of interest is given by Δ, which is usually small compared to any other energy

scale of the system, the energy dependence of S_N can be approximated as trivial $S_0(E) = S_0(0)$.
By diagonalizing Eq. (26), the energy spectrum can be extracted. The final result is

$$\varepsilon_\nu = \pm\Delta\sqrt{1 - T_\nu \sin^2\left(\frac{\phi}{2}\right)}, \tag{31}$$

where $\nu \in [1, n]$ is the transport channel index and T_ν is the junction transmittivity of the ν-th transport channel.
Finally, the global current phase relationship of the junction is

$$I(\phi) = \frac{e\Delta}{2\hbar}\sum_\nu T_\nu \frac{\sin(\phi)}{\sqrt{1 - T_\nu \sin^2\left(\frac{\phi}{2}\right)}} \tanh\left(\frac{\Delta}{2k_B T}\sqrt{1 - T_\nu \sin^2\left(\frac{\phi}{2}\right)}\right). \tag{32}$$

Provided that there is no sizable difference between the transport channel transmittivities, then the following approximated expression holds

$$I(\phi) = \frac{\pi\Delta}{2eR_N} \frac{\sin(\phi)}{\sqrt{1 - \tau \sin^2\left(\frac{\phi}{2}\right)}} \tanh\left(\frac{\Delta}{2k_B T}\sqrt{1 - \tau \sin^2\left(\frac{\phi}{2}\right)}\right), \tag{33}$$

where τ is an effective junction transmittivity and $R_N = \frac{h}{2n\tau e^2}$ is the normal state resistance of the junction. The same result has been obtained by Kulik and Omelyanchuk solving the Elienberger equations [25].
It is easy to notice that this expression is no different from the one derived from the one-dimensional toy model (Eq. (25)). In particular, the main features of the CPR still hold:

- the more transparent the junction, the more skewed its current-phase relation;
- the less transparent the weak link, the more it behaves as a tunnel junction.

Furthermore, other essential features of superconducting weak links can be noticed:

- the weak link's critical current depends on the number of active transport channels, which depends on the density of states at the Fermi energy in the normal region;
- by controlling the chemical potential of the normal region via electrostatic gating, such density of states can be modified to enhance or suppress supercurrent flow across the junction;
- in particular, in case the normal region is a semiconductor and the chemical potential is placed in its energy gap, supercurrent flow across the junction is completely suppressed.

This is the functioning principle of the Josephson Field Effect Transistor (JoFET), which is the device at the basis of superconducting electronics.

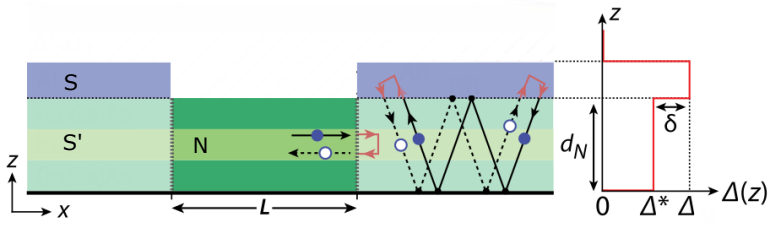

Figure 8: Proximity effect in a planar structure: the combination of normal reflection at the bottom of the film and normal/Andreev reflections at the interface with the superconducting leads induces a gap $\Delta^\star$ in the region direclty below the leads; image adapted from [28].

2.3.5 *Inclusion of the proximity effect*

The more transparent are the junction interfaces, the higher the critical current of the junction and the richer the physics that can be observed. However, obtaining high-performance interfaces is no easy task [26].
One necessary step is optimising the quality of the electrical contacts, that is the interfaces between the superconducting metal and the semiconducting normal region. The main issue is the fact that hetero-interfaces tend to be disordered systems due to the presence of impurities (e.g. oxidized regions) and mutual diffusion of one material into the other.
Nevertheless, there is a way of partially getting around this by exploiting the superconducting proximity effect: at the superconductor-semiconductor interface the superconducting order parameter does not drop to zero at the interface, but instead it penetrates into the normal material, modifying its local density of states. At the same time, the superconductor gap close to the interface gets reduced. This effect can be explained as the penetration of delocalized Cooper pairs across the superconductor-normal interface and can be described via the Eilenberger equations [3].
In particular, if the system's geometry resembles that in Fig. 8, where the normal region is a planar structure[15], the semiconductor immediately below the contacts acquires superconducting properties, that is a superconducting gap that can be described by the following relation [27]

$$\Delta^\star(T) = \frac{\Delta(T)}{1 + \frac{\gamma_B}{\pi T_c}\sqrt{\Delta^2(T) - \Delta^{\star 2}(T)}}, \tag{34}$$

where T_c is the superconductor critical temperature expressed in electron-Volts and γ_B is a parameter that describes the Cooper pair breaking across the S-N interface: the lower it is, the more transparent the interface.
This way an effective S-S'-N-S'-S junction is obtained, with a far more complex out-of-gap energy spectrum [8].
However, the main result is that almost perfectly transparent S'-N interfaces are obtained, since they are not made of boundaries between different materials, but between two regions of the same impurity-free epitaxially-grown semiconductor crystal that resent of the proximity effect differently.

15 Thinner than the superconducting coherence length.

On the other hand, we are interested in having the highest induced superconducting gap possible, in order to operate in a suitable range of temperatures and magnetic fields: for this reason it is of paramount importance that the interface between the metal and the semiconductor is as transparent as possible, so as to minimize γ_B and therefore maximize Δ^*.

2.3.6 *Voltage carrying state: multiple Andreev reflections*

In addition to the Josephson current, one of the prominent phenomena displayed by superconducting weak links is the presence of Multiple Andreev Reflections (MAR).
This effect takes place when a finite voltage bias is imposed on the junction, i.e., when the two superconducting leads are separated by a potential difference.
Even in these conditions, at every normal-superconductor interface, the scattering phenomenology is the one described by the BTK formalism, thus Andreev reflections take place.
The description of voltage biased junctions based on the BTK formalism (that is step-like interfaces with delta-like potential barriers) takes the name of Octavio – Blonder - Tinkham – Klapwijk (OBTK) model [29, 30].
Let us assume a perfectly transparent superconducting weak link with a proximity-induced superconducting gap equal to Δ^*; due to the electro-chemical potential difference between the two superconducting leads, the following process is active (as displayed in Fig. 9):

- an out-of-gap single particle excitation in one of the superconducting leads penetrates into the normal region;
- such particle gets Andreev reflected by the opposite lead;
- the excitation experiences back and forth Andreev reflections, accumulating an energy equal to eV at every normal region crossing, until...
- ...it reaches one of the leads with an out-of-gap energy, allowing it to exit the normal region as a single particle out-of-gap excitation.

The greater the ratio between the superconducting energy gap and the voltage drop across the junction Δ^*/V, the higher the number of Andreev reflections necessary

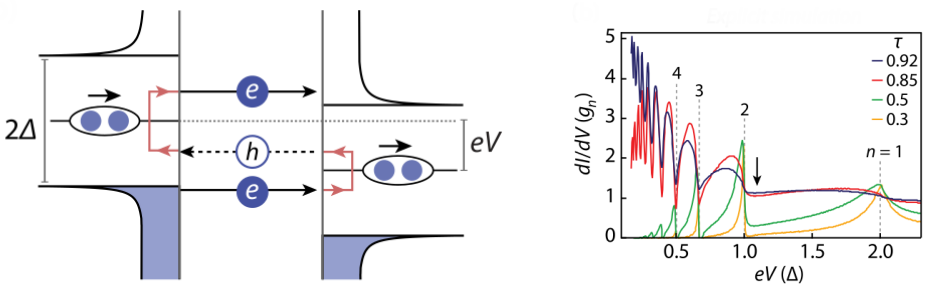

Figure 9: On the left: visual representation of a Multiple Andreev Reflection process of order $n = 2$; on the right: differential conductance as a function of the voltage bias in Josephson Junctions with different transparencies; adapted from [28].

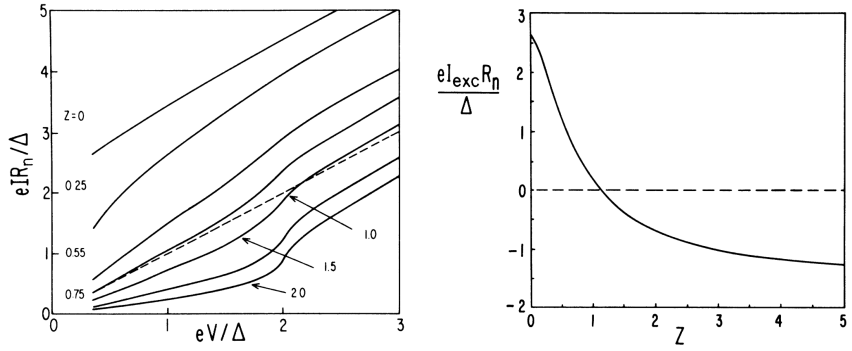

Figure 10: On the left: voltage-current curves extracted from the OBTK model for different values of the interface barrier strength Z; on the right: relation between the normalized excess current and the interface barrier strength in the OBTK model; adapted from [30].

for the particles to get out of the energy gap. In particular, an n-times Andreev reflection process is active when $\frac{2\Delta^\star}{en} \leqslant V \leqslant \frac{2\Delta^\star}{e(n-1)}$.[16]
Since every Andreev reflection effectively transfers a $2e$ charge across one of the normal-superconductor interfaces, the more Andreev reflections are present in the active transport mechanism, the more the electrical conductivity of the junction is enhanced.
This creates the so-called subharmonic gap structure, that is a step-like dependence of the junction's differential conductance on the voltage bias, with transitions located at the previously mentioned voltages $V_n = \frac{2\Delta^\star}{ne}$, which takes the form of differential conductance oscillations once finite junction transmittivity is taken into account (Fig. 9).
By fitting the differential conductance curves with an appropriate model [5, 28, 31], the junction's interface transparency can be obtained, making MAR measurement a valid tool to estimate the quality of superconducting heterostructures and, especially, to estimate the induced gap. In fact, in the case of highly transmissive junctions, the latter can be derived from the positions of dips in the differential conductance signal corresponding to the transitions $V_n = \frac{2\Delta^\star}{ne}$.
On the other hand, in order to achieve an on-the-fly estimation of the quality of the interfaces in the junction, it is convenient to look at its excess current I_E.
As just discurred, due to the presence of single Andreev reflection processes, in an ideal junction even at high voltage bias $V > \frac{2\Delta^\star}{e}$, the conductance across the junction is enhanced with respect to the normal state conductance of the junction. This results in an Ohmic current-voltage dependence if it wasn't for the fact that the linear fit of the data does not pass through the origin, but has a finite intercept at a value of current equal to I_E (as shown in Fig. 10).
As the interface quality gets lower, the value of the excess current decreases, eventually becoming negative for particularly dirty interfaces.
The quantity $\alpha = eR_N I_E/\Delta^\star$ is strongly tied to the interface barrier strength Z of the OBTK model (as shown in Fig. 10). The more α is close to the theoretical limit for ballistic junctions $\alpha_{ideal} = \frac{8}{3}$, the better the interface transparencies [30].
It is worth noticing that, due to the modified density of states of the proximity-

16 The single Andreev reflection process is active for every voltage drop above $V = \frac{2\Delta^\star}{e}$.

induced region, in principle Andreev reflection can occur even when a particle impinges on the S'-N interface with an energy that does not lie inside the induced energy gap, but lies inside of the energy gap of the metallic leads that exert the proximity effect [8]. However, this process can be completely suppressed [5, 32] by a good but far from ideal interface quality between the metal and the semiconductor, i.e., when the induced gap is much smaller than the gap of the superconducting metal electrodes.

2.3.7 *Magnetic field influence: superconducting quantum interference*

Magnetic fields and superconductivity do not really get along together [6]:

- on the one hand, applying a magnetic field on a bulk superconductor greater than its critical field H_c completely suppresses its superconducting behaviour reverting it to its normal phase;
- on the other hand, thanks to the Meissner effect, magnetic fields get completely (type I superconductors or type II superconductors with fields weaker than their H_{C1}) or partially (type II superconductors between H_{C1} and H_{C2}) expelled from bulk superconducting samples[17].

However, superconducting heterostructures include non-superconducting components, into which magnetic field can penetrate freely. Moreover, magnetic field expelled from the superconducting leads gets focused into the normal region sandwiched between them, enhancing the effect of the magnetic field.
It is therefore interesting to study the magnetoconductance of superconducting weak links, i.e., how the presence of an external magnetic field affects the supercurrent flow across the junction.
One of the best known cases is that of a planar junction subjected to a uniform, external magnetic field $\vec{B}$ perpendicular to the junction's plane. The easiest way to approach the problem is through Landau Ginzburg theory that, albeit phenomenological, qualitatively matches with numerical simulations [33].
Let us work within the following assumptions:

- high aspect ratio: $L/W \ll 1$ where L is the junction's length and W its width; this allows to consider the junction as an array of 1D junctions in parallel (i.e., we consider carrier trajectories just perpendicular to the electrodes);
- negligible self-field effects: supercurrent flow across the junction, like any current flow, generates a magnetic field that eventually interacts with the supercurrent itself; this is usually a faint effect for junctions with low current densities: its strength is evaluated by a parameter called Josephson penetration length [34]

$$\zeta = \sqrt{\frac{\Phi_0 W t}{\mu_0 I_c (2\lambda + L)}}, \tag{35}$$

17 As already discussed in Section 2.2.4, the remaining field gets confined into structures called Abrikosov vortexes.

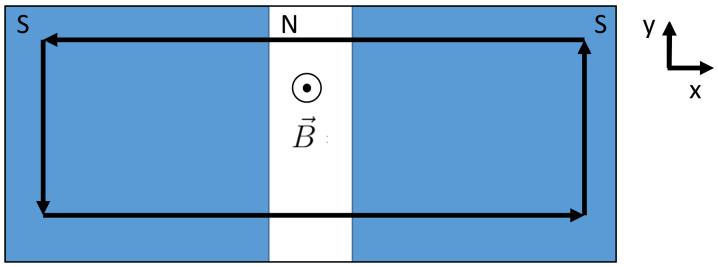

Figure 11: Weak link in presence of an externally applied magnetic field: scheme of the path for the circulation integral that allows to compute the spatial dependence of the superconducting phase difference across the junction.

where λ is the London penetration length of the superconductor[18], Φ_0 the superconducting flux quantum, μ_0 the vacuum magnetic permittivity, t the junction thickness, and I_c the critical current of the junction in absence of external fields, assumed for the sake of simplicity to be uniform.
In order to be able to neglect self-fields, each of the junction dimensions must be small with respect to ζ; by considering the typical parameters of the junctions that will be presented in this work ($L = 200\,\text{nm}$, $W = 1\ \mu\text{m}$, $t = 100\,\text{nm}$, $\lambda = 40\,\text{nm}$, and $I_c = 100\,\text{nA}$) we obtain a Josephson penetration length of $\zeta = 7.5\ \mu\text{m}$, thus satisfying this condition;

- uniform magnetic field $\vec{B} = B\hat{z}$ across the junction, that can be described by a Landau gauge vector potential $\vec{A} = Bx\hat{y}$, where the axis directions were defined as in Fig. 11.

In this framework, the first thing to be noticed is that a superconducting phase difference across the junction is not well defined anymore.
In fact, by combining Eq. (5) with the relationship

$$\Phi = \int_\gamma \vec{A} \cdot d\vec{l} \tag{36}$$

between the magnetic flux across a surface delimited by a closed curve γ and the magnetic vector potential, the following relation is obtained

$$\Phi = \int_\gamma \left(\frac{\hbar}{2e} \vec{\nabla} \phi(\vec{x}) - \frac{m\vec{J}(\vec{x})}{4e^2 n(\vec{x})} \right) \cdot d\vec{l} \tag{37}$$

By taking a close loop as depicted in Fig. 11, the only branches that contribute to the circuitation integral are the ones deep in the bulk of the leads, where transversal supercurrent is absent[19]. This implies that, since a finite flux $\Phi = B(L + 2\lambda)y$ is present across the area delimited by the curve and since the line integrals correspond to the superconducting phase difference between two pairs of points at different y

18 The region of the heterostructure where the magnetic field is present is $L + 2\lambda$ long.
19 Transversal supercurrent is generated to screen the magnetic field in the bulk of the electrode: it is confined to a λ-wide region at the interface of the electrode.

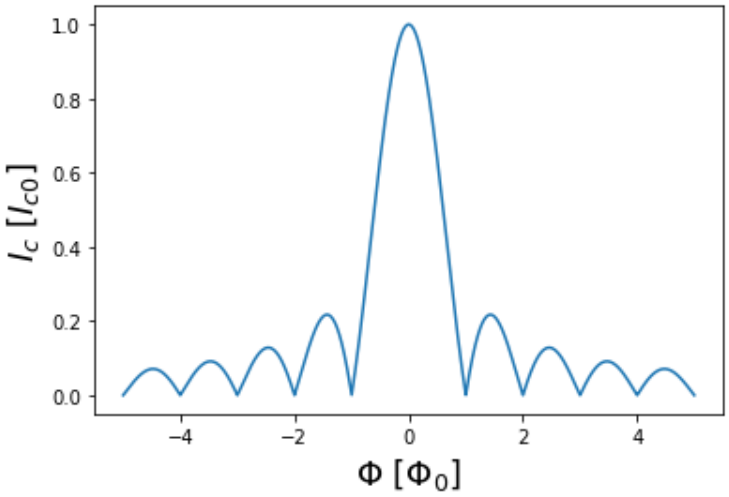

Figure 12: Magnetic interference pattern in a high aspect ratio junction possessing a sinusoidal CPR (Fraunhofer pattern), plotted from Eq. (41); the critical current is normalized with respect to its value at zero magnetic field.

coordinates, there is a spatial dependence of the phase difference across the junction in y:

$$\Delta\phi(y) = \Delta\phi(y=0) + \frac{2\pi B(2\lambda + L)y}{\Phi_0}. \tag{38}$$

This means that there is the formation of positive and negative supercurrent regions, which at high enough magnetic fields lead to the formation of Josephson vortices, which are areas of the junction that contribute with zero net supercurrent.
To obtain the total supercurrent flowing across the junction, it is necessary to integrate over the infinite 1D junctions in parallel, each with its own phase difference across itself; defining $J_c(y)\kappa(\Delta\phi(y))$ to be the current phase relationship of the 1D junctions, the total supercurrent across the junction is equal to

$$I(\Delta\phi(y=0)) = \int_{-\frac{W}{2}}^{\frac{W}{2}} J_c(y)\kappa\left(\Delta\phi(y=0) + \frac{2\pi B(2\lambda + L)y}{\Phi_0}\right) dy. \tag{39}$$

In the case of sinusoidal CPR ($\kappa(\Delta\phi) = \sin(\Delta\phi)$) and assuming the zero-field critical current density to be uniform across the junction $J_c(y) = J_C$, this is equal to

$$I(\Delta\phi(y=0)) = I_c(B=0)\sin(\Delta\phi(y=0))\left(\frac{\sin\left(\frac{\pi\Phi}{\Phi_0}\right)}{\frac{\pi\Phi}{\Phi_0}}\right). \tag{40}$$

The supercurrent across the junction is at maximum when the reference phase difference $\Delta\phi(y=0) = \pi$, giving the well known Fraunhofer pattern modulation:

$$I_c(\Phi) = I_c(B=0)\left|\frac{\sin\left(\frac{\pi\Phi}{\Phi_0}\right)}{\frac{\pi\Phi}{\Phi_0}}\right|, \tag{41}$$

depicted in Fig. 12.
Although this result is limited to sinusoidal CPRs, the "Fraunhofer pattern" denomination is often used in any type of junction, due to the fact that current phase

relationships are always 2π-periodic and therefore the main features of the critical current modulation are preserved even when the sinusoidal assumption is dropped:

- the presence of a magnetic field decreases the junction's critical current with respect to the zero-field case;
- when an integer number of superconducting magnetic flux quanta penetrate into the junction's normal region, destructive interference occurs, and the junction's critical current drops to zero;[20] this divides the critical current modulation curve into lobes.
- each lobe corresponds to a specific number of completely developed Josephson vortices present inside the junction.

To describe more general cases, the hypothesis of zero-field uniform supercurrent denisity distribution must be dropped.
Till very recently [35], no direct measurement of the supercurrent density distribution in Josephson junctions has been performed: in absence of that, there has been struggle to retrieve such information from the plot of the critical current modulation driven by the magnetic field.
Dynes and Fulton [34] were able to develop a technique to retrieve the supercurrent density distribution from the Fraunhofer pattern in the case of sinusoidal current phase relationship, akin to an inverse Fourier transform. Despite the strict set of hypotheses this method is based upon [36], it is often utilised even outside its range of validity for qualitative evaluations.

20 This holds just in the case of zero-field uniform supercurrent distribution; otherwise, the minima of the Fraunhofer pattern remain finite, but an oscillatory pattern is still expected.

3

STATE OF THE ART

3.1 INTRODUCTION TO SEMICONDUCTOR NANOSTRUCTURES

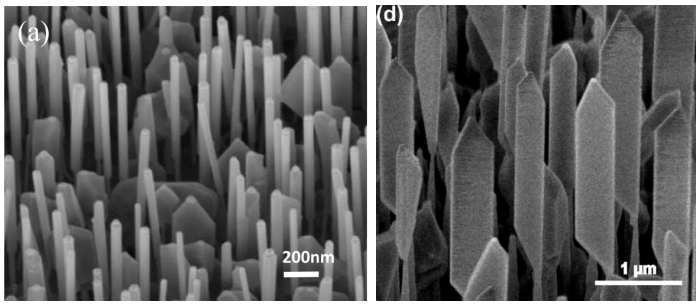

Figure 13: Scanning Electron Microscopy images of semiconductor nanostructures. On the left, InSb nanowires (adapted from [37]), on the right InSb nanoflags (adapted from [38]).

In order to observe quantum phenomena in semiconductors it is crucial to be able to produce samples that present both sufficiently high charge carrier concentration and sufficiently long coherence length[1] and momentum relaxation length (usually quantified with the electron mobility of the sample) with respect to the typical dimensions of the region of interest. These requirements are usually met in structures in which charge carriers are confined into regions with at least one dimension compatible with their Fermi wavelength, giving rise to quantum confinement effects.
Both semiconductor heterostructures (e.g. quantum wells) and single atomic layer materials (e.g. graphene) have proven to be excellent platforms for designing quantum devices, but they are not the only alternatives.
Recent developments in epitaxial techniques allow near-perfect control over the composition and the morphology [39] of crystalline samples at a nanoscale level: "nanoflags" (2D), "nanowires" (1D), or "quantum dots" (0D) geometries can be obtained, as displayed in Fig. 13.
By limiting the presence of dopants to the surface of such structures, that is leaving their bulk to be defect-free, they can display electron mobilities that, although far inferior to those of the most refined quantum wells, are sufficiently high to support a huge plethora of quantum phenomena, including conductance quantization [40], Coulomb blockade [41], Quantum Hall Effects [42], and superconducting proximity effect [5].

1 The parameter that determines whether or not the system displays quantum effects is the carrier coherence length l_ϕ, that can be interpreted as the maximum distance over which a charge carrier can display effects of self-interference (in the same way as it is defined for photons in interferometric experiments). It can be way larger than the charge carrier wavelength, depending on the quality of the device and the temperature of the system.

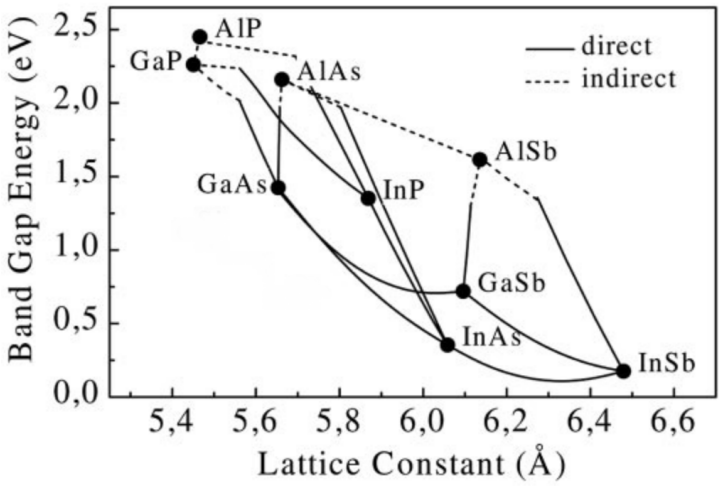

Figure 14: Energy bandgap-vs-lattice constant in III-V semiconductors alloys; adapted from [43].

3.2 INDIUM ANTIMONIDE AS A MATERIAL PLATFORM

3.2.1 *InSb properties*

Indium Antimonide (InSb) is a III-V semiconductor with zincblend crystalline structure and a room temperature lattice constant of $a = 6.65$ Å [44], which is the largest in the III-V family. Its small[2] (compared to other III-V alloys) direct bandgap of about $E_g = 0.23$ eV [45–47] makes it a promising candidate to develop infrared emission and detection devices [48]. These peculiar characteristics are what makes InSb both interesting and difficult to handle.
In fact, due to large lattice mismatch with all of the common crystal growth substrates, fabricating InSb-based samples is a daunting task, but it might be worth the struggle since its properties, when combined with superconductivity, are predicted to give rise to exotic states called Majorana zero modes. This is one of the main topics studied by a prolific branch of condensed matter physics research that investigates topological systems, i.e., systems displaying properties that are resilient to the action of external perturbations and to the presence of impurities [49]. In recent years, great investments have been dedicated to technological advancements towards the development of topological quantum devices, which would allow to perform fault tolerant quantum information processing [49, 50].

Spin-orbit coupling

Spin-orbit coupling is a relativistic effect experienced by particles that posses a finite gyromagnetic factor, like electrons.
Once a magnetic particle is in motion in a region where an electric field $\vec{E}$ is present, due to relativistic fields transformations such particle can experience a finite magnetic field in the reference frame where it is at rest. Such magnetic field interacts with the magnetic dipole moment of the particle, therefore correlating the

2 Large lattice constants are correlated to small bandgaps.

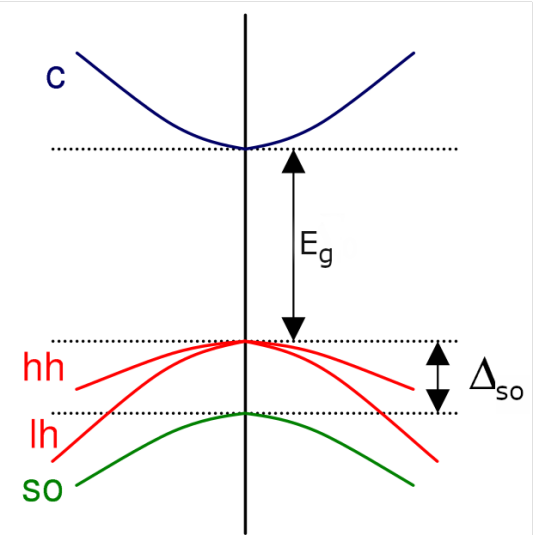

Figure 15: Band structure of III-V semiconductors; adapted from [51].

particle spin to its motion. In the case of an electron, the Hamiltonian describing this process is the following [51]:

$$H_{SO} = g_e \mu_B \left(\vec{E} \times \vec{p}\right) \cdot \frac{\vec{\sigma}}{2m_e c^2} \tag{42}$$

where $g_e = 2$ is the gyromagnetic factor of the free electron and m_e the free electron mass.

Antimony is a heavy atom, which enhances relativistic effects in antimony-made materials. Like other III-V semicondutors [51], InSb possesses an s-wave conduction band and three p-wave valence bands[3], two of which (the $J = \frac{3}{2}$, labelled as lh and hh in Fig. 15) are separated from the third one (the $J = \frac{1}{2}$, labelled ad so in Fig. 15) by the so-called spin-orbit split off gap, as shown in Fig. 15. The large split off of $\Delta_{SO} = 0.803\,\text{eV}$ of InSb evidences the strength of its spin-orbit interaction.

In absence of external electric fields, the behaviour of a charge carrier in the conduction band can be described by the following single particle Hamiltonian where the influence of spin-orbit coupling is completely contained in the parameters $m^\star$ and g [51]:

$$H = \frac{(\hbar\vec{k} + e\vec{A})^2}{2m^\star} + \frac{g}{2}\mu_B \vec{\sigma} \cdot \vec{B} \tag{43}$$

$k \cdot p$ perturbation theory states that the effective mass of the conduction band is modified due to interband mixing in the following way [51]:

$$\frac{1}{m^\star} = \frac{1}{m_0^\star} + \frac{2P_0^2}{3\hbar^2}\left(\frac{2}{E_g} + \frac{1}{E_g + \Delta_{SO}}\right), \tag{44}$$

where $1/m_0^\star$ is the conduction band effective mass without taking into account interband mixing. P_0 is a matrix element that quantifies the overlap between p and s orbitals. The equation Eq. (44) clearly states that the smaller the bandgap E_g,

3 Multiplicities do not take into account spin degeneracy; the indicated bands do not possess s nor p symmetry due to interband mixing, but they are commonly labelled according to the type of orbitals with the strongest contribution.

the smaller is the effective mass of the material, which is in agreement with InSb possessing a small effective mass $m^\star = 0.018 m_e$ [45, 52, 53].
Another result of $k \cdot p$ perturbation theory is the determination of the influence of interband mixing on the Landè g factor [51]:

$$g = 2 + \frac{2E_{P0}}{3}\left(\frac{1}{E_g + \Delta_{SO}} - \frac{1}{E_g}\right), \tag{45}$$

where $E_{P0} = P_0^2/\hbar^2 = 23.1\,\text{eV}$ [54] is the square of the momentum matrix element for InSb.
Since E_{P0} is very large with respect to the other energy scales and $E_g < \Delta_{SO}$, the InSb Landè factor $g \approx -50$ [54] is one of the largest observed in III-V materials.
In case an external or built-in electric field $\vec{E}$ is present, interband coupling induces a spin-orbit interaction even in the otherwise "s-wave" conduction band: the so-called Rashba spin-orbit coupling[4] [51, 56], which can be described by adding an additional term to the Hamiltonian:

$$H = \frac{(\hbar\vec{k} + e\vec{A})^2}{2m^\star} + \frac{g}{2}\mu_B \vec{\sigma}\cdot\vec{B} + \alpha\left(\hat{z}\times\vec{k}\right)\cdot\vec{\sigma} \tag{46}$$

where $\alpha = \frac{P_0^2}{3}\left(-\frac{1}{(E_g+\Delta_{SO})^2} + \frac{1}{E_g^2}\right)|\vec{E}|$ is the interaction parameter and $\hat{z}$ is the electric field direction. The low value of the energy bandgap with respect to the other energy scales of the system results in a large Rashba spin-orbit coupling parameter in InSb-based platforms.

Schottky barriers and Ohmic contacts

Contacting semiconducting samples with metallic leads is usually an issue due to the nature of the electronic states localised at the semiconductor's surface [57]. Due to the presence of unsaturated atomic bonds, a high surface density of states is present; when electrostatic and diffusive equilibrium have been reached, the phenomenon of Fermi level pinning takes place: the electronic bands of the semiconductor bend in proximity of the interface in order for the chemical potential to be located at a precise position in energy, depending on the interface in question.
Most semiconducting materials have their chemical potential pinned close to the middle of their energy bandgap independently from their bulk doping level: a Schottky barrier is created between the metal and the semiconductor, precluding a transparent transfer of carriers between the two materials.
However, when dealing with superconducting proximity effect, it is crucial that the interface transparency is maximized, and therefore the presence of a Schottky barrier must be avoided.
When working with InSb-based nanostructures like nanowires or nanoflags, the crystalline facets that are available for the deposition of the metallic leads belong to the {110} family. For this reason, it is essential to understand the behaviour of InSb

4 For non centrosymmetric crystals (like InSb) it is worth noticing that also another spin-orbit interaction is present: the Dresselhaus spin-orbit coupling [51, 55]. It is caused directly by the crystalline potential, so it is present also in bulk samples in the absence of external fields. However, in the case under study it is not the dominant effect and can be neglected.

at these surfaces.
The {110} surfaces of untreated InSb display Fermi level pinning close to its valence band maximum [58, 59], which results in an inconvenient Schottky barrier for electrons. However, technological advancements found that InSb{110} surfaces can be treated with sulphur-based solutions in order to substitute some indium surface atoms with sulphur atoms. Once this is done, the result is twofold [58]:

- sulphur atoms act like surface-localised donor impurities: the InSb crystal experiences an n-type doping, and, since carriers and impurities are separated, no reduction in its carrier mobility;
- the presence of sulphur donors at the surface results in the complete nullification of surface band bending: no Schottky barrier is present and an Ohmic contact is obtained.

For this reasons, indium antimonide is an ideal candidate to obtain extremely transparent semiconductor-superconductor interfaces [26].

3.3 INSB NANOFLAGS AS A MATERIAL PLATFORM

3.3.1 *State of the art of InSb-based nanodevices*

Due to its large lattice mismatch with common substrates used for crystal growth, fabricating InSb-based quantum wells is a daunting task. In fact, without due precautions, the build up of internal stress generates defects in the crystalline structure of the device which undermines its quality.
One way of getting around this problem is by accurately engineering a set of stress-compensating buffer layers [60–63]. This approach leads to high-mobility 2D electron systems, but, on the other hand, connecting the metallic leads is non-trivial. In fact, in order to induce a significant superconducting proximity effect on the system, the leads must be placed as close to the active region as possible, which in a quantum well with a wide barrier layer requires etching the barrier material in the contact regions prior to their deposition: this approach may compromise the charge mobility of the system. Alternatively, the electron gas can be contacted at the sidewalls of the mesa [64, 65].
It is worth to mention that relevant results [46, 64, 66] were obtained in recent years on aluminium-proximitized InAsSb quantum wells,[5] including the recent demonstration of a 2-site Kitaev chain [67]. However, fabricating high quality quantum wells remains extremely hard, and this makes this platform often unavailable.
The most common way of getting around internal strain is by growing free-standing 1D structures, which can relax the stress laterally during the growth procedure, not being subjected to lateral mechanical confinement. It is no surprise then that the most commonly used InSb nanostructure consists in InSb nanowires, which have been pivotal in the search for topological superconductivity (a review can be found in Ref. [68]) and which are still promising for the study of the behaviour of finite length Kitaev chains [69, 70].

5 In order to maximize the interface quality, epitaxial Al has been deposited in situ in the MBE chamber [66].

The main issue with working with nanowires is their one-dimensional geometry, which limits the device design possibilities and makes it more complicated combining them into a scalable architecture. In general, 2D geometries are much more versatile, e.g. allowing for the fabrication of Hall bars [38] or multiterminal Josephson junctions [71].
One of the goals of materials science research on InSb has been to find a way to exploit the versaltility of a 2D geometry on free-standing defect-free structures: a possible solution is given by InSb nanoflags.

3.3.2 *High mobility InSb nanoflags for quantum technology*

InSb nanoflags consist in thin crystalline flakes of indium antimonide which possess a sheet-like geometry and can be grown in a free-standing way, as shown in Fig. 16. The first report about them can be found in the works of De La Mata et al. [72] and Pan et al. [73]: they were grown on InAs stems in Molecular Beam Epitaxy facilities normally used to produce nanowires. The combination of the vapour-liquid-solid (VLS) growth mechanism in metalorganic vapour phase epitaxy (MOVPE) [74, 75] and selective-area growth was later demonstrated as a successful method for the growth of 2D InSb flakes, as well as, in more recent times, chemical vapour deposition [48].
Both the MBE and the MOVPE method are based on inducing a crystal twinning event in an initially 1D nanowire stem to trigger crystalline growth in a 2D fashion or, alternatively, on the merging process of two nanowires [75].
An alternative way of growing high-quality InSb nanoflags (depicted in Fig. 17) is based on Chemical Beam epitaxy, which allows directional control over the precursor fluxes, and was demonstrated by Lucia Sorba's group in Pisa.
By using InP tapered nanowires as stems in order to support the weight of the upcoming nanostructure[6] and carefully aligning[7] the precursor beams with respect to the stems, the group demonstrated the possibility of inducing the growth of

6 Previously utilized InAs nanowires displayed worse mechanical characteristics that resulted in bending and consequent misalignment during the InSb growth process.
7 Alignment is achieved making use of an in-situ RHEED (Reflection High Energy Electron Diffraction) apparatus.

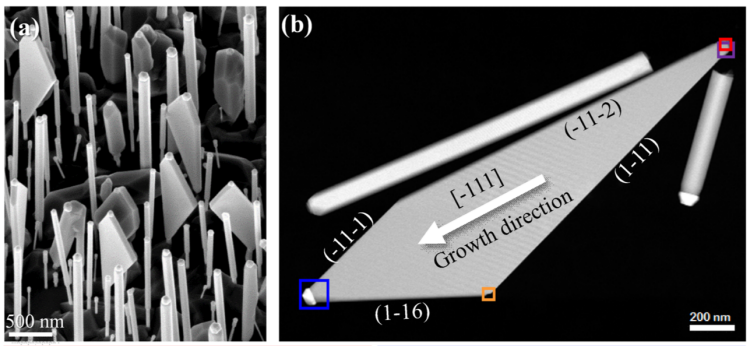

Figure 16: SEM (Scanning Electron Microscopy) images of the nanoflags grown by De La Mata et al. [72]; on the left: nanoflags attached to their growth substrate; on the right: SEM image of a single nanoflag.

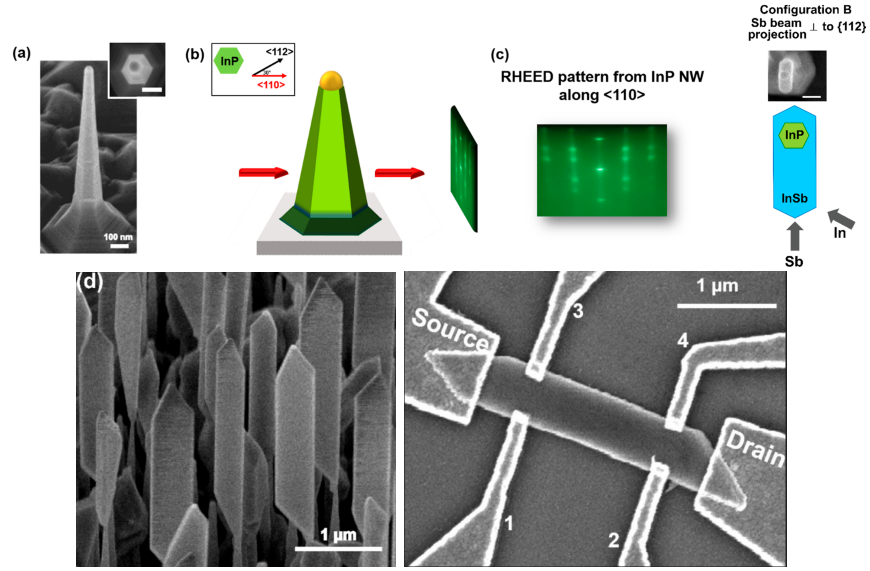

Figure 17: Alingnment procedure and directional growth of InSb nanoflags by Chemical Beam Epitaxy; below: SEM image of CBE grown InSb nanoflags; adapted from [38].

high aspect ratio defect-free InSb 2D nanocrystals. Crystals in the µm scale in two directions and with a typical thickness of 100 nm have been obtained, which have been fully characterized by both TEM analysis and transport measurements.
Low temperature (4 K) measurements of InSb nanoflag-based Hall bars resulted in field effect and Hall mobilities as high as $\mu = 29\,500\,\frac{cm^2}{Vs}$, corresponding to a mean free path of about $\ell_e \approx 500$ nm, sufficient to fabricate devices that work in the ballistic regime [38].
Different groups have investigated InSb nanoflag-based devices, demonstrating gate tunable proximity induced superconductivity [5, 32, 76] as well as electrostatic control over spin-orbit interaction [47, 77].
In fact, due to the strong planar confinement present in these structures and the asymmetry in the system due to the presence of the back gate which generates built in electric fields, strong Rashba spin-orbit coupling (as high as $\alpha = 0.42$ eVÅ) has been reported [78].
Our group has also reported full electrostatic control of the dissipation-less transport [5] as well as superconducting diode effect [79] in junctions defined by Ti/Nb superconducting contacts. More recently, in an InSb nanoflag-based Josephson Junction with Nb superconducting contacts[8], our group reported the presence of half integer Shapiro steps [80]. All of this contributed to proving the quality of these devices as high transparency weak links, making them ideal candidates for the search for exotic effects in ballistic superconductivity.

8 That is, without the Ti layer.

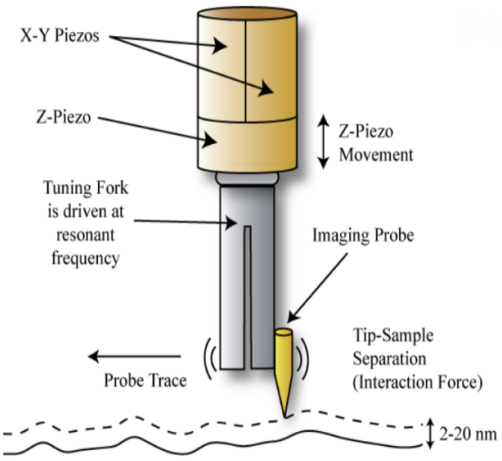

Figure 18: Tuning fork-based atomic force microscope; adapted from [83].

3.4 SCANNING GATE MICROSCOPY

3.4.1 *Historical note*

When designing and fabricating macroscopic objects, be it an engine or a building, engineers must investigate carefully the behaviour of each individual component, in order to be able to guarantee its safety, reliability and functionalities. It goes without saying that this trivial design rule should be kept in mind also in the nano-sized world.
However, due to the limited size of the devices under analysis, collecting local information with sufficient spatial resolution is no easy task and has become the subject of a specific branch of science spread across physics, chemistry, and engineering that goes under the name of Scanning Probe Microscopy.
The first result in the scanning probe field was the invention of the Scanning Tunnelling Microscope (STM) at the Zurich IBM laboratories in 1981, which eventually lead to assigning the 1986 Nobel prize to Binning and Rohrer, its developers [81].
Despite the potentiality of recording atomically resolved topography and local density of states maps, one of the main limitations of STM is that the sample has to be electrically conductive: STM cannot operate on insulators.
To be able to map the topography of insulating samples as well, the Atomic Force Microscope (AFM, depicted in Fig. 18) was conceived, still at the Zurich IBM laboratories, by Binnig, Quate, and Gerber in 1986 [82].
Its principle of operation is based on the mechanical interaction between an atomically sharp tip and the sample via van der Waals and Pauli repulsion forces, which are universally present and thus allow the application of the technique to any kind of sample. In the following years, AFM was taken as the starting point to develop many other scanning probe techniques: one of them is Scanning Gate Microscopy.

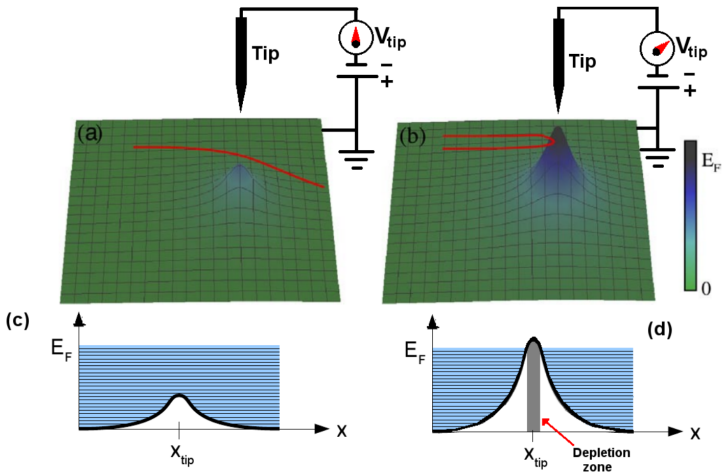

Figure 19: Principle of operation of SGM (a-b): polarising the tip modifies the potential landscape felt by charge carriers inducing backscattering; (c-d) bottom of the conduction band as a function of the position for different voltages applied to the tip; adapted from [85].

3.4.2 *Scanning Gate Microscopy*

Analyzing the topography of nanostructured devices is not the only application of SPM. Particular interest is devoted the study and manipulation of the electronic properties of matter at a local level, which is inside of the capabilities of an STM, but far beyond the scope of an ordinary AFM.
Nevertheless, AFM is suitable to be performed also on semiconductor-based devices at the basis of modern day electronics, and thus interest into upgrading the setup to perform electrical measurements sparked.
The first to conceive the idea of Scanning Gate Microscopy (SGM) was Weservelt's group at Harvard in the late 1990s [84]. The principle is straightforward: an AFM tip is capacitively coupled to a sample close by; therefore, when a potential difference is imposed between a semiconducting device and the tip, field-effect-driven accumulation or depletion of charge carriers in the region immediately below the tip takes place.
This way, a movable local scattering centre for charge carriers is obtained (Fig. 19), whose spatial dimensions vary depending on tip quality, tip-to-sample distance, and potential difference.
By current or voltage biasing the sample and recording its conductance response as a function of tip position, information can be obtained on the current density distribution in the sample as well as the presence, nature and location of defects and much more about the physics of the specific system under study.
This is of particular interest when the investigated sample is in the ballistic or mesoscopic regime, where quantum coherence effects are relevant and it is possible to explore tip-induced quantum interference effects.

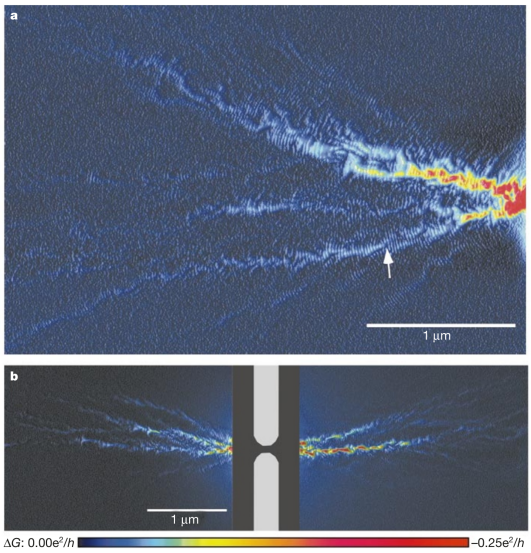

Figure 20: SGM map of the coherent electron flow across a quantum point contact; adapted form [4].

3.4.3 *State of the art*

The proof of principle of scanning gate microscopy [84] involved the manipulation of the electronic transport in a quantum point contact (QPC) defined in a GaAs-AlGaAs quantum well.
In a very short time, the full potentiality of SGM was eventually demonstrated by directly visualising the branched electron flow through an electrostatically defined QPC in a GaAs-AlGaAs quantum well [4, 86]. The most notable feature of this experiment was that for the first time imaging of coherent quantum electron flow was achieved: SGM maps clearly showed interference fringes spaced by half of the Fermi wavelength (Fig. 20).
Further measurements were able to determine the role of the background potential and of hard scatterers in the electron wave flow and to map the former by extracting the local Fermi wavelength from the local fringe spacing and the latter from the interference pattern [87–89].
In higher mobility samples and at lower temperatures (in order to achieve a sufficiently long thermal length)[9], it was eventually possible to visualise Fabry-Perot resonances [90] between the tip and a QPC, from which the spatial dependence of electron dephasing could be measured; furthermore, advancements in sample and apparatus quality paved the way to the study of the electronic equivalent of optical resonant cavities [91].
Other paramount achievements of SGM include direct visualisation of magnetic focusing in a 2DEG [92], and Quantum Hall edge states manipulation and tomog-

9 Here is a difference between the common notations in optical interferometry and electronics: in optical interferometry, no inelastic scattering is usually present. Therefore the name "coherence length" is usually associated to the maximum difference that two optical paths can have in order to preserve relative coherence. It is determined by the energy broadening of the source. In electronics, this goes under the name of "thermal length", whereas the "coherence length" is associated to the maximum electron path length along which self coherency is preserved. It is dominated by inelastic scattering.

raphy [93–97]. Furthermore, electron transport in two-dimensional materials like graphene [98–102] and $MoTe_2$ [103], carbon nanotubes [104–106], quantum dots [107–109], quantum rings [110] and nanowires [111] has been investigated through SGM as well.
Due to the extreme fragility of induced superconductivity to the presence of noise, performing SGM on superconducting heterostructures is a challenge few experimental setups in the world are capable to overcome.
To my knowledge, just three SGM experiments have ever been performed on superconducting devices so far.
In 2009 M. Huefner et al. [112] at ETH-Zurich investigated a superconducting single electron transistor based on an aluminium nanometric island, in a regime where no Josephson effect was present across the tunnel junctions connecting the dot to the electrodes.
In 2020 S. Bhandari et al. [113] at Harvard were able to image Andreev reflection in graphene in a single superconducting electrode architecture by exploiting cyclotron motion to spatially separate the particles impinging on the electrode from those reflected by it.
In 2024 Hegedus et al. [114] were able to study by SGM the effect of two-level defects as noise sources in solid state superconducting quantum systems.
None of the aforementioned experiments addressed the study of Josephson currents across superconducting weak links.

3.4.4 *SGM on Josephson Junctions*

The main purpose of SGM has been imaging normal state current densities with the following procedure:

- bias the device and measure the desired electrical signal in the tip's absence;
- place the tip close to the sample and polarize it to deplete the region immediately underneath, nullifying the current density in this region;
- by measuring the signal dependence on the tip position and subtracting its unperturbed value, the amount of current blocked by the tip and therefore the local current density can be determined.

Now the question is: can this procedure be generalized to supercurrent mappings? The only thing the tip can do is pushing a limited region of the sample into the normal state by depleting it, as depicted in Fig. 21; however, this means that the rest of the device remains in the superconducting state, effectively creating a parallel with zero resistance, that in electronics is known as a short circuit. In other words, in current bias the voltage drop is likely to be zero irrespectively of the tip position, unless one of these two situations occurs:

- the area depleted by the tip is so large that the entire junction is brought back to the normal state; this can happen due to bad tip quality, and it is detrimental to the experiment;

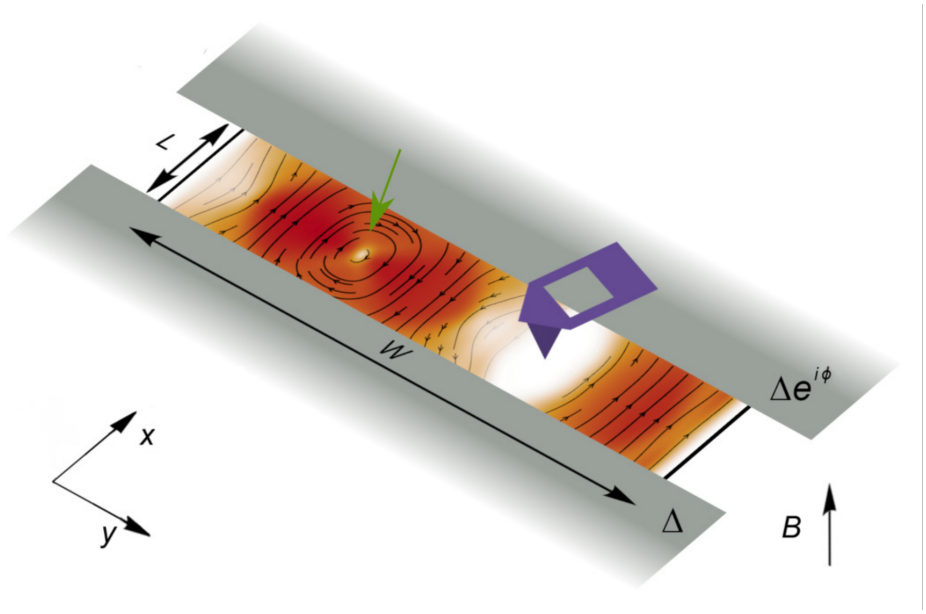

Figure 21: Scanning gate microscopy applied to a Josephson junction; adapted from [33].

- the changes induced by the tip potential in the scattering matrix of the junction are such that the critical current of the junction drops below the current bias, causing a switch to normal state.

The latter situation can be harnessed via the following measurement protocol, that allows the measurement of the critical supercurrent density:

- current bias the device and sweep the bias current to determine the junction's critical current in the tip's absence;
- place the tip close to the sample and polarize it to deplete the region immediately underneath, nullifying the supercurrent density in this region;
- sweep the bias current and measure a full I-V curve for each pixel. This allows to obtain the dependence of the critical current on tip position, and subtract it from the unperturbed critical current. The amount of supercurrent blocked by the tip and therefore the local critical supercurrent density can be determined.

These are the main ideas that set most of the framework to be able to image the junction's critical current density distribution; however, a crucial detail has been hidden under the rug, that makes data analysis of critical current SGM maps non-trivial: the superconducting phase difference can adapt to the presence of the tip, in order to achieve the maximum possible supercurrent at criticality.
This takes place in junctions with non-uniform local CPR or in presence of an external magnetic field. The latter case has been theoretically investigated in [33], and is briefly reported in the following paragraph.

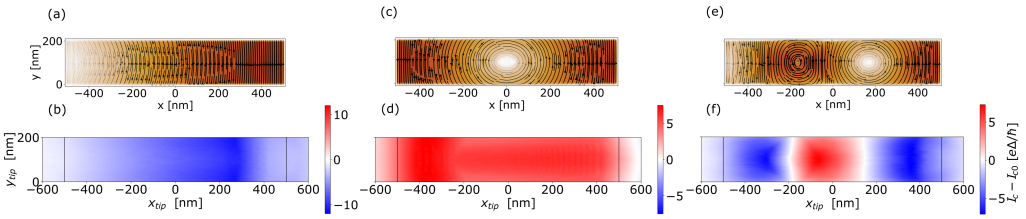

Figure 22: Simulations of SGM imaging of supercurrent distribution at various magnetic fields; in particular, conditions (a) and (e) (corresponding to fluxes equal to $\Phi_0/2$ and $3\Phi_0/2$ threading the junction) allow supercurrent imaging, while condition (c) (corresponding to a flux equal to Φ_0 threading the junction) prevents it; top: simulated supercurrent density field. bottom: simulated SGM signal map. Adapted from [33].

3.4.5 *Josephson vortex imaging*

Let us consider, for the sake of simplicity, a uniform short Josephson junction. In this situation, the system's behaviour in presence of an external magnetic field can be described with the following model [33]:

$$I_C = \max_{\Delta\phi} \int_{-\frac{W}{2}}^{\frac{W}{2}} J_C(y, y_{tip}) \kappa \left(\Delta\phi + \frac{2\pi B(2\lambda + L)y}{\Phi_0} \right) dy \tag{47}$$

$$J_C(y, y_{tip}) = J_0 \left(1 - \frac{1}{1 + \frac{(y - y_{tip}^2)}{d^2}} \right) \tag{48}$$

$$\kappa(\phi) = \frac{\tau \sin(\phi)}{\sqrt{1 - \tau \sin^2\left(\frac{\phi}{2}\right)}} \tag{49}$$

- the first equation (Eq. (47)) is equal to Eq. (39) and describes the critical current across the junction as the parallel of infinite one-dimensional junctions;
- the second equation (Eq. (48)) describes the presence of the tip as a modulation of the local critical current density. The depleted spot is described as a Lorenzian of width d;
- the third equation (Eq. (49)) is just the current phase relation for a short junction, already presented in Eq. (33).

Since the supercurrent density distribution is determined by the junction's CPR, being able to map it would allow to visualize the asymmetrical shape of the Josephson vortices.
The issue lies in Eq. (47), where the critical current configuration is identified as the one corresponding to the value of $\Delta\phi$ that maximizes the integral of the supercurrent density.
In absence of a magnetic field, $\Delta\phi$ corresponds to the superconducting phase difference across the junction, which is a well defined global quantity of the system. When a magnetic field is present, the superconducting phase difference can only be

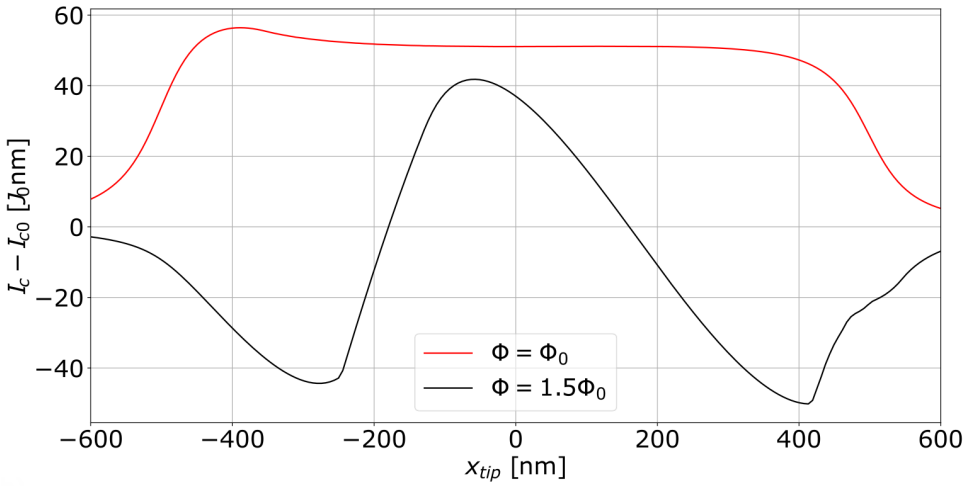

Figure 23: Simulations of SGM imaging of supercurrent distribution at two different magnetic fields; adapted from [33].

defined locally. This adds a degree of freedom to the system: in order to maximize the Josephson current, $\Delta\phi$ can now adapt to the presence of the tip by a rigid shift in the supercurrent spatial distribution [33].
If the system is perturbed by changing its phase difference by $\delta\phi$, the corresponding supercurrent change δI depends on the superconducting phase difference across the junction at the junction's extremes and in the region depleted by the tip. The total change in supercurrent driven by this perturbation can be expressed as

$$\delta I = I_{tip}(\Delta\phi) - I_{tip}(\Delta\phi + \delta\phi) + (J_{right}(\Delta\phi) - J_{left}(\Delta\phi))\frac{\Phi_0}{2\pi B(2\lambda + L)}\delta\phi, \quad (50)$$

where

$$I_{tip} = J_0 \kappa \left(\Delta\phi + \frac{2\pi B(2\lambda + L)y_{tip}}{\Phi_0}\right) d \quad (51)$$

is the supercurrent blocked by the tip and

$$J_{right,left} = J_0 \kappa \left(\Delta\phi \pm \frac{2\pi B(2\lambda + L)\frac{W}{2}}{\Phi_0}\right) \quad (52)$$

are the supercurrent densities at the left ($y = -W/2$) and right ($y = W/2$) edges of the junction respectively; a maximum is reached when the following condition is met

$$\frac{\delta I}{\delta\phi} = 0. \quad (53)$$

We first notice that, at low magnetic fields and with a tip of good quality, the depletion spot is much narrower than the Josephson vortex diameter:

$$d \ll \frac{\Phi_0}{B(2\lambda + L)}. \quad (54)$$

This implies that $\Delta\phi$ at criticality is determined almost solely by the effect of the edges and therefore approximately independent of the location of the tip, allowing

SGM supercurrent imaging, unless $J_{right}(\phi) - J_{left}(\phi) \approx 0$ independently from $\Delta\phi$.
The latter condition corresponds to being close to a minimum of the Fraunhofer pattern, and in that case $\delta I/\delta\phi$ is dominated by the effect of the tip. Therefore, the supercurrent distribution at criticality adapts to the presence of the tip, preventing the possibility of imaging it by SGM (Figs. 22 and 23).
In any other case, i.e., close to the Fraunhofer lobe maxima, the the supercurrent distribution at criticality cannot adapt to the presence of the tip, which allows the possibility to map the shape of Josephson vortices following the protocol described in Section 3.4.4.
Recently an alternative way of investigating supercurrent flow by scanning probe microscopy has been demonstrated: Yacobi's group at Harvard was able to map the supercurrent-generated magnetic field distribution close to a Josephson junction via a scanning probe magnetometer based on a single nitrogen vacancy in diamond [35]. Despite its undeniable potentialities, which include the possibility of mapping the supercurrent distribution in conditions different from criticality, this technique necessitates of samples displaying high critical current densities to create a sufficiently strong magnetic field to be detected. Besides, since the technique is based on zero interaction with the sample, manipulation of topological samples is impossible due to the intrinsic resilience of this systems to external perturbations.

4

MATERIALS AND METHODS

4.1 FROM METALORGANIC COMPOUNDS TO JOSEPHSON JUNCTIONS

4.1.1 *Growth of InSb nanoflags*

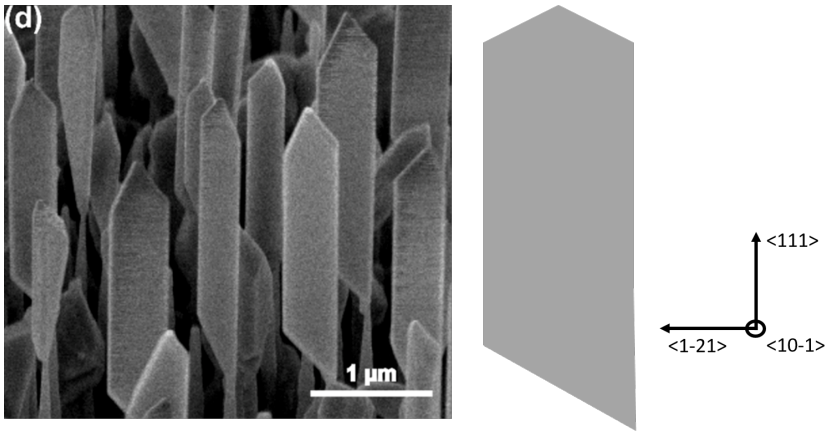

Figure 24: On the left: SEM image of InSb nanoflags grown by Lucia Sorba's group at Nest; adapted from [38]. On the right: schematics of an InSb nanoflag with crystallyne directions indicated.

The InSb nanoflags used for this work were grown by chemical beam epitaxy (CBE) from metal-organic precursors in a Riber Compact-21 system, by the group of Lucia Sorba [38]. Tapered Indium Phosphide nanowires (NW) are used to provide full support to the nanoflags. This strategy allowed to obtain InSb NFs about 2.8 ± 0.2 µm in length, 470 ± 80 nm in width, and 105 ± 20 nm in thickness, with {110} crystalline facets (as shown in Fig. 24).
Initially, tapered InP nanowires were grown on InP(111)B substrates via Au-assisted growth. Au particles with diameter of 30 nm dropcasted onto the bare substrate catalize the growth process.
The InP nanowire stems were grown with sample rotation, in order to ensure their uniform radial growth, for 90 minutes at 400 °C, with 0.6 Torr TMIn (trimethylindium) and 1.2 Torr TBP (tert-butylphosphine). Then the growth temperature was reduced by 30 °C (in presence of TBP flux only) to the InSb growth temperature.
The InSb nanoflags were grown without rotation, after aligning the ⟨112⟩ crystal direction toward the Sb precursor beam, as described in [38], initially for 30 min with 0.6 Torr TMIn and 2.3 Torr TMSb (trimethylantimony), and then for additional 60 min, linearly increasing the TMSb line pressure from 2.3 to 2.6 Torr, in order to enhance the asymmetric radial growth.

4.1.2 *Device fabrication*

Two different sets of devices were analysed in this thesis project. The first set, including sample SC7 and SC6, was fabricated by Dr. Sedighe Salimian in 2021, while the second set, including samples SGM1 and SGM3, was fabricated by Dr. Gaurav Shukla in 2024 following a similar recipe, which includes the following steps.
Firstly, the InSb NFs are drop casted onto a pre-patterned highly conductive p-type Si(100) substrate, which serves as a global back gate. A 285 nm thick SiO_2 layer covers the Si substrate as dielectric.
During the mechanical transfer, the InSb NFs are detached from the InP NW stems, and are randomly distributed on the surface of the substrate. In order to fabricate the devices, the position of selected InSb NFs was determined relative to predefined alignment markers using high resolution SEM images.
Considering the thickness and the edge geometry of the InSb NFs, Nb electrodes and additional reference markers were patterned on a 270 nm thick layer of ARO 679.04 resist with standard electron-beam lithography (EBL). Prior to metal deposition, the InSb native oxide was removed via a 30 s etching process in an optimized sulfur solution of $(NH_4)_2S_x$ (1 : 9 $(NH_4)_2S_x$: DI water at 40 °C). Then the samples were rinsed in DI water for 30 s. Next is the metallic film deposition via sputtering: samples SC6 and SC7 were fabricated with an older recipe that involved the deposition of a 10/150 nm Ti/Nb thin film with the titanium serving as a sticking layer; on the other hand, recent results [80] led to the belief that the use of titanium can be avoided: for this reason, fabrication of samples SGM1 and SGM3 involved the deposition of a 160 nm pure Nb thin film.
In any case, the deposition was preceded by an intense pre-sputtering on every used target and was followed by lift off in hot acetone.
After this, samples were glued with conductive silver paste to SGM sample-holders shown in Fig. 25, and the necessary electrical connections were established by Al wire bonding.
The SGM sample holder imposes strict constraints on the number of devices that can be bonded at the same time: 20 contact pins are available, but pin 12 has a built in connection to the back gate of the sample. Furthermore, only 14 lines are available for electrical transport. Finally, the bonding scheme of each sample must be accurately designed in order to be able to approach and operate the microscope without touching any of the wires.
Fig. 25 shows a typical sample at different length scales, starting from the SGM sample holder (0.35 in x 0.35 in); the top right quadrant contains a Scanning Electron Microscopy (SEM) image of the bonding pads frame (1.5 mm x 1.5 mm), which contains the sample frame (150 µm x 150 µm), where the fabricated devices and the Nb markers are located (shown in the bottom left quadrant); finally, the bottom left quadrant displays the SEM image of device SGM3 H4D2, one of the Nb-contacted nanoflag-based junction we studied in this thesis work (length $L = 190$ nm, width $W = 1420$ nm).

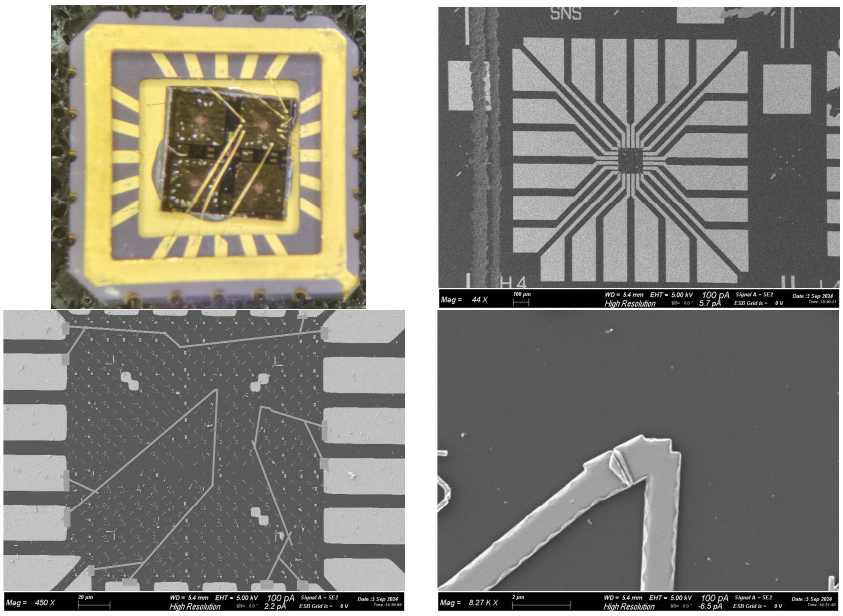

Figure 25: Top left: optical microscope image of the SGM sample holder; top right: SEM picture of a 1.5 mm x 1.5 mm bonding pads frame; bottom left: SEM image of 150 µm x 150 µm frame H4 with niobium marker system, sample SGM3; bottom right: SEM image of junction SGM3 H4D2.

4.2 AFM APPARATUS

In order to perform Scanning Gate Microscopy, a low temperature AFM infrastructure is necessary. This work made use of an Attocube attoAFMIII system based on low temperature tuning fork shear microscopy.
The main body of the microscope is made of titanium[1] and comprises two separate components that include the sample slot and the tip, respectively (Fig. 26).
Its principle of operation allows a completely electrical control of the system: a quartz tuning fork soldered to a printed circuit board (PCB, displayed in Fig. 27) is used as a mechanical oscillator; the fork is kept into vibration by a dither piezo motor which is continuously excited through an AC voltage signal of the desired frequency, while feedback information on the oscillation amplitude is simultaneously acquired from the tuning fork. Such electrical signal gets first amplified through a circuit situated on the PCB and containing a 10 MΩ resistor and a pseudomorphic HEMT capable of operating at low temperatures powered through a dedicated supply wire; then it gets amplified by a room temperature voltage preamplifier, and at last it gets recorded through a lock-in amplifier.
A several mm long and atomically sharp[2] tungsten tip is glued to one of prongs of the tuning fork: once near the sample, van der Waals interactions produce a drag onto the tip's oscillation that induces a shift in the resonance curve of the tuning fork towards lower frequencies. By keeping the driving frequency constant and equal to the free oscillation resonance frequency of the tip+tuning fork system, we observe the sample-to-tip interaction as a decrease in the lock-in oscillation

1 Titanium is a non-magnetic metal, allowing the operation of the apparatus in a high magnetic field environment.
2 Such tips are produced from tungsten wire by electrochemical etching.

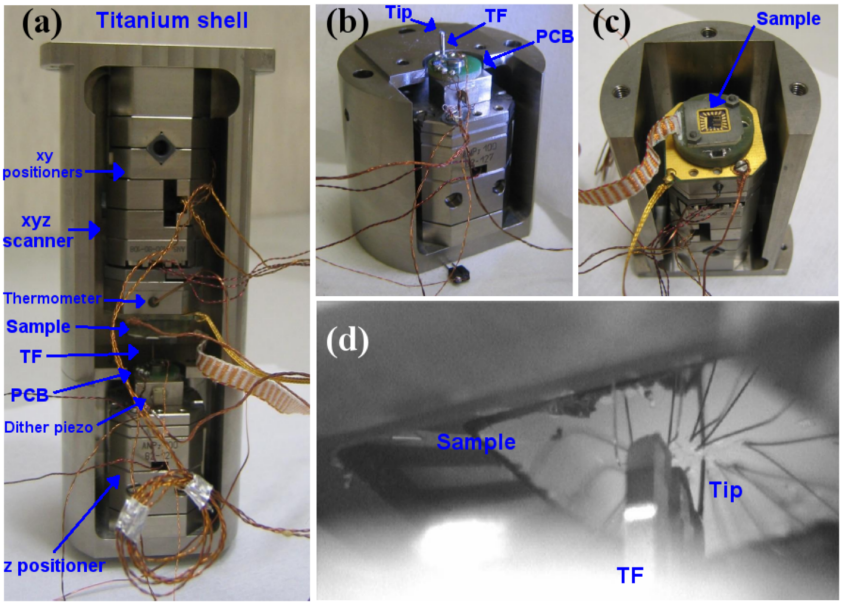

Figure 26: Internal structure of the microscope; a) fully mounted microscope head; b) tuning fork stage; c) sample stage; d) CCD camera picture of the system during an approach procedure: the reflection of the tip on the sample is used as a reference to determine the tip-sample distance and the tip position in the initial coarse approach phase; adapted from [115].

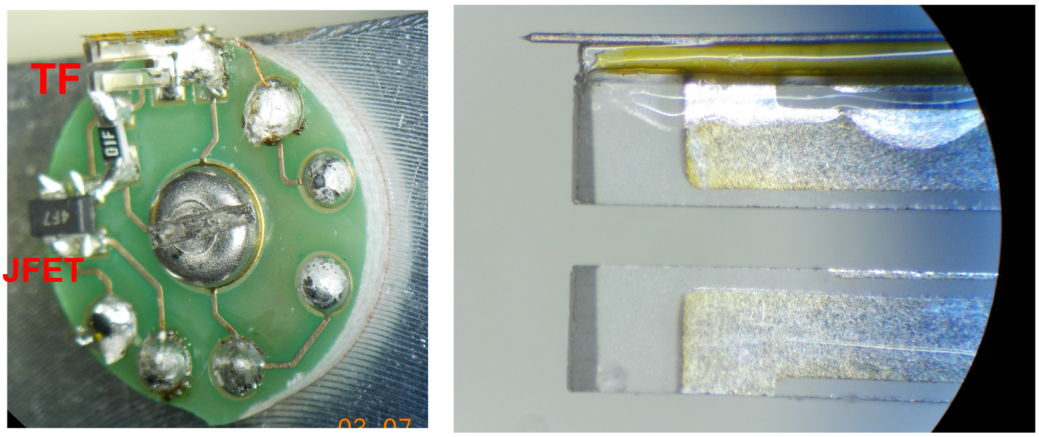

Figure 27: Left: tuning fork PCB; right: optical microscope image of the tuning fork and the tungsten tip; adapted from [115].

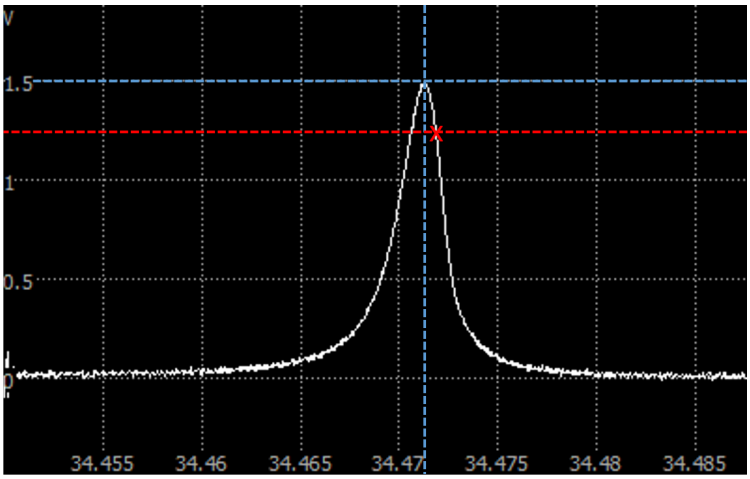

Figure 28: Resonance curve of the tuning fork at T = 300 mK. The blue lines indicate the resonance frequency and the free-oscillation signal amplitude of the tuning fork. The horizontal red line corresponds to the feedback setpoint: the high-frequency intersection between the resonance curve and the red line (indicated by a red x) corresponds to the tuning fork working point during the acquisition of topography maps.

amplitude signal. Due to the short range nature of van der Waals interactions, this effect takes place only when the tip is closer than 20 nm to the sample [116].
In order to perform AFM, the tip must be kept at a constant distance from the surface of the sample: a feedback loop is set in order to operate a z-axis piezoelectric scanner keeping the lock-in amplitude signal at a constant setpoint. The systems is set to react to drops in the lock-in signal by pulling away the tip from the sample and, vice versa, to reduce the tip to sample distance when the detected signal is greater than the setpoint; in order to avoid crashes, the driving frequency must be chosen to be equal or slightly greater than the resonance frequency of the system, as shown in Fig. 28.
Choosing a suitable feedback setpoint is of utmost importance as well: the tip-to-sample distance decreases with increasing difference between the free-oscillation signal amplitude and the feedback setpoint. At the same time, the feedback response time decreases with increasing steepness of the resonance curve at the feedback setpoint. A good rule of thumb consists in choosing a feedback setpoint of about 90% of the free-oscillation signal amplitude; this way, we are able to place the working point in a region where the steepness of the resonance curve is maximised while keeping at the same time the tip sufficiently far from the sample to avoid collisions.
The feedback system includes a Proportional (P) component aiming at reacting to sudden steps in the sample's topography and an Integral (I) component aiming at limiting the fluctuations of the signal around the setpoint. A Derivative (D) feedback component is absent since it would limit the reaction time of the system to a sudden change in topography, putting the tip at risk of crashing with the sample. On the other hand, this implies that fine tuning of the P and I parameters is required, to avoid either a slow feedback loop or uncontrolled oscillations around the setpoint.
The tip is electrically insulated from the rest of the tuning fork by a 200µm-wide

spacer section of optical fiber, with the additional purpose of broadening the tuning fork resonance curve[3]. The tip is connected at its base to electrical wiring used to electrically polarise it to perform SGM experiments.
Three piezoelectric motors have the purpose of effectuating coarse movements to reach any desired region of interest with the tip; they operate in slip-stick mode: a slow dilation and a rapid contraction (or vice versa) are alternated. The difference between static and dynamic friction coefficients ensures a net relative motion in the direction of the slow step of the two components connected by the piezo.
Two orthogonal slip-stick piezos for coarse motion in the x-y plane are located below the sample compartment, while the motor responsible for the z-motion is located below the tuning fork basis.
The latter is also responsible for the tip approach procedure: once the microscope is mounted, the tip is usually several millimiters away from the region of interest in all of the three principal axis directions; after having roughly positioned the tip manually with the help of a CCD camera, the automatic procedure to get the tip in contact with the sample comes into play:

1. the feedback loop gets activated and therefore the z-scanner extends the tip until either it reaches the sample (the feedback setpoint) or it gets to its maximum extension;

2. if the feedback setpoint is not reached, the z-scanner completely retracts the tip and the z-coarse positioner makes some steps in order to put the tip closer to the sample. The coarse positioner step must be at all times shorter than the maximum extension of the z-scanner to avoid tip crashes;

3. iterate from step 1 till feedback setpoint is reached.

Lateral movement during AFM operation is ensured by a couple of piezoelectric scanners attached to the basis of the sample stage. At room temperature they have a maximum range of 42 µm x 42 µm while at low temperature (300 mK) it gets reduced to 8.2 µm x 8.2 µm. This implies that in neither case it is possible to image the whole quadrant where the devices might be located, which is about 150 µm x 150 µm in size (see Fig. 25): it is necessary to employ a pattern of markers in order to be able to navigate the sample and to reach the device of interest.
The following external support electronics is necessary for the AFM operation;

- ASC500 microscope controller, the central control unit that manages all of the signal coming from and going to the microscope, in addition to communication with additional instruments;

- ANC150, the coarse positioners controller;

- Nanonis high voltage amplifier to drive the piezoelectric scanners;

- an external PC supplied with Daisy control software to operate the microscope and coarse positioners controller;

3 This is necessary in order to obtain a stable feedback since otherwise the oscillation amplitude would vary too quickly with the sample-to-tip distance [117].

- a room temperature voltage preamplifier to amplify the tuning fork oscillation signal.

Once the region of interest is reached at room temperature, the tip is retracted from the sample and put at a safety distance of about 500 μm from the sample in the vertical direction: the system is ready to be put under vacuum and cooled down.

4.3 CRYOGENIC EQUIPMENT

4.3.1 *Janis cryostat*

Most superconducting metals display critical temperatures that range from fractions to few Kelvin degrees: this field of research requires to have the ability to reach and maintain such temperatures for the time necessary for the experiment. This can be done thanks to complex equipment commonly known as cryostats.
Modern advancements in cryogenic technology have given rise to many different types of cryostats, each with its specific field of application and principle of operation: this thesis work made use of an 65L Janis ^{4}He bath cryostat to cool down the SGM apparatus to ^{4}He boiling temperature at atmospheric pressure, that is $T_{^4He} = 4.2\,K$.
This cryostat consists in a dewar containing an amount of cryogenic liquid sufficient to submerge the elements of the experimental setup in need to be kept cold. It comprises of two layers of thermal insulation:

- an Outer Vaccum Chamber (OVC);
- a super-insulating polymer layer.

In order to be able to safely host a low temperature AFM within it, this system must be as much vibration-proof as possible. The external wall of the OVC is kept acoustically insulated from the ground by industrial vibration dumpers, while the super-insulating layer was preferred to a pre-existing liquid nitrogen chamber due to the tendency of LN_2 to produce bubble-bursts when close to its boiling temperature.
A superconducting magnet made of a NbTi coil is placed at the bottom of the dewar in order to be completely submerged in cryogenic liquid: it is able to generate intense and uniform magnetic fields at its center without dissipating power due to its superconducting nature and consequent absence of the Joule effect.
Another superconducting component (a superconducting wire) is placed on the dewar's internal wall: only the submerged part displays the superconductive transition and therefore its resistance can be measured to infer the cryogenic liquid level.
Working with bath (or "wet") cryostats has its drawbacks:

- about once a week the experiment must be interrupted in order to refill the dewar with cryogenic liquid;
- it is extremely expensive due to the limited amount of ^{4}He available in the market and its ever rising price.

For these reasons, many laboratories (including NEST) have switched to more modern closed cycle "dry" cryostats that do not need a cryogen liquid bath in order to reach sub-Kelvin temperatures.
However, in the case of the SGM apparatus, this conversion is not so straightforward: in order to cool down, cryo-free systems use pulsed tube refrigerators, which inevitably introduce vibrations to the system. This must be avoided when working with an AFM since, in addition to limiting its spatial resolution, puts the tip at risk of crashing with the sample.
Therefore, it resulted more convenient to keep the existing "wet" system and to upgrade it with an efficient ^{4}He recovery system which is to be installed in the near future in order to greatly reduce the cryostat operative costs.

4.3.2 *LHe3 refrigeration stage*

All of the SGM apparatus, including the microscope, the sample and all of the related electrical connections, is contained in a structure designed to be inserted into the Janis dewar: the SGM insert (Fig. 29).
In addition to the electronic equipment, this section contains also additional cryogenic equipment that allows to reach temperatures lower than that of the LHe_4 bath, namely down to $T_{base} = 300\,mK$: the ^{3}He refrigeration stage.
Its principle of operation is the following: if a liquid and vapour phase coexist at thermal equilibrium, the temperature of the liquid phase is linked to its vapour pressure (the lower the pressure, the lower the temperature).
This implies that the temperature of the liquid phase can be lowered by pumping away the vapour directly above it. But why ^{3}He? This helium isotope has a boiling temperature at atmospheric pressure of 3.3 K, lower than that of the more common ^{4}He: it is thus more convenient to use LHe3 to reach low temperatures since at equal pressure its liquid phase is at lower temperature than its LHe4 counterpart, as shown in Fig. 30. However, due to ^{3}He cost and scarcity, it must be kept in a closed circuit.
In order to use L^{3}He, two obstacles must be overcome:

- how to liquefy ^{3}He (condensation);
- how to pump over L^{3}He (pumping);

In order to liquefy ^{3}He we must put it in thermal contact with a stage at a temperature lower than its boiling point. This is where the 1K pot comes into use: this is a chamber that receives a constant L^{4}He supply from the Janis dewar through a capillary and whose vapour pressure can be lowered by an external scroll pump in order for it to reach temperatures sufficiently low to liquefy ^{3}He that gets in thermal contact with it.
Once ^{3}He gets liquefied, it flows by gravity into the ^{3}He pot that is in thermal contact with the sample and the microscope.
Once in this conditions, the ^{3}He vapour pressure is reduced using an Active Charcoal Pump that exploits the phenomenon of adsorption: they consists in chunks of porous active charcoal that display on their surfaces binding sites for gas atoms.
The temperature of the charcoal controls the statistical occupancy of the relative

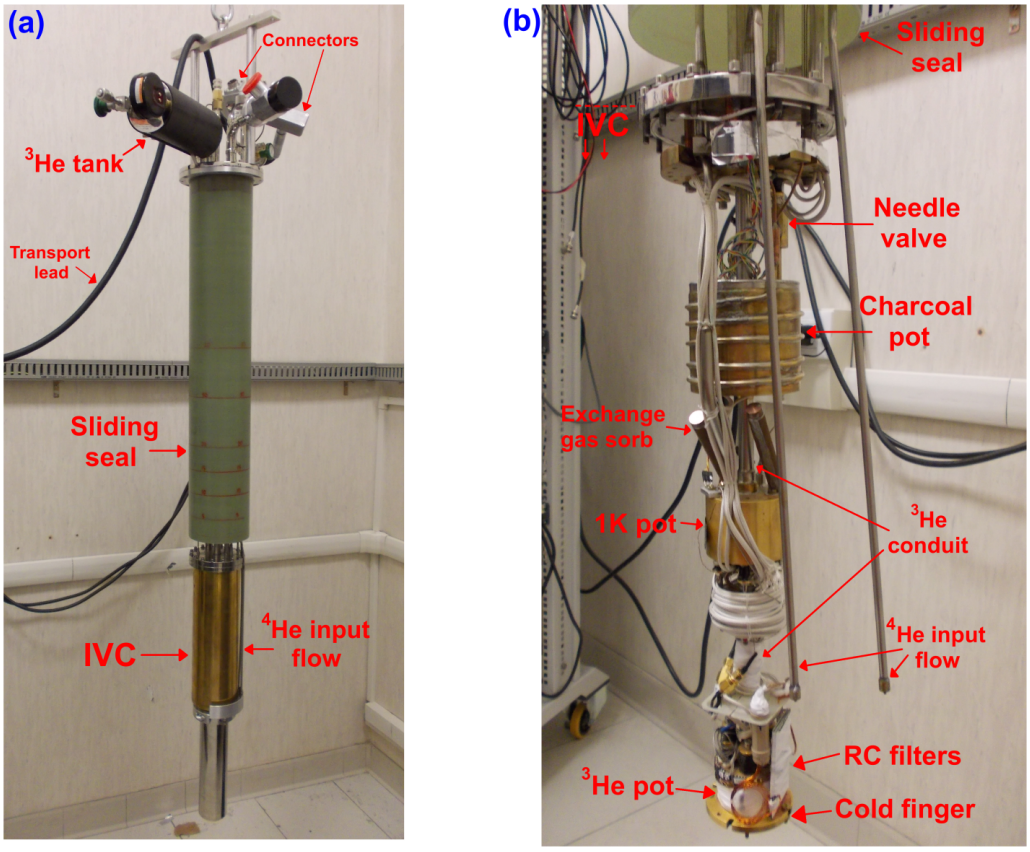

Figure 29: Pictures of the SGM insert exterior (left) and interior (right); adapted from [117].

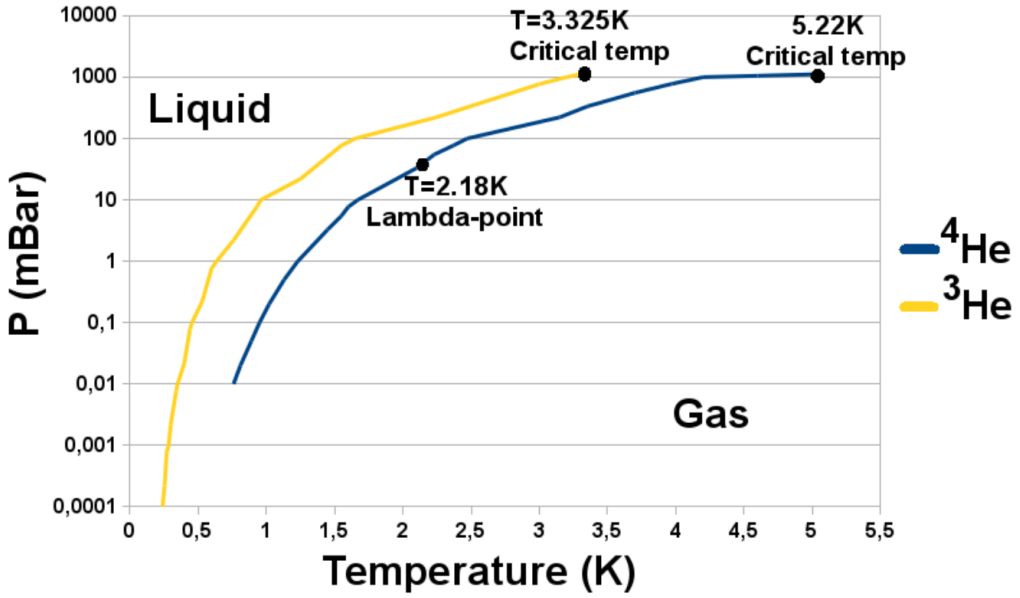

Figure 30: Vapour pressures of ^{3}He and ^{4}He; adapted from [118].

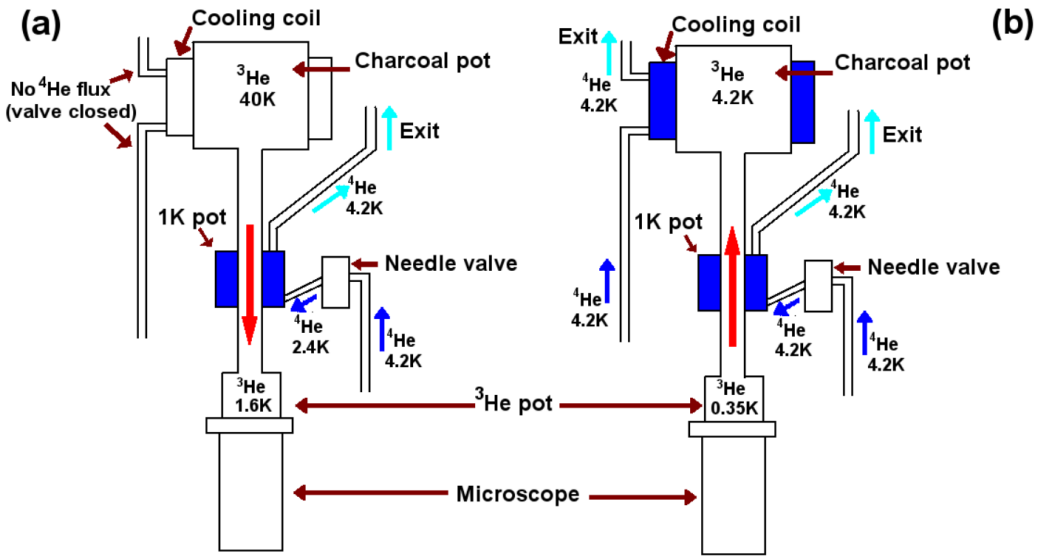

Figure 31: Schematics and operation of a ^{3}He refrigeration stage; adapted from [117].

binding sites: the lower the temperature, the more likely a site is to be occupied, the less likely (due to mass conservation) it is to find an atom in the vapour phase, and the lower is the vapour phase pressure.
This way, by controlling the charcoal pump through a heater and a LHe4 cooling system to respectively increase and decrease its temperature, it is possible to:

- make it release most of the ^{3}He atoms by heating it up to 40 K during the condensation step;
- make it adsorb the ^{3}He vapour by cooling it down to 4 K during the pumping step.

These procedures are schematized in Fig. 31. This system does not involve a continuous supply of L^{3}He to the liquid phase, which instead continues to evaporate due to the underpressure imposed by the charcoal pumps: this implies that after a couple of days the liquid phase is completely lost, the temperature of the system returns back to 4 K, and the condensation process must be repeated.
In order to thermally decouple the cold finger from the 4 K bath, most of the insert is contained in an Internal Vacuum Channel (IVC) that is kept in High Vacuum Conditions; in order to cool the insert down more quickly to 4 K, a tiny amount of ^{4}He gas is inserted in the IVC before cooldown. It gets removed automatically once the bath temperature is reached thanks to thermally activated sorption pumps that restore the high vacuum condition and therefore thermal insulation. Five thermometers allow to record the temperature of the various setup components. The first two are in contact with the charcoal pot and with the 1 K pot, respectively: they are mainly used to monitor the temperature of the relative components during the condensation procedure.
Two RuO_2 thermometers are placed close to the He3 pot and in proximity to the sample position. The last one is placed at the bottom of the dewar to monitor the superconducting magnet temperature.

4.4.1 *Electrical connections*

In order to perform an electrical measurement, it is necessary to put the instrumentation in electrical contact with the object of the study.
The SGM setup possesses, in addition to the connections necessary to operate positioners, scanners, tuning fork, and thermometry, 14 electrical lines available to connect the sample to external electronic equipment.

4.4.2 *Filtering*

Several noise sources are present in an electronics lab: black body radiation, Johnson noise, shot noise, 50Hz noise from the power grid, spourius coupling between the metallic leads and the sourrounding electronics. Superconductivity is extremely sensitive to the presence of high frequency noise, which can increase the electron temperature of the devices: in order to preserve it, every electrical connection, including the ones necessary for the operation of the AFM, must be filtered to reduce noise pick up and transmission as much as possible [117].
This is achieved by using three separate stages of filtering:

- a set of room temperature π-filters (electrical scheme is presented in the bottom section of Fig. 32) to filter out frequencies above 10 MHz;
- a set of low temperature π-filters to filter out frequencies above 10 MHz that can be picked up by the cables between the exterior and the cold region of the cryostat;
- a set of two-stage low-temperature RC filters (electrical scheme is presented in the top section of Fig. 32) with a cutoff frequency of $f_C = 2170\,\text{kHz}$ and a nominal signal reduction of 40dB per decade above such frequency ($R = 1\,\text{k}\Omega$ and $C = 47\,\text{nF}$).

All of this filtering effectively removes high frequency noise, but it is powerless against the equally detrimental low frequency noise such as the conventional 50 Hz introduced by the power supplies.

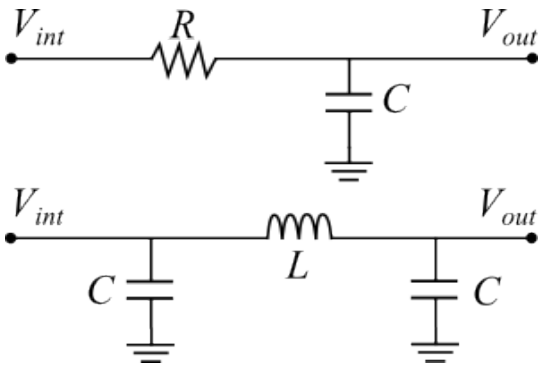

Figure 32: Schematics of a low pass RC filter (on top) and low pass π filter (at the bottom).

In order to avoid it as much as possible, all electrical connections are made through shielded LEMO, BNC, or twisted pair cables. Further attention is needed when setting up the electrical connections between the various electrical components, in order not to create "ground loops". The tip voltage line has one more precaution: a 10 MΩ resistor is placed between the voltage supply and the tip in order to limit the current flow to fractions of μA in case of a contact-induced discharge between the tip and the device.

4.4.3 *Instrumentation*

Here is a list of all of the instrumentation used during this Master's thesis project:

- SR830 Lock-in amplifiers: used to generate AC signals of a given amplitude and frequency while simultaneously detecting same frequency AC current or voltage signals measuring both the in- and out-of-phase components of the signal. In order to avoid noise pickup from the 50 Hz power supply lines, the chosen operating frequency is $f = 13.321$ Hz; as a signal reference lock-in amplifiers can take either their own output signal or an external reference: this allows to operate two amplifiers in sync and therefore to acquire simultaneously both current and voltage signals generated by the same excitation; they can also serve as frequency filtered preamplifiers, generating two distinct DC signals corresponding to the in-phase and out-of-phase component of the input, which can serve as input for additional electronic equipment;
- Keithley K2614B DC Voltage and Current source: used to generate DC voltage signals to drive the sample's back gate electrode or to generate DC current signals to drive the superconducting magnet;
- Yokogawa GS200 DC Voltage source: used to drive all of the DC current bias measurements. It has been preferred to the Keithley K2614B in this role since it is able to generate a more stable and clean electrical signal; on the other hand, the Yokogawa GS200 is able to generate a maximum output voltage of 30 V, while the Keithley K2614B can reach up to 200 V, which makes the Keithley ideal to operate the gate electrode;
- Keysight 34465A digital multimeters: used to measure DC voltage signals;
- SR560 voltage pre-amplifier: used to analogically amplify a voltage signal in order to make it more easily detectable by the multimeters; the preamp gain can be selected in the 1x to 10000x range;
- SR570 current pre-amplifier: used to analogically amplify a current signal on the orders of nanoAmperes, converting it into a voltage signal easily detectable by a digital multimeter. A typical conversion factor is 100 nA/V.
- ASC500 microscope controller DAC and ADC channels: this machinery possesses 4 DAC channels to generate analog voltage signals and 6 ADC channels that can be used as digital multimeters; in the experiments, only 2 DAC channels have been used, one to supply the power to the low temperature

preamp for the tuning fork signal and another to control the tip gating voltage; during SGM either 2 or 1 ADC channels[4] have been used depending on the measurement mode;

- National instrument NIDAQ data acquisition board: a high frequency (up to 5 KHz) data acquisition board that has been used for fast I-V curve data acquisition;
- Lakeshore 340 temperature controller: used to monitor the various thermometers of the setup and to operate the charcoal pump heater during the condensation procedure.
- Lakeshore 625 superconducting magnet power supply: used to turn on the superconducting persistent switch heater that otherwise would prohibit the operation of the magnet. Being designed to supply a magnet for high-fields applications, such power supply has a limited resolution in magnetic field (1 mT). For this reason, we have preferred to use the Keithley K2614B to supply the magnet in order to be able to operate with fields in the milliTesla range;
- a PC and a laptop with the aim of overseeing all the data acquisition process via Daisy and LabView software.

4.4.4 *Electronic measurement setups*

Most experiments are based on a simple principle: the aim is to record the response of the system to an external stimulus. Electronic transport measurements are no different: depending on what is the object of the investigation, different types of stimuli and signals must be generated and recorded respectively.
The main physical quantities in electronics are voltage drops and current flows: they are the natural choices to drive and record the device behaviour.
A typical device usually consists of a junction between two metallic niobium leads; each of these Nb leads splits into two different paths that reach different gold bonding pad and are bonded to different electrical lines. This is useful not only for redundancy, but also to implement multi-terminal measurement methods.

Four wire measurements

The most common, complete and precise way of acquiring an electronic transport measurement in our conditions is the so called four terminal geometry. It involves the use of two couples of terminals located at opposite sides of the device; one couple is used to impose a bias, the other to measure the response.
To be precise, our junctions comprise just two superconducting metallic leads, each one of which splits into two paths that are put in connection with the electrical lines. In order to differentiate this configuration with that in which devices are contacted by four separate leads, it is referred to in literature as *quasi-4-wire* configuration. However, for the sake of simplicity, in this work we will refer to it as *4-wire*

4 This is due to limitations in the data saving process of Daisy software.

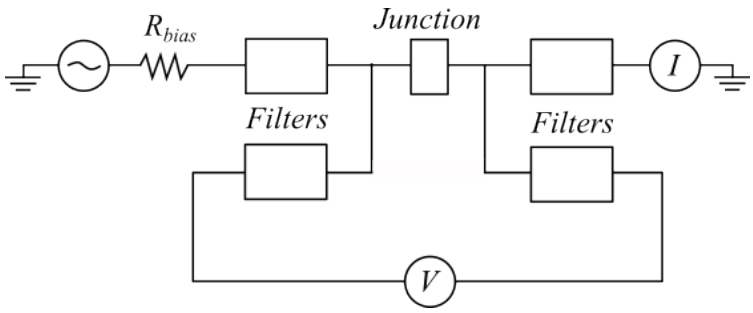

Figure 33: Four wire AC current bias measurement setup.

configuration.
Two setups have been used in this work:

- AC current bias: an AC current is injected into a source and extracted from a drain electrode, while two other electrodes are used to simultaneously acquire the voltage drop across the device; the setup is depicted in Fig. 33.
- DC current bias: the same as the AC current bias configuration, but in direct current. There is the possibility of either measuring the drain current or connecting the drain directly to the electrical ground, avoiding to measure it.

The current bias is obtained by applying a voltage bias to a known resistor R_{bias}. In case the drain current is not measured, in order to ensure the bias current to be approximately $I_{bias} \approx V_{bias}/R_{Bias}$, the bias resistance must be much greater than any other resistance in the system, specifically grater than the junction's resistance and the filter resistances. Being the filter resistance equal to 2 kΩ per line, our choice for the bias resistor is $R_{bias} = 10\,M\Omega$, which allows to operate without measuring the drain current directly whenever the investigated device is not pinched off[5].
Current biasing has been preferred in most cases to voltage biasing because it led to more stable and clean measurements.

Three wire measurements

When there is no possibility of performing four wire measurements due to one electrical connection being severed, it is possible to use a three wire setup, in which the source electrode is used for both injecting the bias current and measuring the voltage drop. The main drawback of this method is that the measured voltage drop includes also the drop across the filters of the line connected to the source electrode, which must be removed in post-processing.

Two wire measurements

In other conditions, there is no possibility of having more than two electrical connections with the junction. In this case, both the drain and the source electrode must be shared between the biasing and the measurement branches (as depicted in Fig. 34), and the recorded voltage drop includes the sum of the drops across the

5 Pinch-off is the condition in which the conductance of a semiconductor-based sample drops to zero due to gate-induced charge carrier depletion.

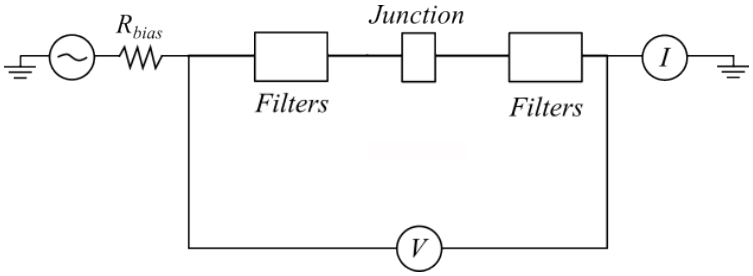

Figure 34: Two wire AC current bias measurement setup.

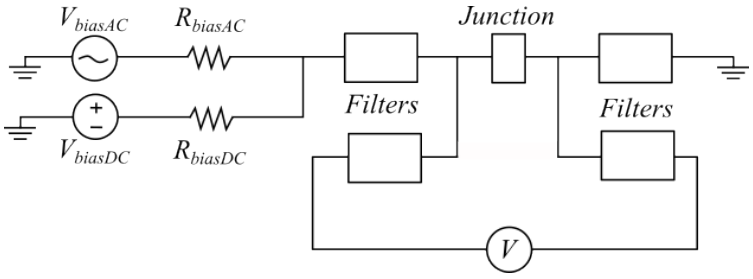

Figure 35: AC+DC four wire current bias measurement setup

filters of the source and drain lines, which must be removed in post-processing.
Two wire DC voltage bias measurements have been performed in order to characterise the behaviour of one of the devices; in this case, a 1/1000 voltage divider has been used to reduce the voltage supply signal to a value bearable for the junction and to increase voltage bias resolution.

Combined AC+DC bias

Another possibility is that of imposing a combined AC and DC current bias. In this case, a four wire setup is used, and two different bias resistors are connected on one side to a common source line and on the other side to an AC and a DC voltage source respectively (as displayed in Fig. 35).
If the AC bias is much smaller than its DC counterpart and the device working point is such that its relative differential resistance variation due to the AC excitation is negligible

$$\frac{d^2V_{DC}}{dI_{DC}^2} I_{AC} \ll \frac{dV_{DC}}{dI_{DC}} \tag{55}$$

then the differential resistance can be directly measured by recording the AC component of the voltage drop across the device:

$$\frac{dV_{DC}}{dI_{DC}} = \frac{V_{AC}}{I_{AC}}. \tag{56}$$

This condition can be reached by choosing the bias resistors (R_{biasAC} and R_{biasDC}) and voltage supply outputs (V_{biasAC} and V_{biasDC}) of the AC and DC branch accordingly:

- both R_{biasAC} and R_{biasDC} must be greater than any other resistance in the system, mainly the junction resistance and the filter resistance, in order to have a constant current flowing across the device;

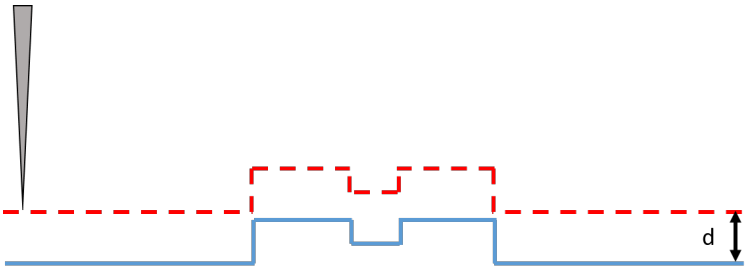

Figure 36: Dual Pass mode principle illustrated.

- $R_{biasAC} \gg R_{biasDC}$ when using voltage supply outputs of similar order of magnitude $V_{biasAC} \approx V_{biasDC}$.

Scanning Gate Microscopy measurements: normal state

It has been useful to perform normal state[6] SGM on the investigated devices, in order to verify that the tip is correctly connected and the device responds to it. These measurements have been performed either in AC or DC current bias configuration, and the sample resistance has been recorded as a function of the tip position. Two ways of scanning the charged tip over the region of interest have been investigated:

- Dual Pass mode is an operation mode that is already built in the Daisy microscope controller software and consists in performing a double raster scan (Fig. 36):
  1. At first, one line of topography signal is acquired (forward and backwards): the tip is in contact with the sample[7] and is kept grounded while doing this, in order to prevent discharges;
  2. then the tip stops, and the tip is lifted up from the sample by a given amount; after the tip gets lifted, there is the possibility of activating some "Alternatives", such as generating a signal from one of the DAC channels of the microscope controller: in the case in question, a selected voltage value was used to polarise the tip;
  3. after a user-selected wait, the tip performs a second line scan maintaining a constant distance from the device equal to the lift value, using as a reference the previously recorded topography signal;
  4. alternatives get deactivated, the tip is put again in contact with the sample and after the user-selected wait interval, the following topography line of the raster scan is acquired.
- Flying mode (depicted in Fig. 37) is an operation mode that requires a previously acquired reference topography map of the scan area; in this protocol, the tip is never in contact with the sample and, for this reason, no simultaneous topography is acquired. The reference topography is used to determine the

6 We define the system to be in the normal state if it does not support supercurrent flow. This implies that either the temperature of the system is above its superconducting transition, or the current flowing across the junction is greater than the critical current.

7 Here we are implying that the tip is kept at a distance from the sample determined by the AFM feedback loop, not that it is actually scratching the sample.

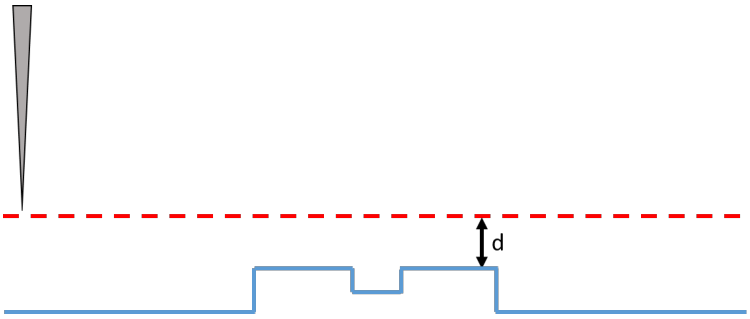

Figure 37: Flying mode principle illustrated.

highest point of the sample. Then the tip extension is limited to a maximum value equal to said reference minus a safety distance. After having polarized the tip, it can be scanned over the region of interest while simultaneously acquiring the desired electrical signals.

Both Dual Pass Mode and Flying mode have their advantages and disadvantages. Dual Pass mode is great since it ensures that the tip is always kept at a constant distance from the sample, which allows to operate SGM safely at a small distance from the sample, reducing the size of the induced depletion spot and therefore increasing the SGM resolution; on the other hand, a Dual Pass measurement takes at least twice the time of a flying mode measurement, without considering the necessary waiting intervals: due to the electrostatic interactions between the tip and the backgate, every time the voltage of the tip is changed, it influences the oscillation of the tuning fork and therefore the feedback loop; in order to safely operate, it is necessary to wait for the system to reach equilibrium after this sudden perturbation. This can take as long as 25 s, depending on the tip and tuning fork under use: for a scan of 100 rows this implies that, provided a normal topography map takes 30 minutes, a Dual pass map would take 2.5 hours.
Flying mode is way faster, it takes no longer than a usual topography scan. However, in order to safely operate, the tip is kept indicatively about 100 nm more distant from the semiconducting region of the junction than in the Dual Pass mode. This affects the SGM resolution.

Scanning Gate Microscopy measurements: supercurrent modulation

Performing critical current maps is far less straightforward than normal state SGM since it requires to measure for every position of the tip at least a whole current-voltage curve.
The AFM software does not allow the possibility of performing such pixel-by-pixel actions for both methods reported in the previous section.
There is, however, another built-in operation mode in the Daisy software: Path mode, which consists in selecting a set of positions in the scan range (usually distributed on an evenly spaced grid or along a line).
At each of the given positions there is the possibility of performing different kinds of actions, including communicating with external equipment through a dedicated TTL channel.
The chosen protocol is the following:

1. a reference topography is taken;
2. a set of tip positions is selected in path mode;
3. the tip extension is limited in the same way as described in the Flying mode in order to avoid contact between the charged tip and the sample;
4. a gating voltage is applied to the tip;
5. Path mode is started: the tip reaches its first position;
6. 5 seconds wait to eliminate any transient behaviour[8];
7. a TTL signal is sent from the microscope controller to a NIDAQ acquisition board, triggering the acquisition of an I-V curve;
8. once acquisition is completed, a TTL signal response is generated by the NIDAQ acquisition board, which triggers the movement of the tip to its following position.

In order to acquire I-V curves, a sawtooth voltage signal is generated by the NIDAQ output to drive a current bias in the device while the NIDAQ input channel acquires simultaneously the relative voltage drop; all of this takes place at a much higher rate with respect to all of the other instruments available[9]. This approach has been used to acquire current versus voltage curves as the tip is scanned over the device, a process that would take several more hours with different instrumentation.

8 Due to the I-V data saving process, the software controlling the NIDAQ acquisition board causes a brief downtime that impedes the correct reception of TTL signals: this delay is crucial to maintain the correct communication between the two components.

9 ... with the exception of the ASC500 microscope controller DAC, that could be a valid alternative to be investigated in future work.

5 JOSEPHSON JUNCTION CHARACTERIZATION

In this chapter we report on the quantum transport measurements performed in this thesis work. This will allow to ensure the correct behaviour of the fabricated devices and to compare their performance with previous work.
Unless explicitly indicated, experiments were performed in the SGM Janis cryostat at a temperature of 300 mK.

5.1 BACK-GATE-INDUCED CONDUCTANCE MODULATION

As a first step, it is necessary to assess whether or not devices correctly respond to the application of a voltage difference between the junction and the back-gate (later referred to as "back-gate voltage" or V_G).
Due to the high operative costs of wet cryostats, it is convenient to make sure of the proper operation of the devices before cooling them down to LHe temperatures; the fastest and cheapest way to perform these tests is cooling down the investigated sample to $T = 77\,K$ by placing it into a dip stick inserted into a LN_2 dewar.[1]
The conductance of the devices is determined by simultaneous measurement of the current and the voltage difference across the device in a 100 nA AC current bias configuration. Let us take as an example the 4-wire measured back-gate conductance modulation curve of device SGM1 D9D1 reported in Fig. 38. By qualitatively analysing this data, the following main features can be identified:

- the junction's conductance increases with increasing positive back-gate voltage, indicating that the InSb region of the junction behaves as an n-type semiconductor; this is aligned to our expectations concerning the action of the surface sulphur treatment performed prior to the deposition of metallic leads (see Section 4.1.2);
- at negative back-gate voltages $V_G < 0$ the device reaches a pinch-off condition, i.e., its conductance goes to zero. This corresponds to complete depletion of the semiconducting region and is the best indicator of the absence of a metallic short across the device;
- an hysteretic behaviour is present: for rising back-gate voltages the conductance is always higher than in their descending counterparts.

In order to perform a quantitative analysis of the collected data, we have adopted the approach reported in Ref. [119]. Let us consider the resistance of the device as the sum of two contributions:

$$R = R_{con} + R_{channel} \tag{57}$$

1 It is worth to mention that room temperature testing is also possible, but, due to thermal energy broadening, devices do not display pinch off in these conditions.

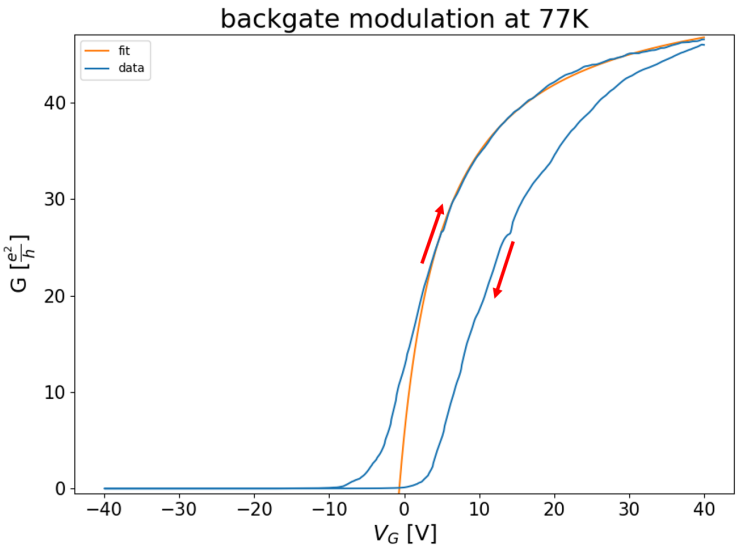

Figure 38: Lock-in measurement of sample conductance as a function of the back-gate voltage. Device SGM1 D9D1; fit results: $\mu = 8557 \pm 34 \frac{cm^2}{Vs}$; $R_{con} = 485.2 \pm 0.1\Omega$; uncertanties estimated as the standard deviation of fits performed over consecutive measurements on the same device.

R_{con} is a contribution independent of the back-gate voltage and corresponds to the contact resistance of the device, giving insight about the Nb-InSb interface quality; while $R_{channel}$ is a gate-dependent resistance that takes into account the gate- induced charge carrier density modulation; the characteristic equations of field effect transistors state that this contribution is equal to

$$\frac{1}{R_{channel}} = \frac{nWt\mu}{L}, \tag{58}$$

where n is the charge carrier density into the channel, L is the junction length, W its width, t its thickness, and μ a device-dependent effective mobility; furthermore, the charge carrier density is determined by the capacitive coupling between the junction and the back-gate

$$n = \frac{C(V_G - V_{th})}{t}, \tag{59}$$

where C is the back-gate to junction capacitance per unit area and V_{th} a device-dependent threshold voltage; to sum up, we obtain

$$R_{channel} = \frac{L}{CW\mu(V_G - V_{th})}. \tag{60}$$

Following this model, the junction's conductance takes this form:

$$G = \frac{1}{R_{con} + R_{channel}} = \frac{1}{R_{con} + \frac{L}{CW\mu(V_G - V_{th})}}. \tag{61}$$

In this equation, L, W and C are known quantities: L and W can be determined from SEM images of the junction, while C has been measured in Ref. [38] in similar

device	L [nm]	W [nm]	$\mu[\frac{cm^2}{Vs}]$	$R_{con}[k\Omega]$	critical current
SGM1 D9D1	150 ± 10	670 ± 10	8557 ± 34	0.4852 ± 0.0001	> 10 nA
SGM1 D8D1	180 ± 10	1530 ± 30	16670 ± 60	0.5721 ± 0.0001	90 nA
SGM1 D8D2	188 ± 10	610 ± 10	12300 ± 300	0.758 ± 0.002	80 nA
SC7 D4D4	400 ± 20	400 ± 20	11900 ± 100	1.49 ± 0.001	no

Table 1: Report of the 77 K characterization of the devices that have been also measured at 300 mK. The last column of the table indicates the critical currents devices displayed at 300 mK. Devices SGM3 H5D1 and SGM3 H4D2, which will be mentioned in the following section, have not been characterized at 77 K.

samples, obtaining the following value $C = 10\,\frac{nF}{cm^2}$. Therefore, this model has three unknown parameters to be determined by fit of the experimental data: μ, V_{th} and R_{con}.
Numerical least squares fit has been performed on the rising slopes of the back-gate conductance modulation curves, whose results are reported in Table 1. The main advantage of this method is that it is directly applicable to any measurement setup (4-wire, 3-wire, or 2-wire). The only difference is that in the latter cases R_{con} takes into account also the resistance of the transport lines, which has to be subtracted from it a posteriori in order to compare measurements taken on different devices using different setups.
The described procedure has proven to be useful as a first figure of merit of the quality of the devices. Fit-obtained mobilities higher than $10000\,\frac{cm^2}{Vs}$ and contact resistances lower than $1k\Omega$ have been found to be linked to the presence of Josephson currents at $T = 300$ mK and therefore with high quality devices, as reported in Table 1.
It is worth to mention that the obtained device-dependent effective mobility does not correspond to the electron mobility of InSb nanoflags reported in Ref. [5], which is a material-dependent property. In fact, the latter is defined in the diffusive regime and is measured in μm-long Hall bar devices, while the dimensions of our junctions ensure that their behaviour is ballistic.
In order to understand that, we can determine the effective mean free path ℓ_e of junction SGM1 D9D1 from its effective mobility: by applying the Drude model formula for the mean free path $\ell_e = \frac{\mu m^\star v_d}{e}$, where $m^\star = 0.018 m_e$ [45, 52, 53] is the effective mass of the charge carriers and $v_d = 1.5 \times 10^6\,\frac{m}{s}$ is the InSb drift velocity (assumed to be equal to the typical Fermi velocity in InSb nanoflags) [5], this results in $\ell_e = 131 \pm 5$ nm, which is comparable to the junction's length of $L = 150 \pm 10$ nm.
Therefore, the system is not in the diffusive regime and the value of μ obtained through the fit does not represent in a faithful way the electron mobility in the material, which explains why it is not compatible with the much higher value reported in InSb nanoflags-based Hall bars [38].

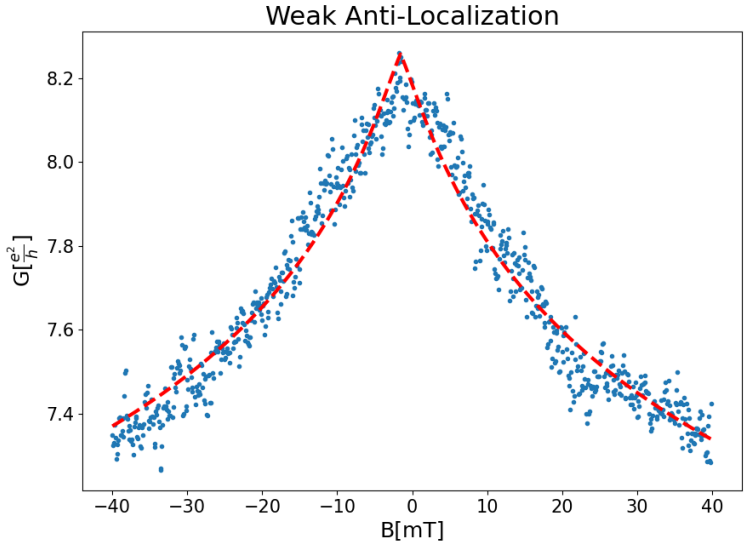

Figure 39: Weak Anti Localization: zero-field peak in the measured magnetoconductance. Back-gate voltage $V_G = 8\,V$; red dashed curve: least squares fit following the chosen theoretical model; device SC7 D4D4.

5.2 SPIN-ORBIT COUPLING: WEAK ANTI-LOCALIZATION

In presence of Rashba spin-orbit coupling (see Section 3.2.1), the momentum of any particle of given energy univocally determines their spin; in particular, due to time reversal symmetry, particles with opposite momenta must also possess opposite spins.
This implies that, in order to be elastically backscattered by an impurity, charge carriers must also experience a spin flip: in absence of external magnetic fields or magnetic impurities, which can act directly on the spin degree of freedom of the particle, this suppresses the elastic backscattering probability. Once an out of plane magnetic field is switched on, backscattering events become gradually more probable, increasing the sample resistance. This phenomenon is known as Weak Anti-Localization (WAL) and has already been studied in InSb nanowires [120] and nanoflags [47, 77].
Here, the first Weak Anti-Localization measurement on NEST-grown InSb nanoflags is reported. The investigation was performed on device SC7 D4D4, which did not display any superconductive behaviour at $T = 300\,mK$, consistent with its characterization at 77 K (reported in Table 1). The presence of elastic scattering centres is a requirement for the observation of WAL: previous measurements performed on different devices did not show any sign of WAL, which is consistent with the ballistic nature of such devices.
Magnetoconductance measurements have been acquired at various back-gate voltages in a 2-wire DC current bias configuration; filter resistance equal to 4 kΩ has been subtracted from the data prior to performing any analysis.
An example magnetoconductance curve is reported in Fig. 39: it displays, as expected, a sharp maximum close to zero field.
Weak Anti-Localization is described in a quantitative way in the diffusive limit by

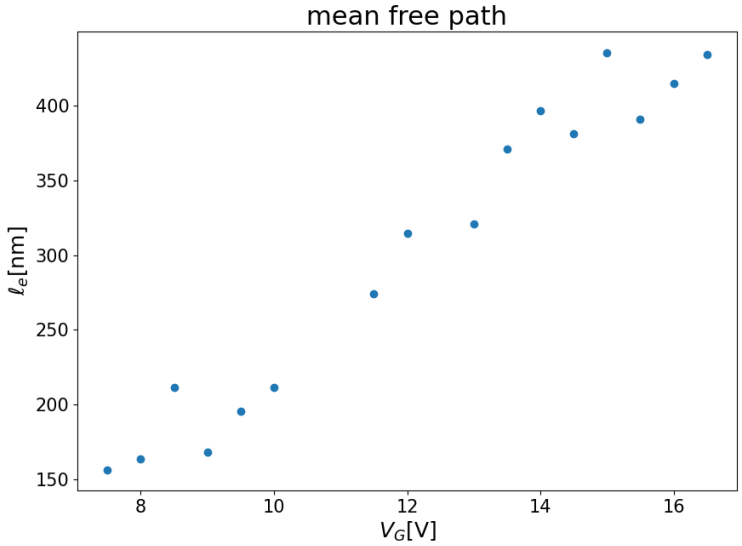

Figure 40: Mean free path as a function of back-gate voltage; device SC7 D4D4, T = 300 mK.

the Hikami-Larkin-Nagaoka (HLN) theory [121], which states that the deviation from the zero field conductance takes the following form:

$$\Delta G(B) = -\frac{e^2}{\pi h}\left(\Psi_{digamma} + \Psi_{log}\right) \tag{62}$$

$$\Psi_{digamma} = \frac{1}{2}\upsilon\left(\frac{B_\phi}{B} + \frac{1}{2}\right) + \upsilon\left(\frac{B_e}{B} + \frac{1}{2}\right) - \frac{3}{2}\upsilon\left(\frac{4B_{so}}{3B} + \frac{B_\phi}{B} + \frac{1}{2}\right) \tag{63}$$

$$\Psi_{log} = -\frac{1}{2}\log\left(\frac{B_\phi}{B}\right) - \log\left(\frac{B_e}{B}\right) + \frac{3}{2}\log\left(\frac{4B_{so}}{3B} + \frac{B_\phi}{B} + \frac{1}{2}\right) \tag{64}$$

where υ is the digamma function and $B_{\lambda,\phi,so}$ are three parameters connected to the material's mean free path, coherence length and spin orbit length respectively:

$$B_{e,\phi,so} = \frac{\hbar}{4eL^2_{e,\phi,so}} \tag{65}$$

Finally, the spin orbit length is linked to the Rashba parameter $\alpha = \frac{\hbar^2}{m^\star L_{so}}$ [47].
The acquired magnetoconductance curves have been fitted with the HLN formula: in order to avoid overfitting, just two fitting parameters have been considered (B_ϕ and B_{so}) while B_e has been measured by extracting the mean free path from the zero field resistance minus the contact resistance $R_{channel} = R - R_{con}$ following the Drude model:

$$\ell_e = \frac{m^\star v_d L}{C(V_G - V_{th})R_{channel}W} \tag{66}$$

where, for this device, $W = L = 400 \pm 20$ nm, $v_d = \frac{\hbar}{m^\star}\sqrt{\frac{2\pi C(V_G - V_{th})}{e}}$ the Fermi velocity of the nanoflag, and $V_{th} = 5$ V has been extracted from the back-gate conductance modulation curves of the device. The dependence of the so-obtained mean free path on the back-gate voltage is reported in Fig. 40. As expected [38], ℓ_e increases with back-gate voltage and is of the order of the hundreds of nanometers.

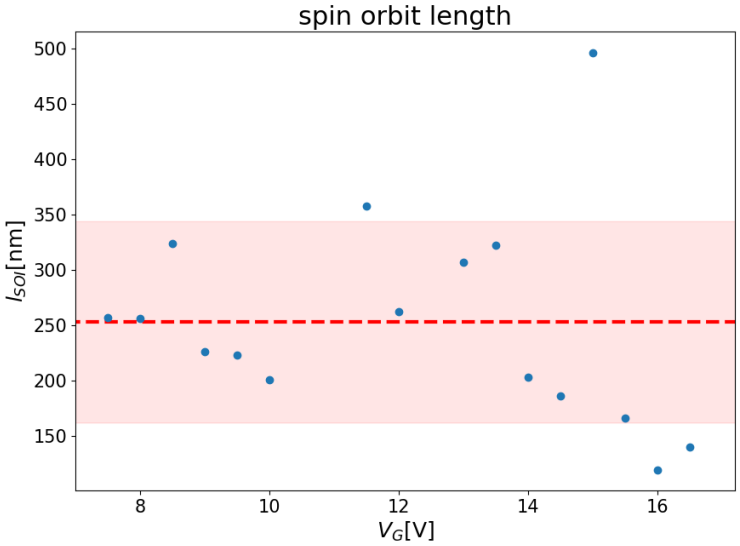

Figure 41: Spin orbit length as a function of back-gate voltage; device SC7 D4D4, T = 300 mK.

The least squares fit results as a function of the back gate voltage are reported in Fig. 41 and Fig. 42.
The spin orbit length does not display any evident dependence on the back-gate voltage and assumes a typical value of $L_{SO} = 252 \pm 90$ nm, corresponding to a Rashba coefficient of $\alpha = 0.17 \pm 0.05$ eVÅ, which evidences the presence of strong spin-orbit interaction. This value is in agreement with those reported by Xu's group [77, 78] in similar devices.
The coherence length, on the other hand, displays an unexpected downward trend that can be explained as a spurious negative correlation to the mean free path.
Furthermore, the coherence length is determined by the occurrence of inelastic scattering events, while the mean free path takes into account both elastic scattering events (assumed to be dominant at low temperature) and inelastic events: obtaining a coherence length shorter than the mean free path has no physical meaning.
In any case, the order of magnitude of the obtained coherence length is some hundreds of nanometers as well, underlining the good quality of the InSb nanoflag.
It is worth to mention that all of the derived characteristic lengths are compatible with the dimensions of the devices: we are close to the limits of applicability of HLN theory. Furthermore, this kind of analysis has been proven to be difficult due to the large correlations between the fit parameters [122]. Therefore, these measurements are not meant to be precise quantitative evaluations, but, as already noticed, give results consistent with our expectations.

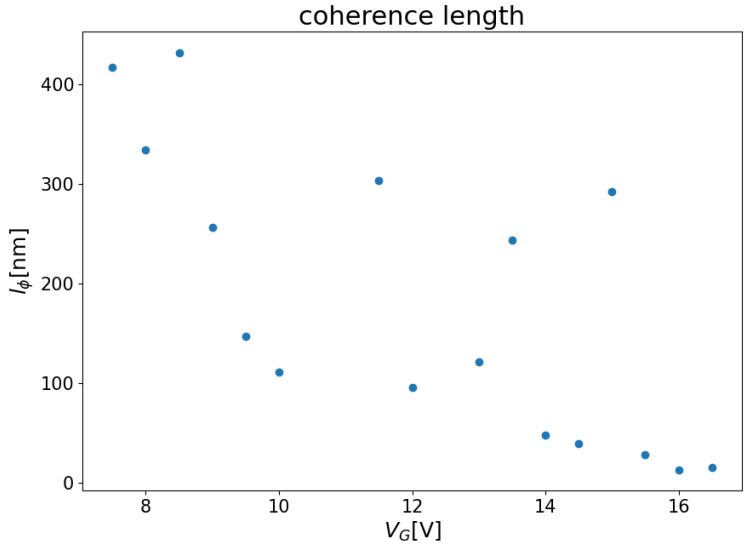

Figure 42: Coherence length as a function of back-gate voltage; device SC7 D4D4, T = 300 mK.

5.3 JOSEPHSON EFFECT

In this section we report the measurement of Josephson currents in recently fabricated superconducting weak links with Nb-only electrodes. Before this Master's thesis project, only a single Nb-only nanoflag-based device had been measured by our group (Ref. [80]): we decided to test the reproducibility of the performances of this new fabrication recipe, in order to compare them with those of previous designs based on Nb/Ti electrodes.
In order to analyse the Josephson effect, I-V curves were acquired in a 4-wires DC current bias setup. Soon it became clear that, in order to minimize the electrical noise in the system and, therefore, highlight its superconducting behaviour, it was convenient to connect the drain electrode of the junctions directly to the electrical ground of the system, thus avoiding to measure the drain current directly. Such current has been assumed to be equal to the nominal current bias $I_{bias} = \frac{V_{bias}}{R_{bias}}$. This assumption is justified by the fact that the used bias resistor $R_{bias} = 10\,M\Omega$ is far greater than any other resistance in the system, and it has been verified by performing preliminary drain current versus nominal current bias test measurements.
Here we report the characterization of device SGM1 D8D2, which, as described in the following chapter, has also been investigated by Scanning Gate Microscopy.
A current-voltage curve of said device is shown in Fig. 43, where we can identify two clearly defined regimes:

- a low-bias dissipationless regime, in the form of a zero-resistance plateau, corresponding to the flow of Josephson current across the junction;
- a high-bias dissipative regime, where the system displays an Ohmic behaviour, i.e., a linear voltage-current dependence, corresponding to a normal resistance R_N;

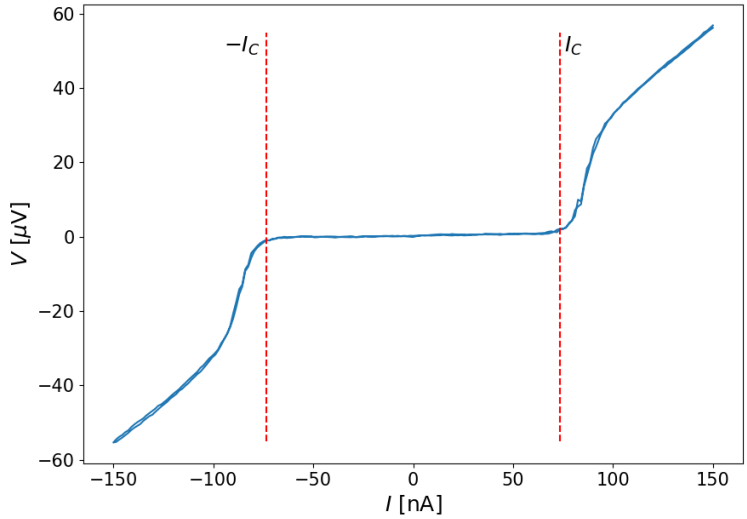

Figure 43: Current-Voltage curve of device SGM1 D8D2 at $V_G = 40\,V$. There is no clearly defined switching-retrapping difference: both forward and backwards sweeps are displayed in the plot, resulting to be perfectly overlapped.

- as expected, these two regimes are separated by a transient region corresponding to a rapid variation in the voltage difference across the junction. Such transition is smooth and takes place in a current bias interval rather than at a precise current bias value: we have defined the critical current I_C of the junction as the low-bias extreme of said transient interval, as indicated in Fig. 43.

The dissipationless-dissipative transition can be investigated by sweeping the current bias in two different ways:

- switching: the system is brought from the dissipationless to the dissipative regime; the current bias at which this process takes place goes under the name of switching current I_{sw};
- retrapping: the system is brought from the dissipative to the dissipationless regime; the current bias at which this process takes place goes under the name of retrapping current I_{rt};

In general, due to capacitive coupling between the junction's leads and heating of the system when in the dissipative regime [6], the switching and retrapping currents do not coincide, with the retrapping current being smaller than its switching counterpart, giving rise to an hysteretic behaviour of the junction at the superconducting transition that takes the name of switching-retrapping asymmetry.
In this case (Fig. 43), the system displays evident superconducting behaviour with smooth transitions and no switching-retrapping asymmetry, which is consistent with previous measurements in similar conditions [5, 123]. Said characteristics can be explained as the action of thermal fluctuations, which at 300 mK are strong enough to suppress phenomena that can be visible at lower temperatures [123].
Critical current has been determined as the minimal current bias value at which the

device	contact metal	L [nm]	W [nm]	I_C [nA] at $V_G = 40\,V$
SGM1 D8D1	Nb	180 ± 10	1530 ± 30	90 ± 10
SGM1 D8D2	Nb	130 ± 10	610 ± 10	80 ± 20
SGM3 H4D2	Nb	190 ± 10	1420 ± 30	35 ± 5
SGM3 H5D1	Nb	190 ± 10	1500 ± 30	700 ± 50
SC10 [5]	Nb/Ti	200	700	50
SC20 F6 [123]	Nb/Ti	250 ± 10	540 ± 10	50
SC20 F7 [123]	Nb/Ti	110 ± 10	530 ± 10	17

Table 2: Critical current of the superconducting devices measured at 300 mK by our reseach group. The first four rows correspond to original work made in this Master's thesis. Uncertanties are taken as the semidispersion of critical current data taken in different days. Novel Nb-only devices display in average better performances than the previous concept involving a 10 nm Ti sticking layer. A separate discussion will be reserved to device SGM3 H5D1.

potential difference across the junction is greater than a given threshold V_t; being the typical voltage noise in the zero resistance plateau of the order of fractions of μV independently of the device under study, such threshold has been chosen to be equal to $V_t = 2\ \mu V$. This results in a critical current of $I_C = 73\,nA$ at $V_G = 40\,V$.
We performed similar measurements on three other Nb-only devices (SGM1 D8D1, SGM3 H4 D2, and SGM3 H5D1) and compared the results with those obtained on Nb/Ti junctions in previous works of our research group (Table 2). Nb-only devices appear to display in average greater critical currents with respect to Nb/Ti ones, making this new recipe promising for the development of future nanoflag-based devices.

5.3.1 *Critical current modulation by the back-gate: JoFET*

In Fig. 44, a set of I-V curves taken at different back-gate voltages is displayed, showing that there is a dependence of the critical current and normal state resistance of the junction on the back-gate voltage. As the back-gate voltage is lowered, we expect the junction's normal resistance to increase and its critical current to decrease, which is what we observe as a general trend.
This can be better visualized in Fig. 45, showing the numerically computed differential resistance of the junction as a function of back-gate voltage and current bias. The picture shows that the Josephson effect is completely suppressed in the weak link when $V_G < 2.5\,V$, definitely ruling out the possibility of presence of a superconducting short in the system. Moreover, when $V_G > 14\,V$ no back-gate induced critical current modulation is present, in a similar way as in [5].
In the $2.5\,V < V_G < 14\,V$ interval, the critical current experiences an overall downward trend; however, there are evident fluctuations that ultimately lead to the presence of superconducting pockets in the $2.5\,V < V_G < 4\,V$ region. Such fluctuations are associated to features in the normal resistance of the sample, as shown in Fig. 46; this fact, alongside with the reproducibility of such features over measurements taken days apart from one another, could lead to the interpretation

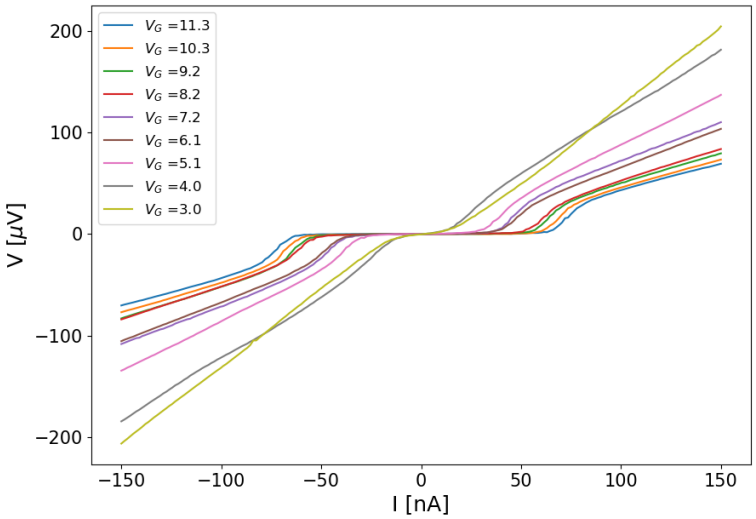

Figure 44: Current-Voltage curves of device SGM1 D8D2 at various back-gate voltages; there is no evident switching-retrapping difference;

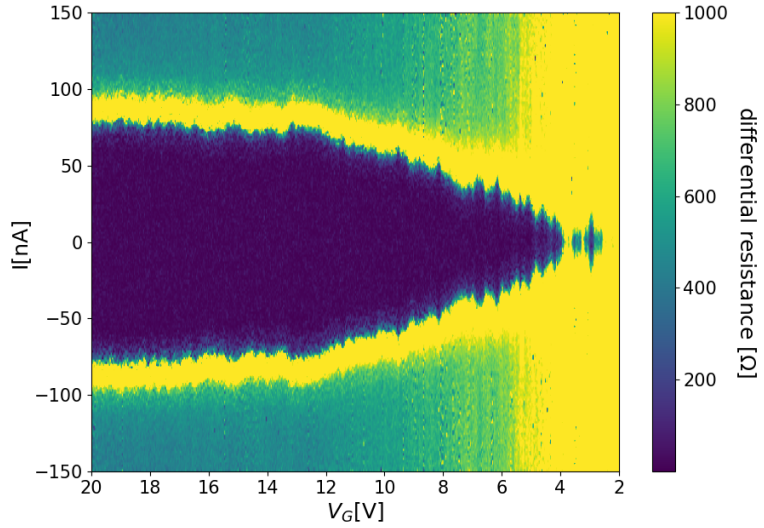

Figure 45: Differential resistance map as a function of the back-gate voltage and the current bias. Supercurrent is completely suppressed below $V_G = 2.5\,V$. Fluctuations in the critical current are present in the supercurrent modulation region ($2.5\,V < V_G < 14\,V$), ultimately resulting in superconducting pockets in the interval $2.5\,V < V_G < 4\,V$. Device SGM1 D8D2.

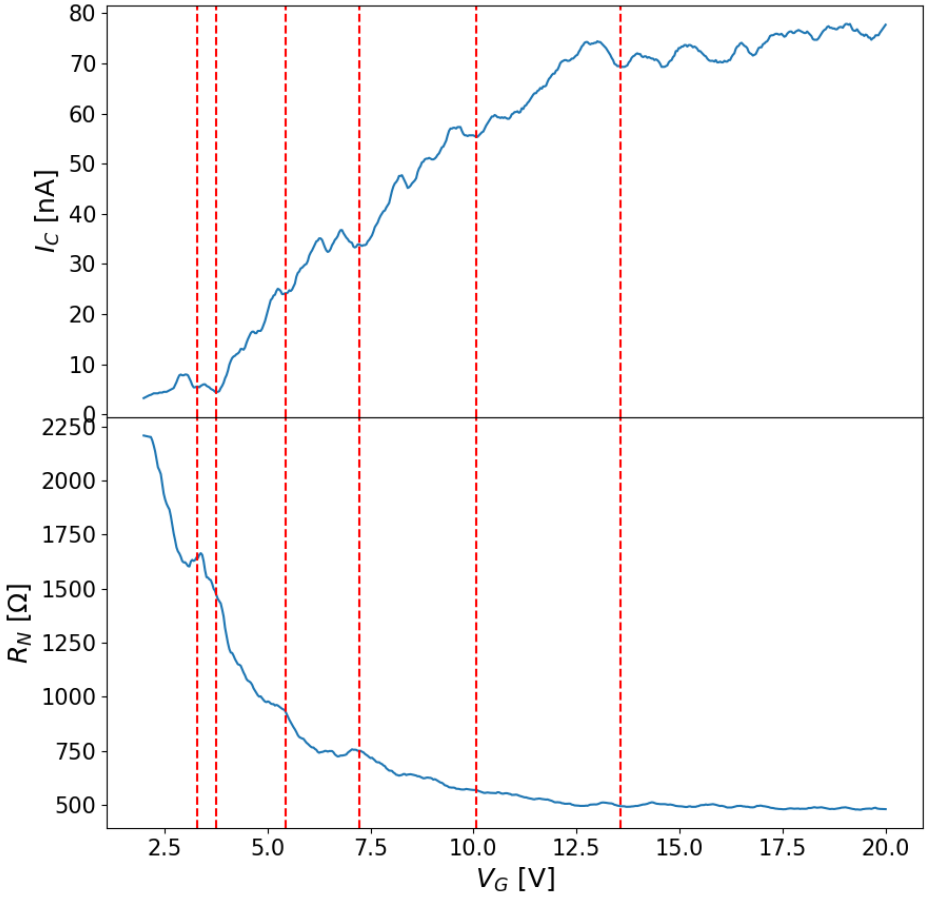

Figure 46: Top: critical current as a function of back-gate voltage; the signal has been filtered through a linear Savitzky-Golay filter with window equal to ten points. Red dashed lines indicate fluctuations in the critical current that have been found consistently over various back-gate modulation measurements; below: normal resistance as a function of back-gate voltage; the signal has been filtered through a linear Savitzky-Golay filter with window equal to ten points. Red dashed lines indicate features corresponding to those found in the critical current plot. Device SGM1 D8D2, T = 300 mK.

of this phenomenon as the superconductive equivalent of universal conductance fluctuations [24], but further investigation is needed.
It is worth to mention that this features are counter-productive when a sample is intended to be investigated by SGM: the back-gate operating point during SGM must be placed in a region where voltage-induced critical current modulation is possible (otherwise the effect of the tip would be negligible) and such modulation must be monotonous so that it can be determined univocally that when the tip operates in depletion mode the critical current in the junction is partially suppressed:[2] otherwise, it would be impossible to distinguish the amount of supercurrent that is blocked by the tip from the supercurrent enhancement or suppression due to tip-induced quantum interference effects.

5.4 FRAUNHOFER PATTERN

Superconducting quantum interference is another crucial feature of superconducting weak links. We measured I-V curves of device SGM1 D8D2 at several values of the magnetic field in a 4-wire DC current bias setup. Fig. 47 shows a plot of numerically computed differential resistance as a function of the current bias and magnetic field, which displays features typical of a Fraunhofer pattern: a main lobe and two first-order lateral side lobes.
We have extracted the magnetic field-dependent critical current with the same procedure described in Section 5.3.1. After that, we have performed numerical least squares fits on the critical current data using the Fraunhofer model [6]

$$I_C(B) = I_C(0)\left|\frac{\sin\left(\frac{\pi f S B}{\Phi_0}\right)}{\frac{\pi f S B}{\Phi_0}}\right|, \tag{67}$$

where $S = (L + 2\lambda)W$ is the area of the region penetrated by the magnetic field, $\lambda = 40\,\text{nm}$ is the Nb London penetration length [124], $\Phi_0 = \frac{h}{2e}$ is the superconducting flux quantum, and f is the so-called Magnetic Focusing factor, which takes into account the presence of the Meissner effect in the superconducting leads, which increases the entity of the magnetic field in the junction with respect to the externally applied field. f and $I_C(0)$ are taken as free parameters, to be determined by best fit: the results are reported in Fig. 47.
We notice that the best fit function describes well the central Fraunhofer lobe. However, the lateral lobes appear to be weaker than expected from the simple Fraunhofer picture: reduced lateral lobes are a common feature in InSb nanoflag-based Josephson junctions [5, 76, 123] that still has to be fully understood.
A possible explanation could be the following: the Fraunhofer model describes the behaviour of junctions in the $W \gg L$ limit, while more elaborate models take into account the effect of finite junction length. In particular, Heida et. al. [125] developed a model to describe the behaviour of ballistic junctions with $W \approx L$

$$I_C(B) = I_C(0)\left|\frac{\sin\left(\frac{\pi f S B}{2\Phi_0}\right)}{\frac{\pi f S B}{2\Phi_0}}\right|^2, \tag{68}$$

2 There has been no occasion of performing SGM with an externally applied magnetic field to the sample, therefore in this discussion I will analyse just the zero field case.

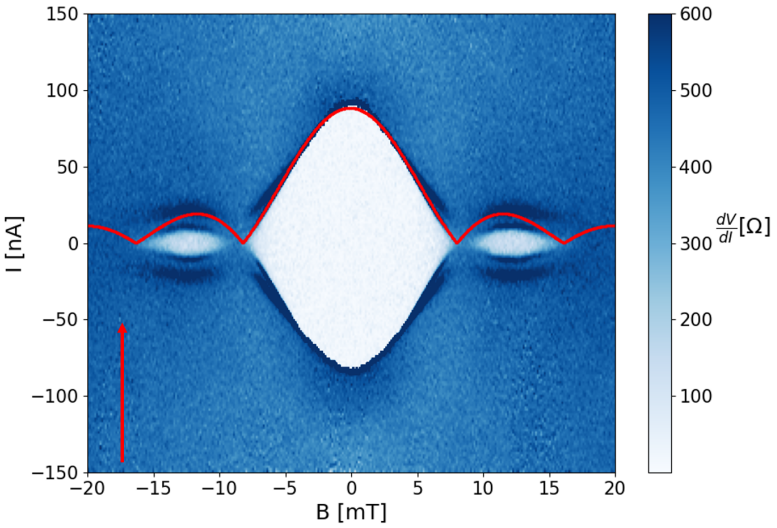

Figure 47: Numerically computed differential resistance as a function of current bias and magnetic field. Well defined lateral lobes are present; in red: best fit with the Fraunhofer model; red arrow indicates current sweep direction. Device SGM1 D8D2, $V_G = 40\,V$.

which predicts smaller side lobe amplitudes. Since for junction SGM1 D8D2 $L \approx \frac{W}{3}$, we performed a least squares fit of our data with this model, as well (reported in Fig. 48). The best fit describes rather well the central lobe, but completely fails to describe the behaviour of the side lobes, underestimating their amplitude and, differently from the fit with the Fraunhofer model, missing their locations.
In an attempt to better describe our data, we adopted the following heuristic approach: as we have already noticed, the fit with the Fraunhofer model is able to extract the correct periodicity of the lobes; for this reason, we heuristically implemented some corrections to this model in order to take into account the effects due to the finite width of the junction. To do so, we have developed the following model:

$$I_C(B) = I_C(0)\left(p_1\left|\frac{\sin\left(\frac{\pi f S B}{\Phi_0}\right)}{\frac{\pi f S B}{\Phi_0}}\right| + p_2\left|\frac{\sin\left(\frac{\pi f S B}{\Phi_0}\right)}{\frac{\pi f S B}{\Phi_0}}\right|^2\right), \tag{69}$$

which corresponds to a weighted average of a Fraunhofer-like contribution (with weight p_1) with a Heida-like contribution (with weight p_2) that is forced to display Fraunhofer-like periodicity. The best fit results are $p_1 = 0.497$ and $p_2 = 0.503$. The best fit curve is displayed in Fig. 49: this heuristic model describes in a precise way the shape, size, and periodicity of both the central and the lateral lobes. Therefore, size-related effects could play a role in determining the reduction of the lateral lobes, but further investigation in this direction is required to develop a more refined model to describe the behaviour of the system.
On the other hand, De Vries et al. [76] put forward the idea that this behaviour could be explained by a nonlocal transport process that creates a preferential supercurrent flow at the nanoflag lateral edges; this would result in an even-odd feature in the Fraunhofer pattern, i.e., in an enhancement of the even order lobes (like the central

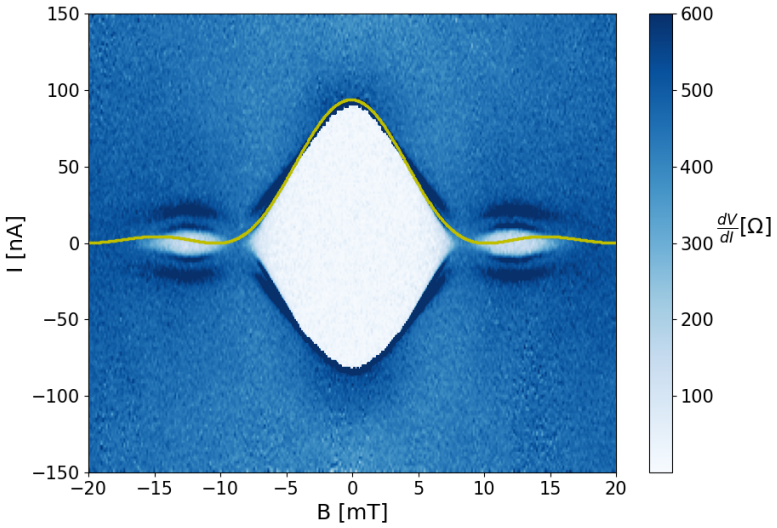

Figure 48: Numerically computed differential resistance as a function of current bias and magnetic field; in yellow: best fit with the Heida model; Device SGM1 D8D2, $V_G = 40\,V$.

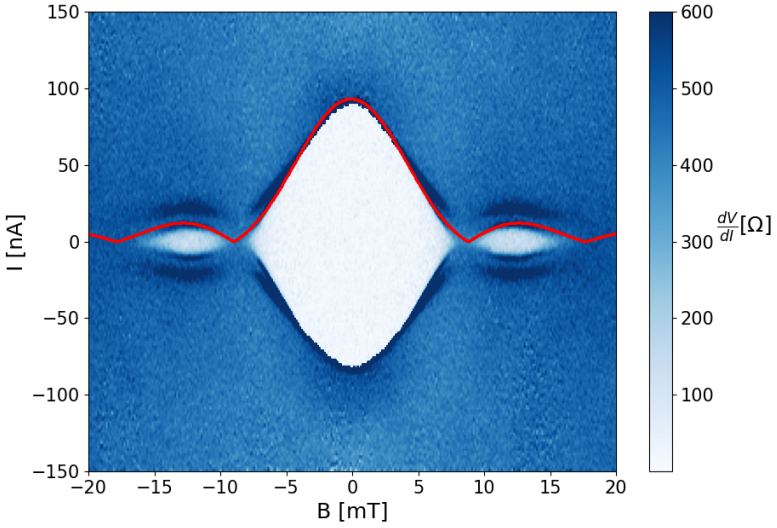

Figure 49: Numerically computed differential resistance as a function of current bias and magnetic field; in red: best fit with the model described in Eq. (69); Device SGM1 D8D2, $V_G = 40\,V$.

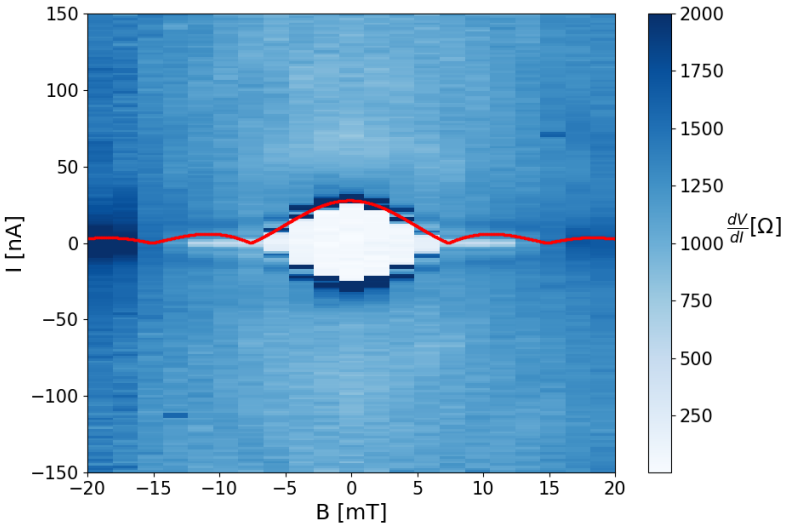

Figure 50: Differential resistance as a function of current bias and magnetic field. Hints of lateral lobes are present; in red: best fit with the Fraunhofer model. Device SGM1 D8D2, $V_G = 5.6\,V$.

V_G	$I_C(0)$ [nA]	f
40 V	87 ± 1	1.55 ± 0.02
20 V	73 ± 1	1.7 ± 0.2
16.6 V	74 ± 1	1.6 ± 0.2
12.8 V	63 ± 1	1.69 ± 0.2
9.2 V	50 ± 1	1.70 ± 0.2
5.6 V	28 ± 1	1.70 ± 0.2

Table 3: Least squares fit results of the Fraunhofer model; device SGM1 D8D2.

one) and a reduction of the odd order ones with respect to the Fraunhofer model. However, since in our devices so far there is no sign of the presence of visible second order lobes, which would be enhanced by this mechanism, there is no possibility to test such hypothesis.

We measured the dependence of the Fraunhofer pattern on the back gate voltage, reporting the results in Table 3: as expected, the zero-field critical current decreases with reduced back-gate voltage, while the measured values for the focusing factor are approximately constant and consistent with those reported in similar devices [5, 79].

Furthermore, we found that the presence of the lateral side lobes persists to back-gate voltages as low as $V_G = 5.6\,V$, see Fig. 50. This is promising in the future perspective of performing SGM (which necessitates back-gate voltage working points close to the pinch-off region) on supercurrents at finite magnetic fields.

Over the side lobes and the lateral region of the main Fraunhofer lobe an eye-like structure appears in the differential conductance plot (see Fig. 51); such feature appears in the I-V curves as a double-step in correspondence of the superconducting

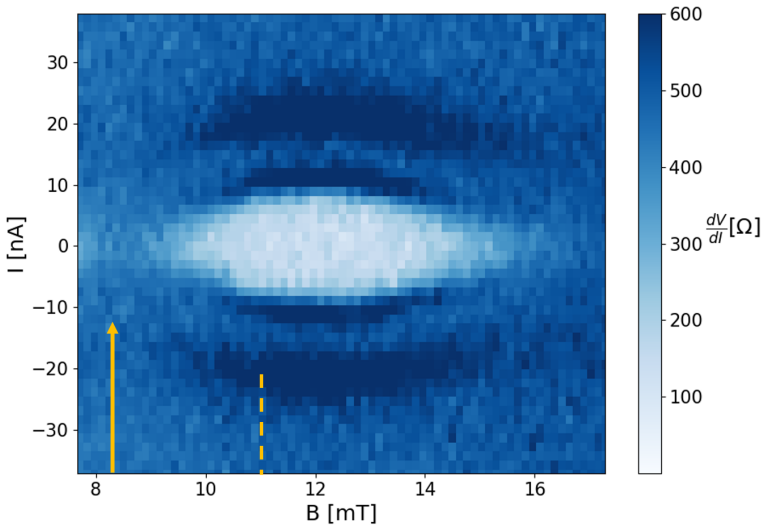

Figure 51: Zoom in of Fig. 47, highlighting the oscillations in the differential resistance close to the side lobes; yellow arrow indicates the current sweep direction; yellow dashed line indicates $B = 11\,mT$, e.g., the magnetic field value at which the cuts displayed in Fig. 52 and Fig. 53 have been extracted; device SGM1 D8D2, $V_G = 40\,V$.

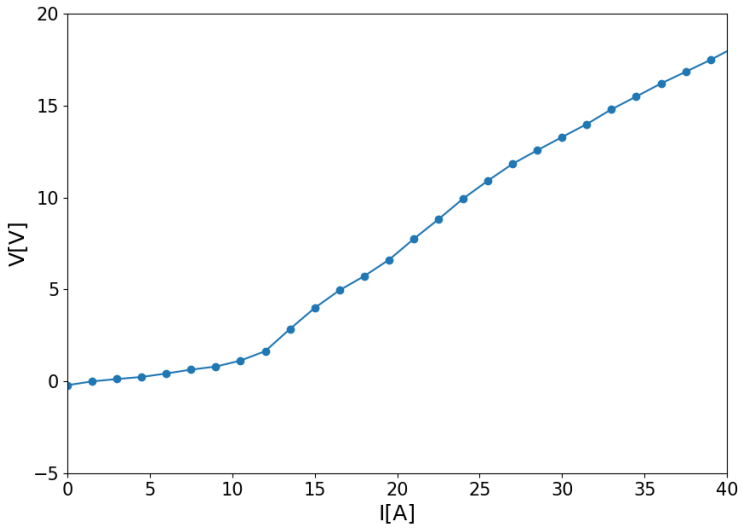

Figure 52: Section of the I-V curve taken at $B = 11\,mT$: the transition to the dissipative regime presents a double step feature. Device SGM1 D8D2, $V_G = 40\,V$.

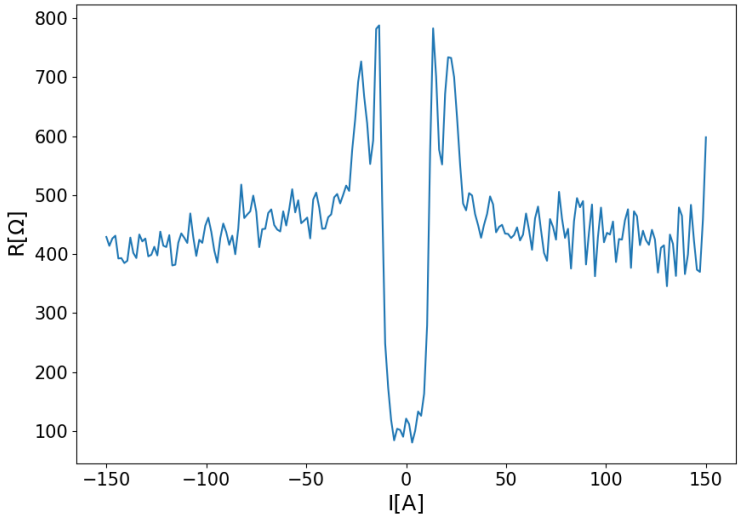

Figure 53: Numerical derivative of the I-V curve taken at $B = 11\,mT$: both positive and negative current transitions present a double differential resistance peak. Device SGM1 D8D2, $V_G = 40\,V$.

transition (Fig. 52) or as a double peak in the numerical differential resistance (Fig. 53). After repeating the measurement several times on the same junction within one week, the following conclusions were reached:

- such differential resistance oscillation features appear consistently over five measurements performed on device SGM1 D8D2;
- they appear both in switching and in retrapping: as shown in Fig. 51 the feature is symmetrical in the current bias (the negative bias transition corresponds to retrapping, while the positive bias one to switching);
- they never appear close to the maximum of the main Fraunhofer lobe, implying that this is an effect related to the presence of an external magnetic field.

To our knowledge, no similar features have been reported in literature and further investigation is needed to understand their nature.
To sum up, we have measured the superconducting quantum interference pattern of junction SGM1 D8D2; we observed the presence of fully developed first-order lateral side lobes, which remain visible even when the junction is close to pinch off, opening up the possibility of performing tip-induced supercurrent manipulation at finite magnetic fields; furthermore, we observed a reduction in the amplitude of the lateral lobes with respect to the expectations based on the Fraunhofer model, as well as unexpected oscillations in the differential conductance at finite magnetic fields, which require further investigations to be fully understood.

In the attempt to observe devices displaying higher critical currents and multiple lateral Fraunhofer lobes, we opted to fabricate wider junctions. In order to do this, Dr. Gaurav Shukla experimented the possibility of depositing Nb electrodes oriented along the <1-21> crystalline direction of the flag [77] instead of the previously used <111> direction [5, 79, 80] (see Fig. 54).
Three devices of this kind were tested: SGM1 D8D1, SGM3 H4D2, and SGM3 H5D1. The first two devices delivered performance not different from those of their <111> counterparts, but SGM3 H5D1 behaved very differently.
Device SGM3 H5D1 displays the highest critical current recorded in our lab at $T = 300\,mK$, surpassing the closest competitor by an order of magnitude.
Consistently reproducing such unexpected and currently unexplained performance would pave the way for the development of future InSb nanoflags-based devices.

5.5.1 *Josephson effect*

A typical I-V curve of device SGM3 H5D1 is reported in Fig. 55; it displays features that are here observed for the first time at 300 mK in InSb-based devices:

- transitions between the dissipationless and dissipative regime are extremely sharp, differently from Fig. 43;
- the typical switching current is about $I_{sw} \approx 700\,nA$;
- there is an evident switching-retrapping asymmetry, with the retrapping current being about $I_{rt} \approx 400\,nA$

The switching-retrapping asymmetry can be understood in the RCJ model framework in presence of small thermal fluctuations [6] and is due to the interplay between Josephson effect and the junction's spurious capacitive and resistive behaviour. Such feature is suppressed in presence of non-negligible thermal fluctuations in the system, which can be estimated with the thermal current noise at $\delta I_{300\,mK} = \frac{2ek_BT}{\hbar} = 12.5\,nA$. Such current fluctuations are about the same order of

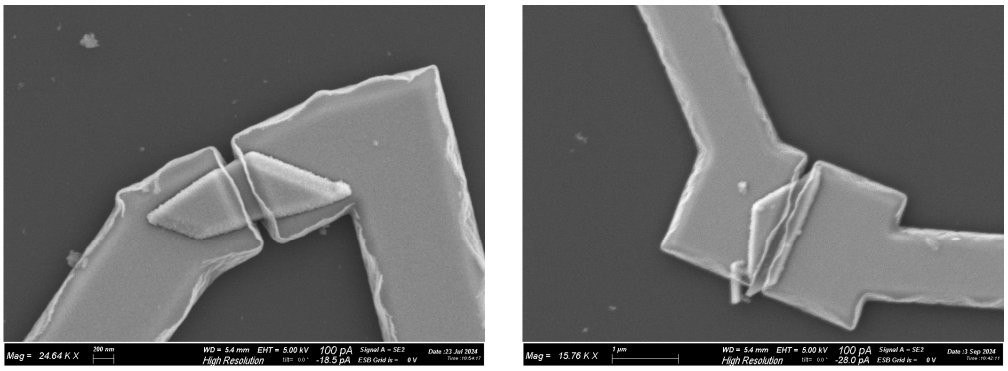

Figure 54: On the left: SEM image of device SGM1 D8D2, oriented along the <111> crystalline direction of the InSb nanoflag; on the right: SEM image of device SGM1 H5D1, oriented along the <1-21> crystalline direction.

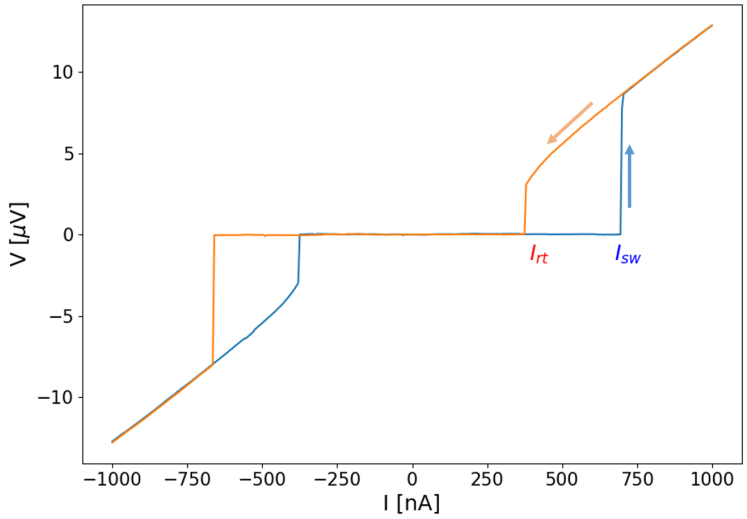

Figure 55: I-V curve of device SGM3 H5D1 at $V_G = 40\,V$; in orange: descending current bias curve; in blue: ascending current bias curve. Superconductive transitions are much sharper than those shown in Fig. 43 and display evident switching-retrapping asymmetry.

magnitude as the critical currents recorded in the other devices, but are a factor 60 smaller than the SGM3 H5D1 switching current at $V_G = 40\,V$, which justifies our observations.

Back-gate modulation of the superconducting characteristics are reported in Fig. 56, showing complete suppression of supercurrent flow across the junction at voltages below $V_G < 5\,V$ and therefore demonstrating the correct functioning of the device as a JoFET and excluding the possibility of attributing its behaviour to the presence of a Nb microbridge shorting the junction.

5.5.2 *Multiple Andreev reflections*

This exceptional critical current might be due to an higher than usual Nb-InSb interface transparency in device SGM3 H5D1.

In order to put this idea to test, we measured Multiple Andreev Reflections features in a 4-wire AC+DC current bias setup described in Section 4.4.4 [3]. As mentioned in Section 2.3.6, the differential conductance of a highly transparent weak link displays an oscillating behaviour with minima located at voltage differences across the junction equal to $V_n = \frac{2\Delta^\star}{ne}$, where $\Delta^\star$ is the induced superconducting gap in the nanoflag and n is a natural number.

Fig. 57 reports a differential conductance measurement as a function of the DC voltage difference across the junction at $V_G = 40\,V$. The plot clearly presents well-resolved signatures of a subharmonic gap structure in the form of differential conductance oscillations.

Fig. 58 reports differential conductance measurements at different values of the

3 $R_{biasAC} = 10\,M\Omega$, $R_{biasDC} = 100\,k\Omega$, $V_{biasAC} = 0.1\,V$

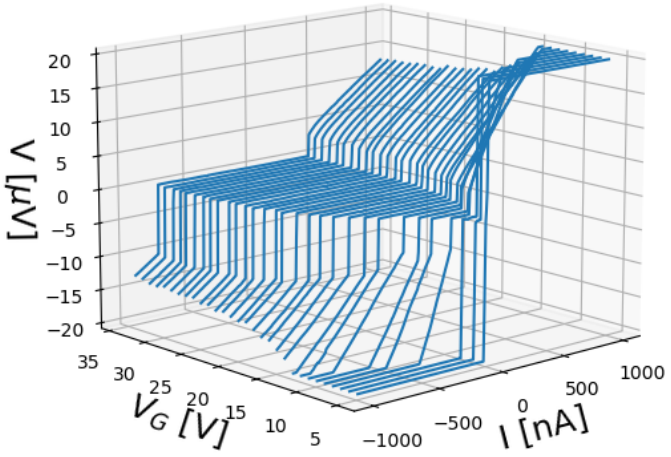

Figure 56: back-gate-induced critical current modulation: supercurrent flow is completely supressed below $V_G = 5\,V$; device SGM3 H5D1.

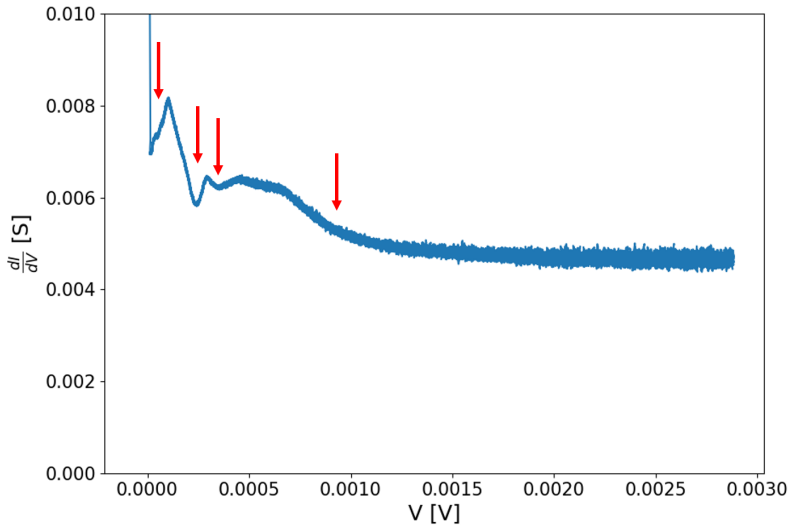

Figure 57: Subharmonic gap structure in the differential conductance signal as a function of the voltage difference across the junction; red arrows indicate dips and flexions in the differential conductance; device SGM3 H5D1, $V_G = 40\,V$.

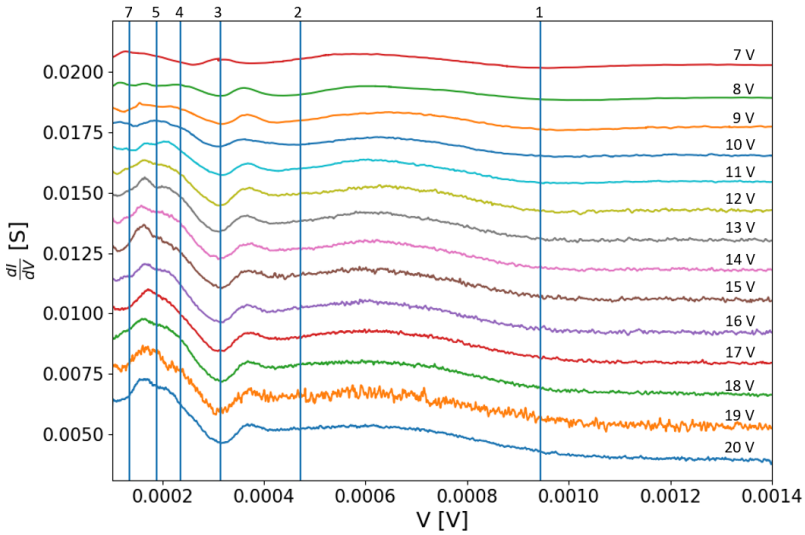

Figure 58: MAR traces at various back-gate voltages: the offset between consecutive measurements is set to 1.5 mS in order to better visualise the different curves; vertical lines correspond to the expected positions of differential conductance minima based on the location of the best resolved conductance dip, recognized as $\frac{2\Delta^\star}{3e}$; from left to right: $\frac{2\Delta^\star}{7e}$, $\frac{2\Delta^\star}{5e}$, $\frac{2\Delta^\star}{4e}$, $\frac{2\Delta^\star}{3e}$, $\frac{2\Delta^\star}{2e}$ and $\frac{2\Delta^\star}{e}$, with $\Delta^\star = 0.47$ meV; device SGM3 H5D1.

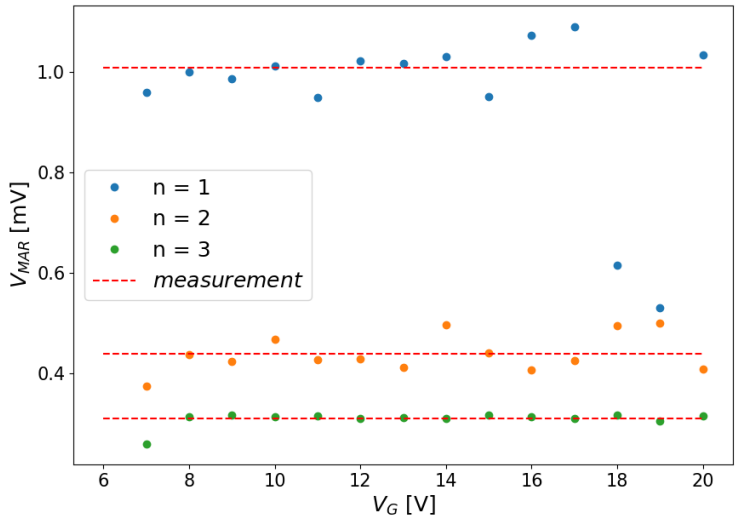

Figure 59: Positions of the local conductance minima corresponding to $\frac{2\Delta^\star}{3e}$, $\frac{2\Delta^\star}{2e}$ and $\frac{2\Delta^\star}{e}$ features; horizontal red lines correspond to the average position of the dip across the analysed back-gate voltage range. Device SGM3 H5D1.

n	$\Delta^\star$ [μeV]
1	500 ± 20
2	440 ± 40
3	460 ± 20

Table 4: Induced superconducting gap $\Delta^\star$ extracted from the average of the positions of minima of the differential conductance at different back-gate voltages. Error bars coincide with the standard deviation of the collected data. Device SGM3 H5D1.

back-gate voltage, displaying the following behaviour: while the amplitude of the differential conductance oscillations tends to fade as the back-gate voltage gets reduced, the positions of said features experience little to no change until $V_G = 8\,V$, indicating that the back gate voltage has no influence on the value of the proximity induced superconducting gap. A first change in the dip positions seems to appear at $V_G = 7\,V$, but investigation at lower gating voltages was prevented by the presence of noise due to the junction being close to pinch-off.

The best resolved feature in the differential conductance curves is a dip that has been recognized, by qualitative comparison with theoretical simulations reported in Fig. 9, as that corresponding to $V_3 = \frac{2\Delta^\star}{3e}$. The position of said dip has been taken as a reference to determine the position of more elusive features. In fact, we extracted from it an initial estimation of the proximity-induced superconducting gap $\Delta^\star = 0.47\,meV$. Consistent with our assignment, the positions of the vertical lines reported in Fig. 58, corresponding to the expected positions of differential conductance features based on this initial estimation, are placed close to actual conductance dips or flexions for values of $n = 1, 2, 3, 4, 5, 7$.

The position of the conductance dips corresponding to $V_{1,2,3}$ have been measured as that of the local minimum of the signal[4] placed closest to the expected value corresponding to our first rough estimation of the induced superconducting gap. No clear dip in the $V_1 = \frac{2\Delta^\star}{e}$ position is present at voltages above $V_G > 17\,V$, while a well-developed feature is found at lower back-gate voltages. The results are reported in Fig. 59 and in Table 4.

As shown in Table 4, the extracted values of the induced superconducting gap are compatible with one another and with the initial estimation, resulting in a weighted average of $\Delta^\star = 0.47\,meV$. By applying Eq. (34) (which links the induced gap to the gap in the proximitizing material), given the Nb superconducting gap $\Delta = 1.28\,meV$ and critical temperature $T_C = 8.44\,K$ measured in similar NEST-fabricated devices [5], a Cooper pair breaking parameter $\gamma_B = 3.4$ is obtained (see Section 2.3.5), a factor 3 lower than that reported in similar devices [5], indicating a high Nb-InSb interface transparency.

Another way to estimate junction transparency is the product between excess current and normal resistance, displayed in Fig. 60. Such product presents little to no back-gate modulations when $V_G > 12\,V$ and tends to decrease at lower back-gate voltages. The coefficient $\alpha = \frac{eR_N I_E}{\Delta^\star}$ is a well established figure of merit of superconducting weak links whose ideal theoretical value is $\frac{8}{3}$; in this case a value of $\alpha \approx 0.87$ is measured, compatible to that observed in the past in similar

4 Local minima have been determined using the *argrelextrema* function from the *scipy* python library.

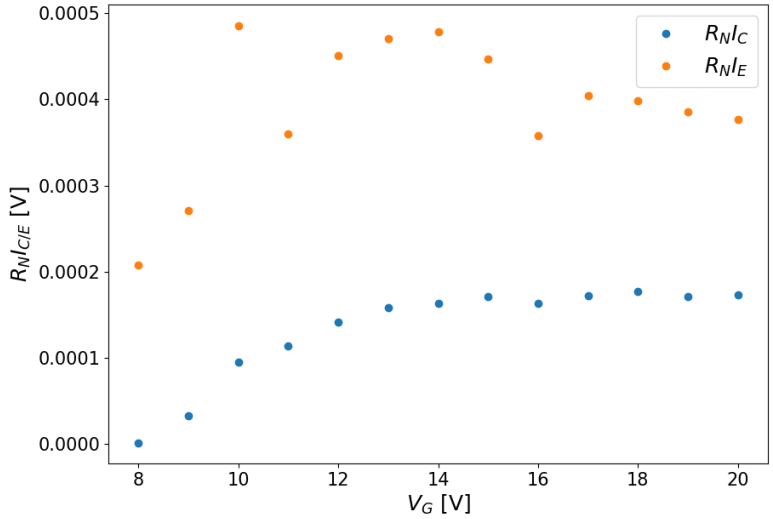

Figure 60: product of the critical/excess current times the normal resistance as a function of the back-gate voltage; device SGM3 H5D1.

structures [5].
In a similar fashion, the product between the switching current and the normal resistance is supposed to be equal to $\frac{\Delta^\star}{e}$ up to a constant of the order of unity; here $\frac{eI_C R_N}{\Delta^\star} \approx 0.2$, which is a manifestation of premature switching in weak links induced by thermal fluctuations [5, 6].
Furthermore, the device behaviour was studied as a function of temperature. In Fig. 61 we report the values of switching current as a function of the device temperature.
Supercurrent flow across the device is completely suppressed at temperatures above $T > 2.5\,K$, corresponding to thermal current fluctuations of $\delta I_{2.5\,K} > 100\,nA$ (same order of magnitude as the switching current) and a thermal energy of $k_b T > 0.2\,meV$ (same order of magnitude as the InSb induced superconducting gap).
On the other hand, Eq. (34), that we repeat here

$$\Delta^\star(T) = \frac{\Delta(T)}{1 + \frac{\gamma_B}{\pi T_C}\sqrt{\Delta^2(T) - \Delta^{\star 2}(T)}}, \tag{70}$$

states that the proximity induced superconducting gap depends only on the value of the gap of the proximitising material, in this case Nb. In the $0\,K < T < 4\,K$ range the Nb superconducting gap experiences negligible variations and, therefore, the proximity-induced gap should remain constant even when its value is comparable to the thermal fluctuations in the system. To test this hypothesis, differential conductance curves have been acquired as a function of temperature and are reported in Fig. 62. For the determination of conductance minima, the same procedure described for the back-gate dependent measurements has been applied; in these measurements the only dip-like feature that can be clearly resolved from the background noise is that corresponding to V_3.
Fig. 63 shows that the position of such differential conductance feature experiences little to no variations with temperature, and the amplitude of the observed oscilla-

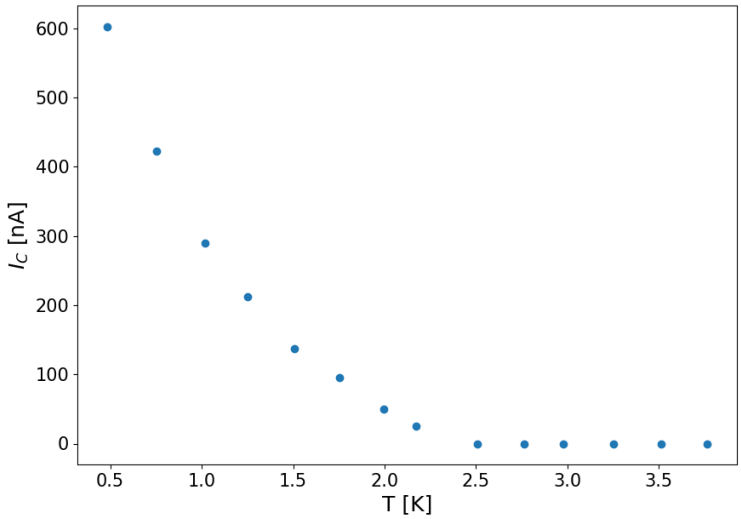

Figure 61: Critical current dependence on the temperature of the system: supercurrent flow across the device is completely suppressed above $T = 2.5\,K$; $V_G = 40\,V$; device SGM3 H5D1.

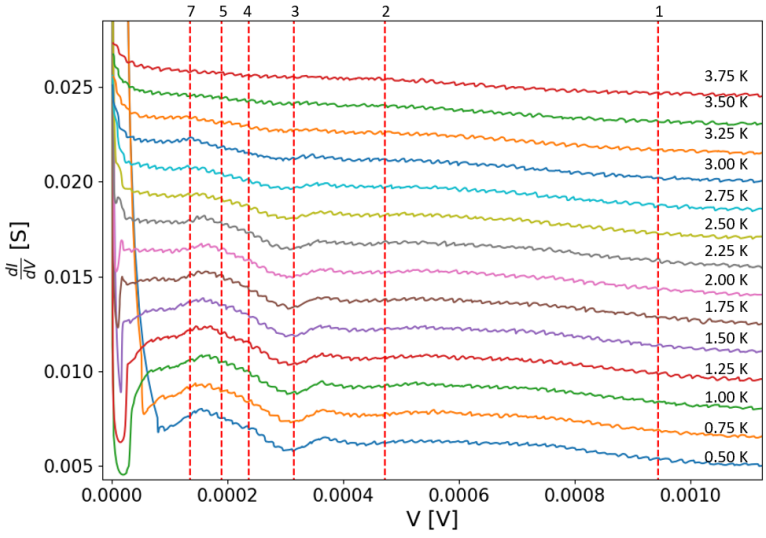

Figure 62: MAR traces at various temperatures: offset between consecutive measurements is set to 1.5 mS in order to better visualise the different curves; vertical lines correspond to the expected positions of differential conductance minima based on the location of the best resolved conductance dip, recognized as $\frac{2\Delta^\star}{3e}$; from left to right: $\frac{2\Delta^\star}{7e}$, $\frac{2\Delta^\star}{5e}$, $\frac{2\Delta^\star}{4e}$, $\frac{2\Delta^\star}{3e}$, $\frac{2\Delta^\star}{2e}$ and $\frac{2\Delta^\star}{e}$, with $\Delta^\star = 0.47\,meV$; device SGM3 H5D1, $V_G = 40\,V$.

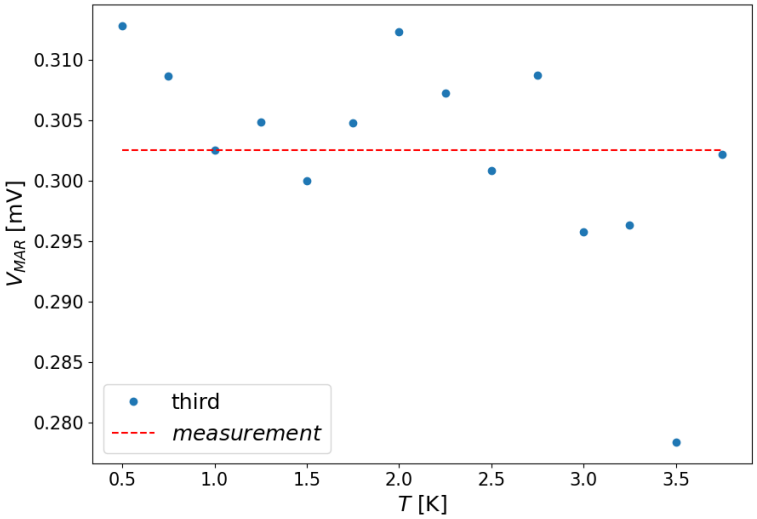

Figure 63: Position of the local conductance minima corresponding to $\frac{2\Delta^*}{3e}$ features; the horizontal red line corresponds to the average position of the dip across the analysed back-gate voltage range. Device SGM3 H5D1, $V_G = 40\,V$.

tions fades away at high temperatures, but remains visible even at temperatures where supercurrent flow is suppressed in the weak link, confirming that a finite proximity-induced gap is still present in the region below the leads.

5.5.3 *Fraunhofer pattern*

Finally, we report the magnetic superconducting interference patterns measured on device SGM3 H5D1. Fig. 64 shows two sets of numerically computed differential resistance data as a function of the current bias and the externally applied magnetic field, for the magnetic field swept from negative to positive values and vice versa. Both plots present side lobes alongside sudden jumps in the differential resistance between consecutive external magnetic field values.
After having repeated these measurements multiple times, we noticed that the presence of these jumps persists, but their location varies randomly from sweep to sweep.
Furthermore, in each measurement, the pattern seems to be shifted towards the sweep direction. The same results were obtained in the study of device SGM1 D8D1, while nothing of this sort has been reported on junctions fabricated along the <111> crystalline direction. This excludes a magnetization of the cryostat as the reason for these jumps, which instead must be sample related.
We propose this is due to the action of Abrikosov vortices in the region of the Nb leads close to the junction; a solution would be changing the geometry of the Nb leads to the nanoflag from rectangular to T-shaped, so as to reduce their surface, a precaution that is about to be taken in the fabrication of any future <1-21> oriented InSb nanoflag based junctions from now onward.

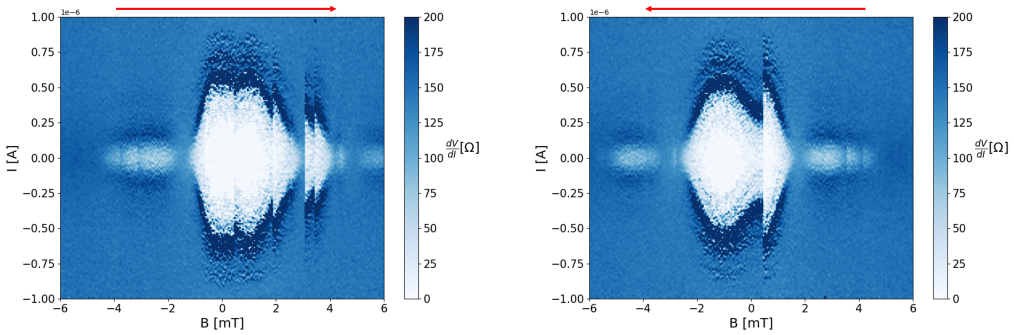

Figure 64: Magnetic superconducting interference pattern; right: descending magnetic field; left: ascending magnetic field. the red arrows indicate the sweep direction. Device SGM3 H5D1, $V_G = 40\,V$.

6

SCANNING GATE MICROSCOPY ON INSB NANOFLAG-BASED JOSEPHSON JUNCTIONS

In this chapter we describe the steps leading to the first SGM critical current maps performed on superconducting weak links.

6.1 ATOMIC FORCE MICROSCOPY

One of the most crucial prerequisites in order to perform a scanning gate experiment is being able to locate the region of interest, which requires the ability of performing both room temperature and low temperature AFM topography maps without damaging either the devices or the tip. During this process, InSb nanoflags are kept in place by van der Waals interactions with the silica substrate and by the presence of the metallic leads, which makes the system extremely frail: careful optimization of the feedback parameters is needed in order to prevent the tip from mechanically dragging away the nanoflags.
Such fine tuning procedure can be performed prior to any topography map with the help of the Setpoint Modulation feature of the Daisy microscope controller software, which allows to periodically change the feedback setpoint between two values in a square wave fashion, simulating a sudden change in the sample topography.
By monitoring the feedback signal, the P and I parameters can be adjusted in order to reach a situation where the microscope shows both a quick reaction time to sudden changes and limited fluctuations around the setpoint.
Another important parameter is the setpoint itself, which determines the tip-to-sample distance during the measurement. A good compromise has been found by setting the feedback setpoint at 900 mV while selecting an excitation signal that keeps the free oscillation resonance amplitude of the tuning fork in the $1.05\,\mathrm{V} - 1.2\,\mathrm{V}$ range at low temperature and in the $1.00\,\mathrm{V} - 1.05\,\mathrm{V}$ range at room temperature. In ideal tip conditions, this optimization process allows to obtain a sub-100 nm spatial

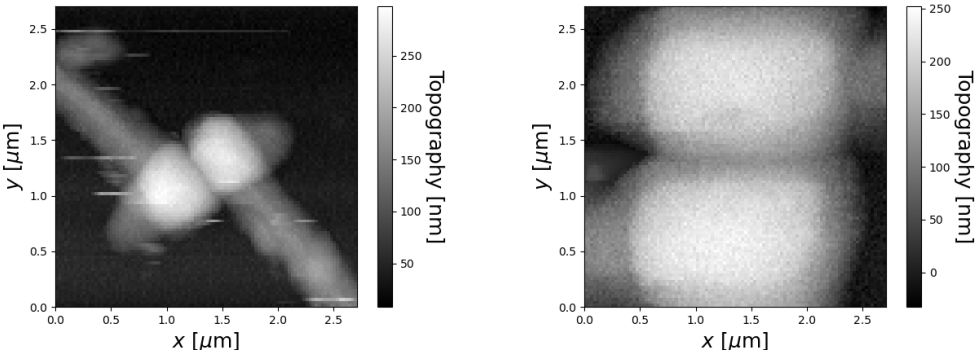

Figure 65: Room temperature AFM performed with a sharp tip with sub-100 nm spatial resolution.

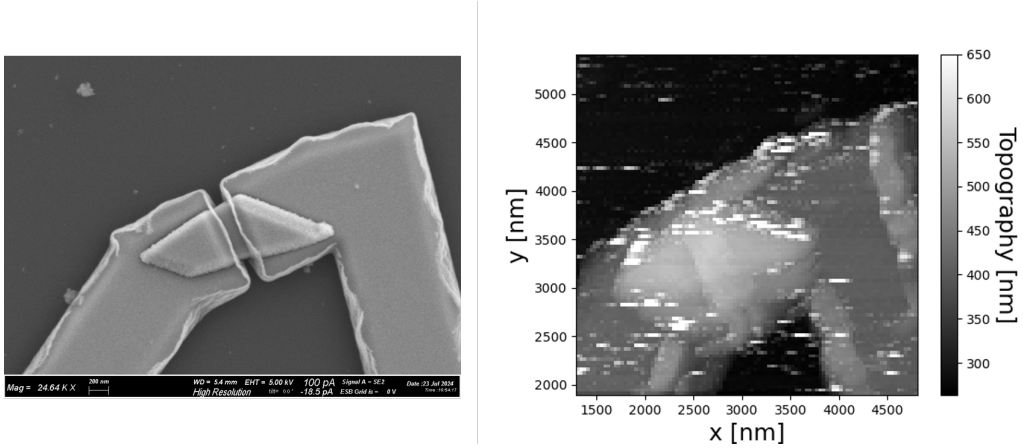

Figure 66: On the left: SEM image of device SGM1 D8D2; on the right: low temperature AFM image of the same device, in which both the nanoflag and the junction shape can be clearly identified.

resolution at room temperature, as displayed in Fig. 65, where the metallic leads, the InSb nanoflag, and the junction region are clearly identifiable.
The best resolved low temperature topography map of a superconductive device is reported in Fig. 66. Here both the junction and the nanoflag can be clearly identified, but it displays lower resolution due to the system's higher susceptibility to noise at low temperature.
In any case both low temperature and room temperature AFM maps possess sufficient resolution to clearly identify the region of interest over which SGM will be performed.

6.2 SCANNING GATE MICROSCOPY AT 77 K

Before cooling the system to 300 mK, the correct functionality of the electrical connections to the tip has been tested by performing conventional normal state SGM at 77 K.
In this section we report the first SGM measurements on InSb nanoflag-based samples, displayed in Fig. 67. This test was made on device SC6, which consists in a nanoflag contacted with 4 Nb-Ti electrodes. SGM measurements were performed in dual pass mode and in 2-wire[1] 100 nA AC current bias setup acquiring the in phase component of the voltage difference signal across the junction with an integration time of 300 ms.
In order to enhance the effect of the tip, a back-gate potential working point of $V_G = 3\,V$ has been set, corresponding to a region where the rate of change of the sample conductance with the back-gate voltage is maximized, as shown in Fig. 68.
In Fig. 67 we report a conductance modulation map induced by a $V_{tip} = 10\,V$ polarized tip; data have been filtered with a Gaussian filter with $\sigma = 2$ pixels in order to eliminate random background fluctuations in the electrical signal.
The location of an exposed region of the nanoflag is marked by a red area in the conductance map: as expected, once the positively charged tip gets close to the

1 The Nb stripes leading to electrodes 3 and 4 were severed.

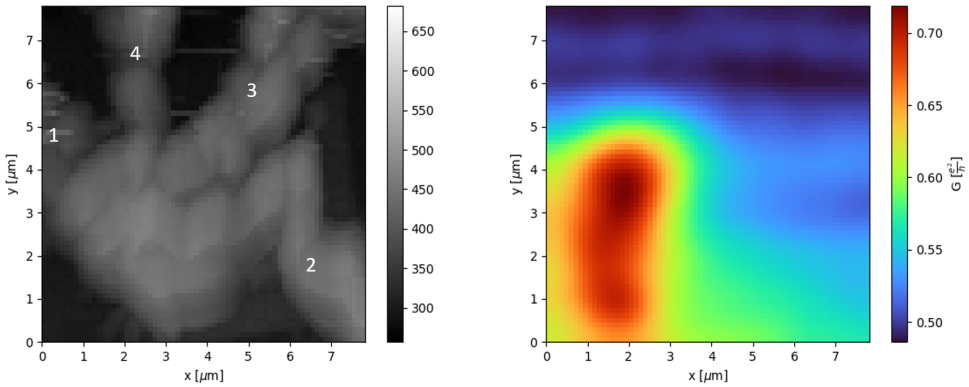

Figure 67: Left: topography of device SC6; right: conductance map as a function of the tip position acquired in dual pass mode with a 200 nm tip offset with respect to the topography scan. Working point: $V_{tip} = 10\,V$, $V_{BG} = 3\,V$.

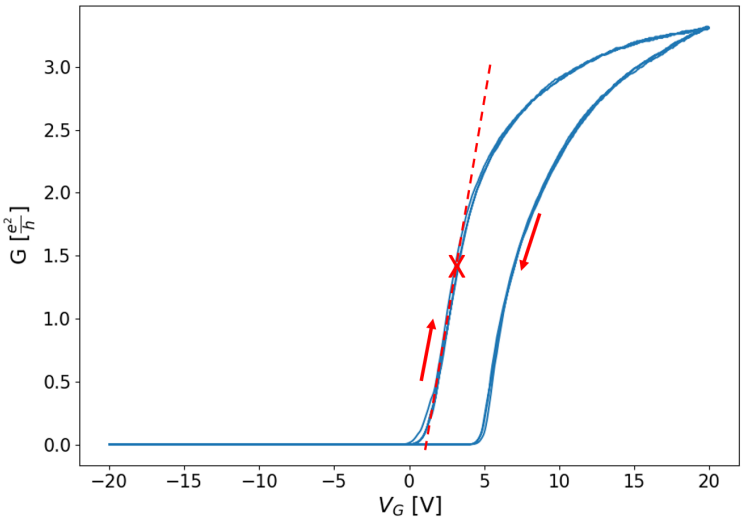

Figure 68: Back-gate conductance modulation curve of device SC6. The back-gate working point $V_G = 3\,V$ is indicated by a red x. The numerical least squares fit of the rising slope in proximity to the working point with a linear model is indicated by the red dashed line. The fit results in a back-gate efficiency $\alpha_G = 0.52\,\frac{e^2}{hV}$.

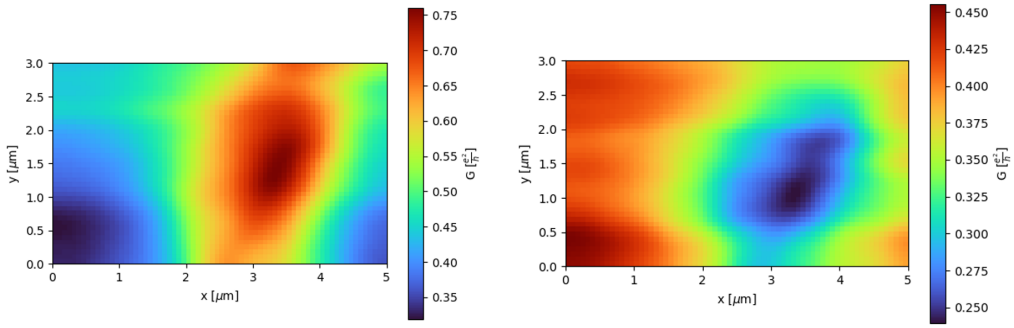

Figure 69: Left: conductance map as a function of tip position acquired in dual pass mode with a 60 nm tip offset with respect to the topography scan. Working point: $V_{tip} = 10\,V$, $V_{BG} = 3\,V$; right: conductance map acquired in the same conditions, but with $V_{tip} = -10\,V$.

device it induces charge carrier accumulation in the InSb nanoflag enhancing its conductance.
In order to recognize this effect as caused by the tip-induced charge carrier density modulation, SGM maps have been acquired with both positive and negative voltages applied to the tip, as reported in Fig. 69.
As expected, while the positive polarization of the tip induces a conductance enhancement, the negative polarization induces a conductance suppression once the tip is placed close to the exposed semiconducting region.
We noticed that in both Fig. 67 and Fig. 69 the junction conductance data recorded in the SGM scans is smaller than that corresponding to the working point in Fig. 68; we attribute this effect to a shift in the position of the conductance modulation curve caused by the presence of the tip close to the device. Nevertheless, the presence of this effect has not affected our analysis nor our interpretation of the data, since it appears to affect all of the measurements in the same way.
The effect of the tip was next studied as a function of the tip-to-sample voltage difference V_{tip} by performing dual pass scans with a lift-off of 60 nm with respect to the reference topography. For each SGM scan, the maximum recorded conductance is taken and displayed in Fig. 70; uncertainties are set to be equal to the fluctuations in the conductance signal when the tip is in proximity to the device.
The acquired data are well described by a linear model

$$G_{max} = \alpha_{tip} V_{tip} + G_0, \tag{71}$$

which has been used to perform a numerical least squares fitting procedure, leading to the following results

$$\alpha_{tip} = 0.047 \pm 0.008 \, \frac{e^2}{hV} \tag{72}$$

$$G_0 = 0.28 \pm 0.06 \, \frac{e^2}{h} \tag{73}$$

The parameter G_0 corresponds to the background signal that is obtained when the tip is placed far away from the device. The value obtained from the fit is consistent

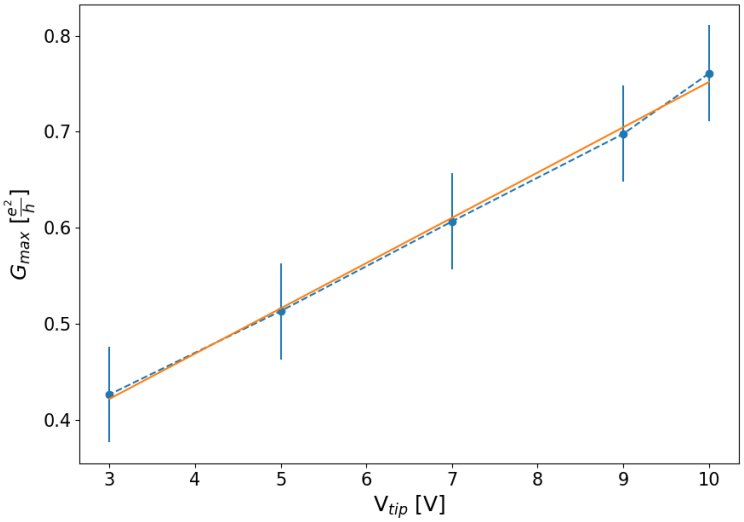

Figure 70: Maximum conductance recorded in an SGM map as a function of the tip-to-sample voltage difference. A numerical least squares fit has been performed using a linear model.

with those measured in the conductance maps. From the slope α_{tip} it is possible to estimate the efficiency of the tip-nanoflag capacitive coupling with respect to the tip-back-gate coupling: from the back-gate conductance modulation curve (Fig. 68) we determined that the conductance as a function of the back-gate voltage in proximity to the working point follows a linear model with slope $\alpha_G = 0.52 \pm 0.05 \frac{e^2}{hV}$.
Being the device close to pinch off, the contribution of the InSb channel to the sample resistance is way larger than the contact resistance, which can therefore be neglected. This allows to assume the charge carrier density proportional to the sample conductance.
Then, we can obtain the ratio between the tip and back-gate gating efficiencies as

$$\frac{\alpha_{tip}}{\alpha_G} \approx 0.09 \pm 0.02 \tag{74}$$

This indicates that, when placed at 60 nm distance from the sample, the effect of 10 V on the tip is equivalent to a variation of the back-gate potential of about 1 V; however, since capacitive coupling depends on the sample and tip geometry and on the sample-to-tip distance, this measurement has to be taken as a rough estimation and stronger or weaker capacitive couplings are to be expected depending on the specific situation.
One of the main difficulties found in performing SGM measurements was related to the strong susceptibility of the system to electric perturbations: due to material pickup by the tip, both the quality of topography pictures and the response time of the feedback loop got worse over time, leading to the charged tip occasionally getting into contact with one of the Nb leads. This electrical spike can change the electrostatics of the nanoflag, shifting its back-gate threshold voltage and therefore the position of the chosen working point on the conductance back-gate modulation curve. In the worst case, the discharge is sufficient to destroy the device.

For these reasons, device SC6 has been used as a benchmark to find the optimal tip-to-sample distance that allows safe operation while maintaining a satisfying SGM spatial resolution. We came to the conclusion that 100 nm is the optimal safety distance in our operative conditions.

6.3 NORMAL-STATE SCANNING GATE MICROSCOPY AT 300 mK

Here we report the first SGM maps of an InSb nanoflag-based device at 300 mK. The device in question is SC7 D4D4 and consists in an InSb nanoflag contacted with three Nb/Ti electrodes as displayed in the AFM topography map and the SEM image reported in Fig. 71.
SGM measurements were performed in dual pass mode with 100 nm lift-off with respect to the reference topography; electrical transport data were acquired in a 2-wire[2] 100 nA DC current bias setup by simultaneously recording both the drain current and the voltage difference across the junction. All SGM maps have been acquired with $V_{tip} = -10\,V$.
This junction did not support any supercurrent flow, but displayed an unexpected behaviour, as shown in Fig. 72.
This figure includes 100 pixel x 100 pixel plots of the variation in the junction's resistance as a function of the position of the polarized tip at different back-gate voltages. Prior to being plotted, SGM data were processed via the following pipeline:

1. row-wise subtraction of the row-averaged resistance value: this is a common technique in treating Scanning Probe data when there can be row-to-row signal jumps due to different rows not being acquired immediately after one another. This is our case, since dual pass mode is based on the alternation of the acquisition of topography and SGM lines (as described in Section 4.4.4);
2. median filter with $\sigma = 3$ pixels, in order to remove any signal noise spikes;
3. Gaussian filter with $\sigma = 1.5$ pixels, aiming at smoothing out the median filter-generated steps in the signal.

The plots shown in Fig. 72 display two peculiar characteristics:

- even though the tip is always negatively polarized ($V_{tip} = -10\,V$), at $V_G = 10\,V$ and $V_G = 4\,V$ the presence of the tip enhances the conduction across the device, while the opposite is true at $V_G = 8\,V$ and $V_G = 6\,V$.
- In every case, some ripples-on-a-pond-like features are formed around the position of the junction.

Similar features have been reported by Westervelt's group [126] in InAs nanowires and have been attributed to the presence of spurious disorder-induced quantum dots in the nanostructure.
Quantum dots host a phenomenon commonly known as Coulomb blockade, closely tied to the quantization of the electric charge: when a quantum dot is weakly coupled[3] to the surrounding environment, the number of electrons present inside the

2 The Nb stripe leading to the third electrode was severed.
3 The barriers delimiting the dot display low transmittivity to charge carriers.

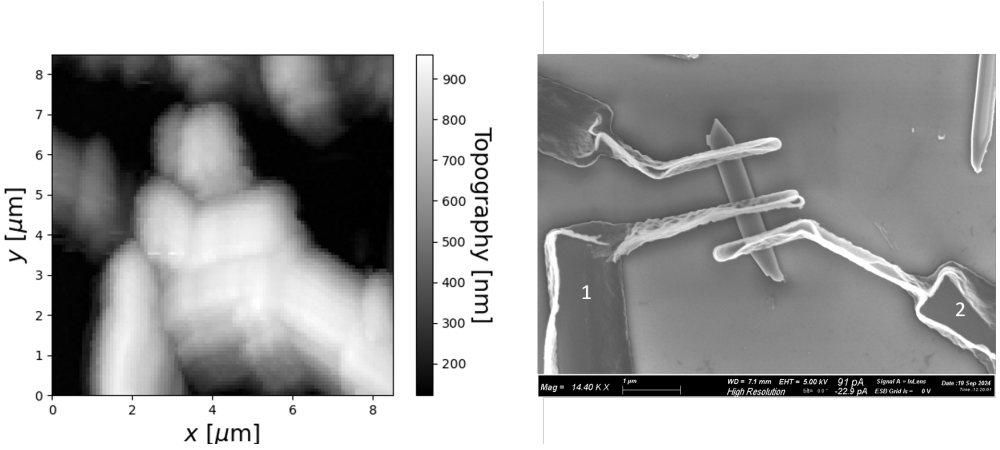

Figure 71: Left: 300 mK AFM topography map of device SC7 D4D4; right: SEM image of the same device; source electrode is indicated as 1, drain electrode as 2, the third electrode is floating.

dot is a well-defined quantum number that must assume an integer value. However, electrons are not charge-neutral particles, and therefore moving an electron in or out of the dot has a cost in terms of electrostatic energy. Therefore, quantum dots develop discrete "electrostatic energy levels" evenly spaced by the energy necessary to add one electron to the system, equal to $\Delta E = \frac{e^2}{C_{dot}}$, where C_{dot} is the capacitance of the dot with respect to the surrounding environment. Low-bias conductance through the dot is suppressed when its electrochemical potential lies in one of such electrostatic energy gaps, while it is enhanced when it lies close to one of the electrostatic energy levels, giving rise to well known diamond-shaped patterns in the differential conductance as a function of voltage difference across the dot and back-gate voltage [127].
The observed oscillations in the sample resistance as a function of the tip-to-device distance can therefore be explained as the transition of a disorder-generated quantum dot between different charge carrier occupation numbers. In order to put this hypothesis to test we have measured the transport characteristics of the device in DC voltage bias as a function of the back-gate potential, as reported in Fig. 73.
The plot of the numerically computed differential conductance[4] clearly shows diamond-like regions where the sample conductance is suppressed, which is in line with our interpretation.
In Fig. 74 we report a cut of the data displayed in Fig. 73 taken at zero voltage bias. The plot clearly shows periodic oscillations in the sample conductance as a function of back-gate voltage. By performing a least square fit with a sinusoidal model, the periodicity is estimated to be

$$V_{qd} = \frac{\Delta E}{e} \approx 0.26\,V, \tag{75}$$

corresponding to a back-gate to dot capacitance of the order of

$$C_{dot} = \frac{e^2}{\Delta E} \approx 0.7 \times 10^{-18}\,F \tag{76}$$

4 A linear baseline subtraction has been performed on the data in order to select only the fluctuations around the expected conductance increase.

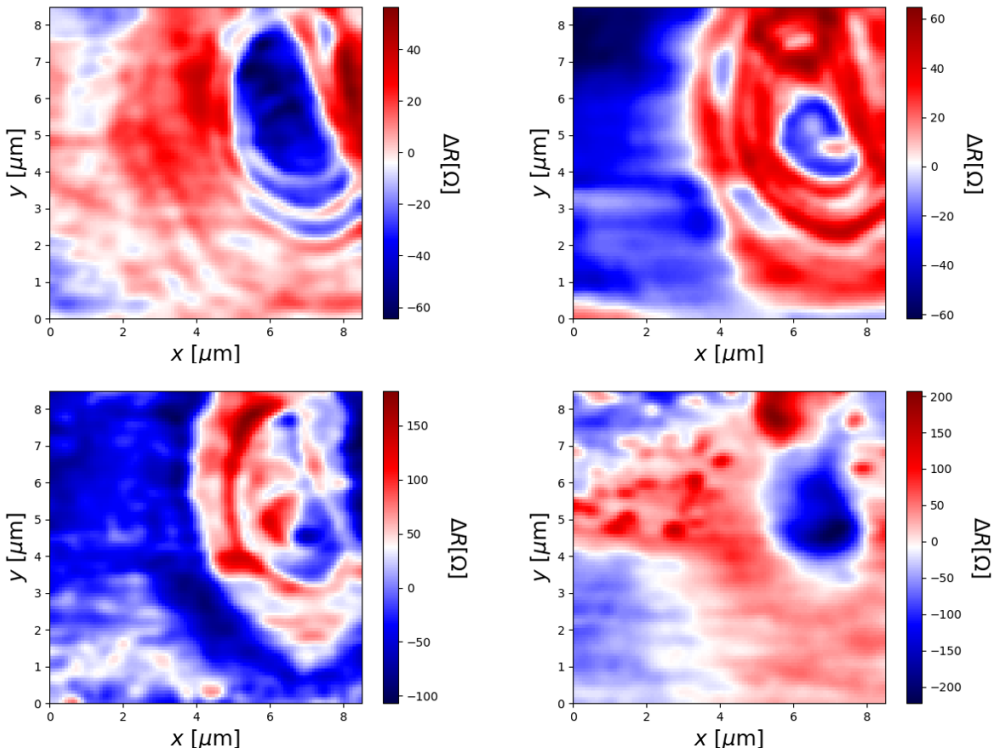

Figure 72: SGM resistance modulation maps as a function of tip position, $V_{tip} = -10\,V$. Evident signatures of ripples in the resistance modulation are present. Top left: $V_G = 10\,V$; top right: $V_G = 8\,V$; bottom left: $V_G = 6\,V$; bottom right: $V_G = 4\,V$.

which is of the same order of magnitude of the back-gate to dot capacitances observed in Ref. [126] strengthening our interpretation.
Once we have established the nature of these ripples in the resistance maps, we have analysed them in order to find how many electrons get pushed away from the quantum dot due to the depleting action of the charged tip.
To do so, we have located the local minima and maxima in the SGM resistance maps by using the *argrelextrema* function in the *scipy* library, reporting the result in Fig. 75. As already noticed in Fig. 72, these plots display alternating ring-like features: to every "resistance local maxima"-"resistance local minima" pair of rings corresponds one electron that gets electrostatically pushed out of the dot.
In particular, we noticed that the tip was able to push away 4 electrons from the dot at $V_G = 10\,V$, 3 electrons at $V_G = 8\,V$, 2 electrons at $V_G = 6\,V$ and just one electron at $V_G = 2\,V$. It can be noticed that the number of rings increases with the back-gate voltage and their relative distance gets reduced. This can be interpreted as a gate-induced increase in C_{dot} and can be explained as a manifestation of the increasingly efficient electrostatic screening of the dot as its surrounding environment gets more and more populated by charge carriers.
In conclusion, by Scanning Gate Microscopy and transport experiments we have fully characterized the behaviour of a defected InSb nanoflag-based device, unveiling the possibility of using SGM as a diagnostic technique: in fact, after this analysis, we understood the reason why the sample did not display any superconductive behaviour, i.e., due to the presence of disordered structures in the system.

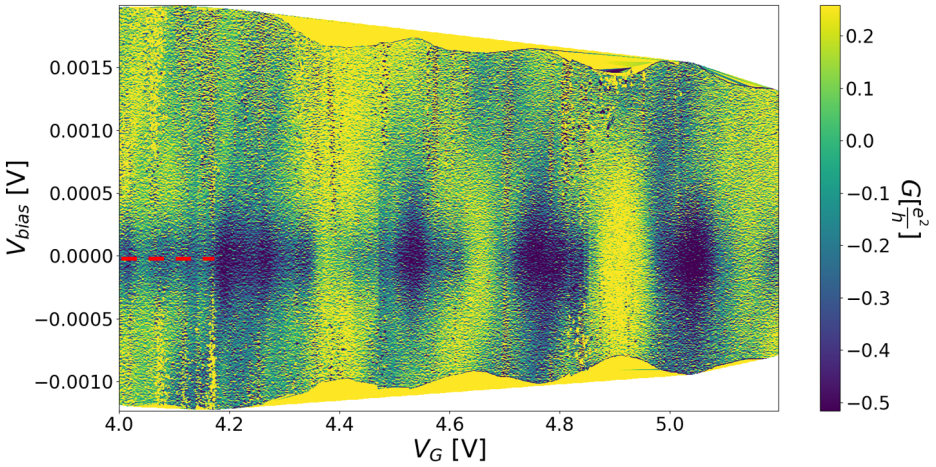

Figure 73: Numerically computed differential conductance as a function of voltage difference across the junction and back-gate voltage; signatures of diamond-like regions of conductance suppression close to zero bias are present. The red dashed line indicates the voltage bias value at which data displayed in Fig. 74 have been extracted.

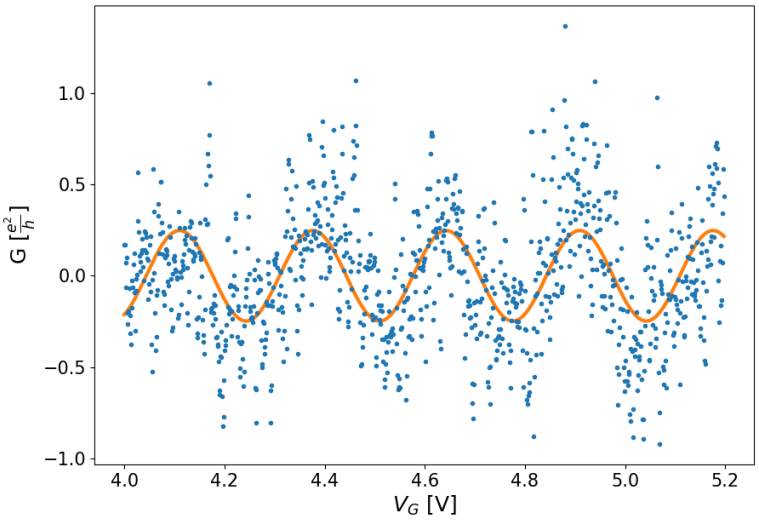

Figure 74: Cut of Fig. 73 taken at $V_{bias} = 0$ V; the plot displays periodicity in the conductance oscillations; in orange: least squares fit with a sinusoidal model.

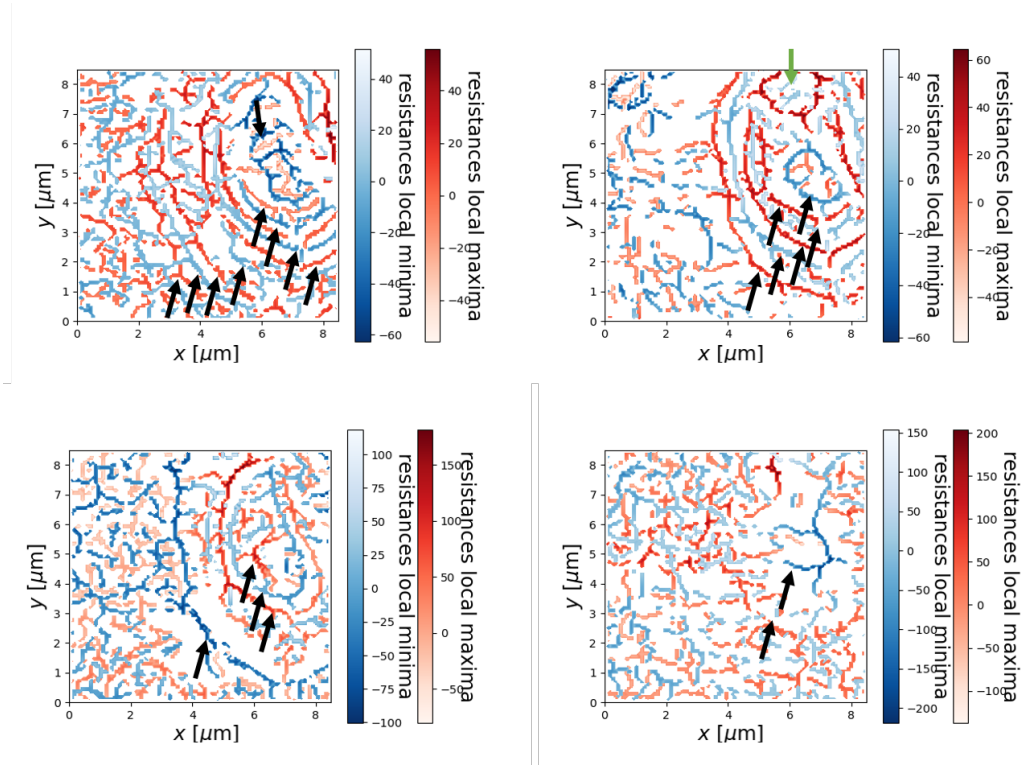

Figure 75: Numerically determined local minima and maxima of the plots reported in Fig. 72; black lines indicate the positions of rings corresponding to local minima and maxima, while the green arrow highlights the position of an ancillary structure detected at $V_G = 8\,V$; top left: $V_G = 10\,V$; top right: $V_G = 8\,V$; bottom left: $V_G = 6\,V$; bottom right: $V_G = 4\,V$.

Finally, we report the first demonstration of Scanning Gate microscopy on superconducting weak links, obtained in device SGM1 D8D2 and, a few days later, in device SGM3 H4D2.

6.4.1 *Tip-induced critical current modulation*

In order to demonstrate tip-induced critical current modulation, device SGM1 D8D2 has been set into the following working conditions:

- the tip has then been placed in the middle of the junction at a safety distance of 100 nm above the highest point recorded in a previously acquired AFM topography map, as reported in Fig. 76.
- the back-gate voltage has been set to $V_G = 9.5\,V$, a point positioned in a voltage interval where the requirements of non-negligible critical current back-gate dependence and limited fluctuations are both met, as shown in Fig. 77;

Then, by keeping the tip position fixed, we have acquired I-V curves in a 4-wire DC current bias configuration for different values of the tip potential.
The critical current has been determined following the same algorithm described in Section 5.3 of this work; however, the presence of the tip close to the junction increased the voltage signal noise, requiring to change the threshold voltage difference to $V_t = 4\mu V$.
Critical current measurements as a function of the tip-to-sample voltage difference are reported in Fig. 78, showing a clear critical current reduction when $V_{tip} < 0$ and an enhancement when $V_{tip} > 0$.
By comparing Fig. 77 and Fig. 78, we noticed a critical current reduction when the tip is placed close to the junction with respect to when it is far away from it: we attribute this to the oscillation of the AFM tip, which introduces a limited amount of noise in the system.
We recorded a critical current modulation of a few nA, which is in agreement with the theoretical predictions of [33] considering the width and critical current of the junction under investigation. By performing a least squares fit with a linear model, we obtained a critical current modulation efficiency $\alpha_{tip} = 0.35\,\frac{nA}{V}$.
Furthermore, we performed a least squares fit with a linear model on the back-gate voltage critical current modulation curve in the proximity of the working point (as shown in Fig. 77), obtaining a critical current modulation efficiency $\alpha_G = 6.5\,\frac{nA}{V}$: this indicates that, in these conditions, the effect of applying 10 V on the tip is equivalent to a variation in the back-gate voltage of about 0.5 V. This value of lever arm is also roughly consistent with the value obtained at 77 K (see Section 6.2).
Such trends have been reproduced over multiple acquisitions, confirming that the tip exerts an influence on the superconductive behaviour of the sample, opening up the possibility of performing SGM critical current maps.

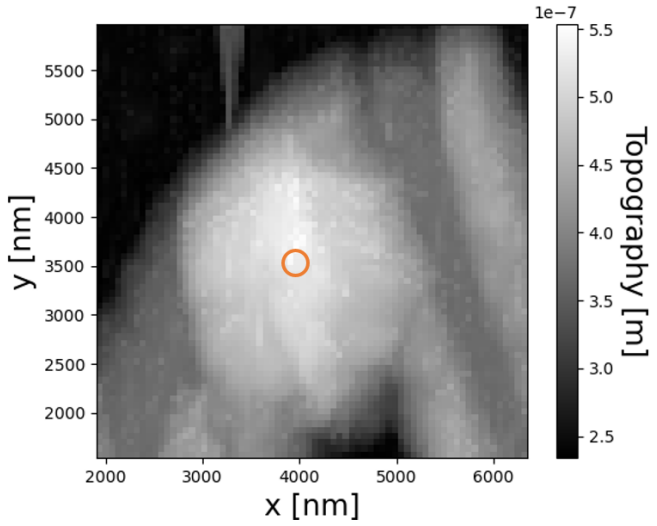

Figure 76: Low temperature AFM topography map of device SGM1 D8D2. The tip position for the measurements is indicated by an orange circle.

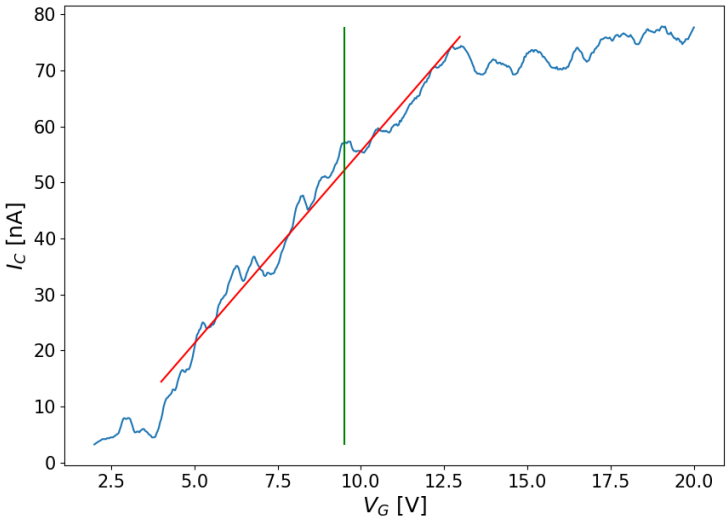

Figure 77: Critical current as a function of the back-gate voltage; the signal has been filtered through a linear Savitzky-Golay filter with window equal to ten points. The green line indicates the position of the working point. The red line corresponds to the best fit with a linear model of the back-gate critical current modulation in the neighbourhood of the working point. The fit results in a back-gate efficiency $\alpha_G = 0.35\,\frac{\mathrm{nA}}{\mathrm{V}}$.

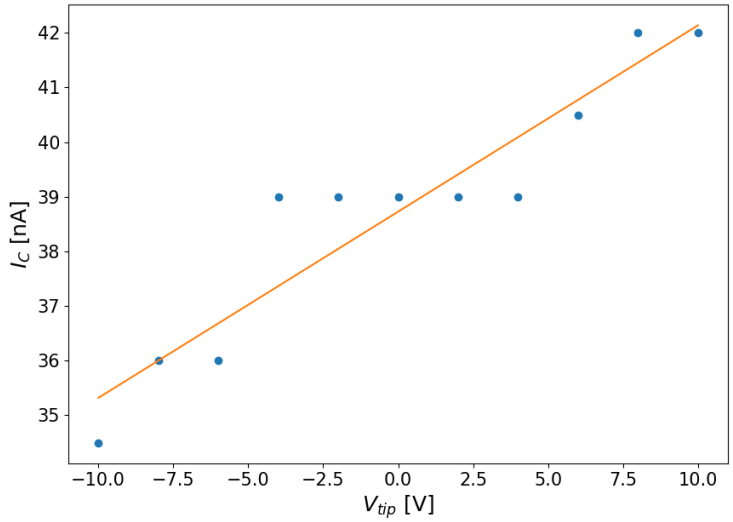

Figure 78: Critical current as a function of tip-to-sample voltage difference V_{tip}; device SGM1 D8D2, $V_G = 9.5\,V$, tip position indicated in Fig. 76. The best fit curve of the displayed data with a linear model is shown in orange.

6.4.2 *First scanning gate critical current maps*

In order to perform critical current maps, we applied the path mode protocol previously described in Section 5.3. The tip is scanned maintaining a constant vertical distance of 100 nm from the topmost recorded point in a previously acquired reference topography and is kept at a fixed voltage difference $V_{tip} = -10\,V$ with respect to the sample, in order to induce charge carriers depletion.
The first critical current map has been acquired on device SGM1 D8D2 in a 4-wire DC current bias setup, using the NiDAQ acquisition board for both signal generation and acquisition at its maximum sampling frequency of $f = 5\,kHz$. The back-gate potential has been set to $V_G = 9.5\,V$, following considerations already reported in Section 6.4.1.
The main disadvantage of using the acquisition board is the presence of intense 50 Hz noise pickup in the collected data, as displayed by the I-V curve reported in Fig. 79.
In order to extract the critical current from the raw data it is necessary to filter out such noise as much as possible: this has been done by performing a mobile average with a window width equal to 100 points, corresponding to an integration time of 0.025 s, that is the period of a 50 Hz oscillation. An example of a filtered signal is reported in Fig. 79, showing that the data processing pipeline does not alter the overall trend and features of the raw data while eliminating the background noise.
Critical current has then been determined following the procedure described in Section 5.3 by setting a threshold voltage difference equal to $V_t = 5\mu V$ following considerations related to the amplitude of the background noise in the dissipationless regime.
Finally, the first critical current modulation map is reported in Fig. 80 alongside a reference topography map of the device: as expected, it shows a clear reduction of

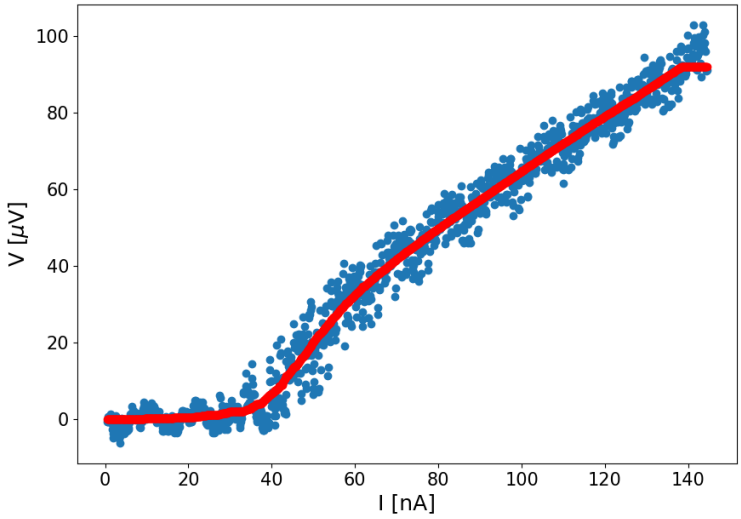

Figure 79: Raw data of an I-V curve of device SGM1 D8D2 acquired through the NiDAQ acquisition board; in red: data after the filtering procedure.

the supercurrent of the device, indicated by the blue area in the middle of the plot. In order to assess the reproducibility of this result, a similar experiment has been performed on device SGM3 H4D2. The measurements have been performed in a 3-wire DC current bias setup maintaining the same operative conditions as in the previous experiment, with the exception of the back-gate voltage, which has been set to $V_G = 6\,V$, in order to adapt to the device-dependent back-gate modulation behaviour.
Data have been analysed following the same pipeline described in the first part of this paragraph, resulting in Fig. 81. As in the previous experiment, also in this case a region in which the junction's supercurrent is reduced by the presence of the tip is present. However, in this case it is less straightforward to determine the junction's position from the reference topography due to bad tip quality: in particular, this could be a case of "double tip", which is a common issue in Scanning Probe Microscopy and results in doubling the topography features.
From the SEM images of the device in question, reported in Fig. 81, it is possible to understand the collected topography map as the partial superposition of two topography patterns of the device shifted one with respect to the other in the y direction, confirming the "double tip" hypothesis.
The location of the supercurrent suppression spot reported in Fig. 81, which covers completely only one of the two topography patterns, led us to the following hypothesis:

- two effective AFM tips have developed from the original one due to usage-driven deformation and material pickup during previous scans;
- these two tips are not in electrical connection with each other (otherwise we would have recorded a depletion spot covering both of the topography patterns of the sample);

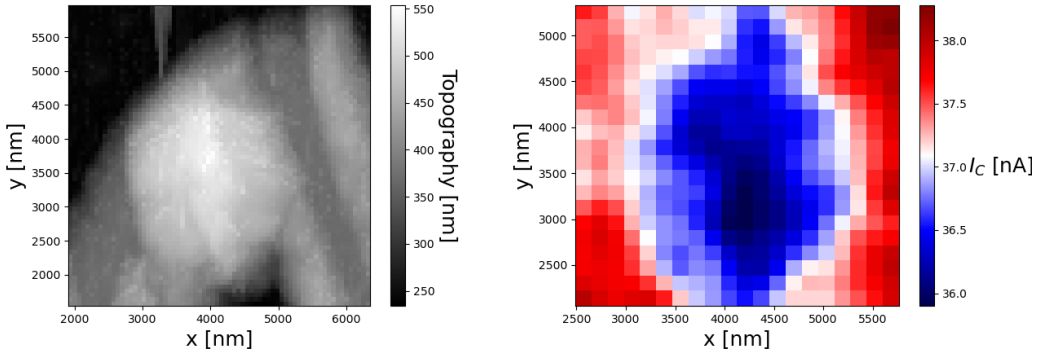

Figure 80: Critical current modulation map of device SGM1 D8D2; on the left: reference AFM topography of the device; on the right: 20 pixel x 20 pixel critical current map as a function of the position of the tip; Gaussian filter with $\sigma = 1$ pixel has been performed to suppress background noise. $V_{tip} = -10\,V$, $V_G = 9.5\,V$.

- the tip that experiences the externally applied potential V_{tip} is the one that generates the topography features located at lower y coordinate; additional topography features are therefore to be interpreted as "shadows" of the original one.

In order to put this hypothesis to test, we have performed a normal state SGM experiment on device SGM3 H4D2. In order to completely suppress the presence of any superconductive behaviour, we have operated at a back-gate voltage of $V_G = 1.5\,V$ (close to the device pinch-off condition) and at a DC current bias of 100 nA, far greater than the critical critical current of the device under study. Measurements were acquired in a flying mode 3-wire setup maintaining a safe distance of 100 nm and a tip polarization of $V_{tip} = -10\,V$.
The resulting resistance modulation map is reported in Fig. 82, which displays a resistance enhancement spot in the region corresponding to the critical current reduction spot detected in Fig. 81, confirming our interpretation of the critical current modulation data.
In conclusion, we have reported the first SGM critical current modulation maps, demonstrating the possibility of manipulating the behaviour of superconductive weak links through a charged AFM tip.

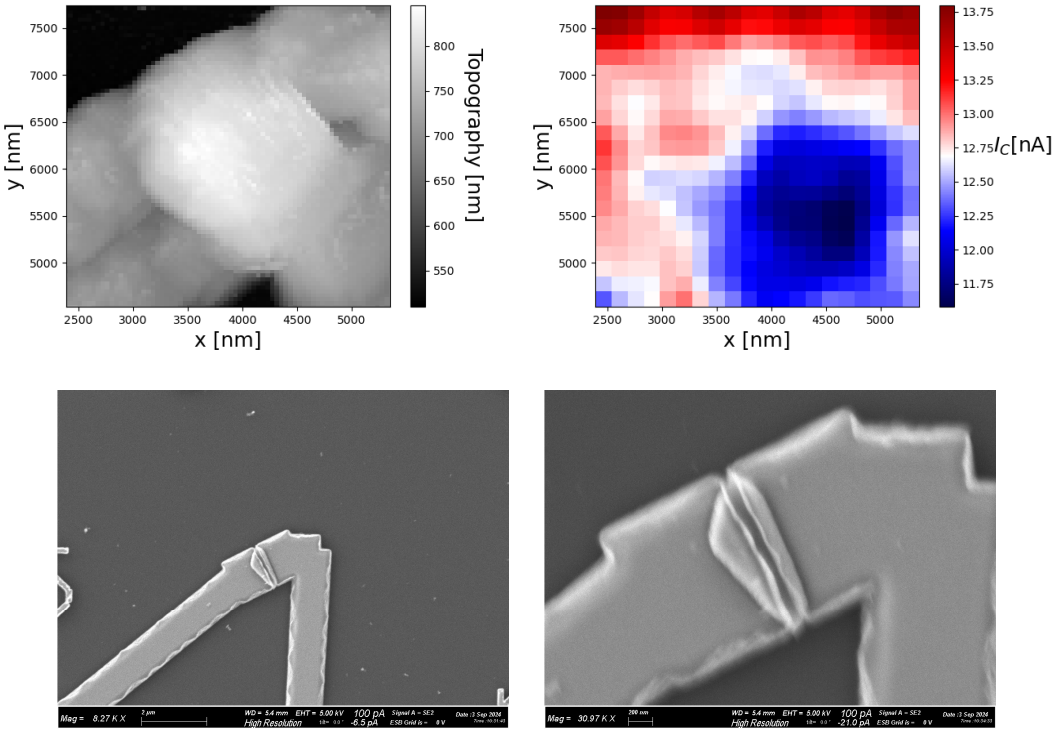

Figure 81: Critical current modulation map of device SGM3 H4D2; top left: reference AFM topography of the device; top right: 20 pixels x 20 pixels critical current map as a function of the position of the tip; Gaussian filter with $\sigma = 1$ pixel has been performed to suppress background noise. $V_{tip} = -10\,V$, $V_G = 6\,V$. Bottom: SEM images of the device under study.

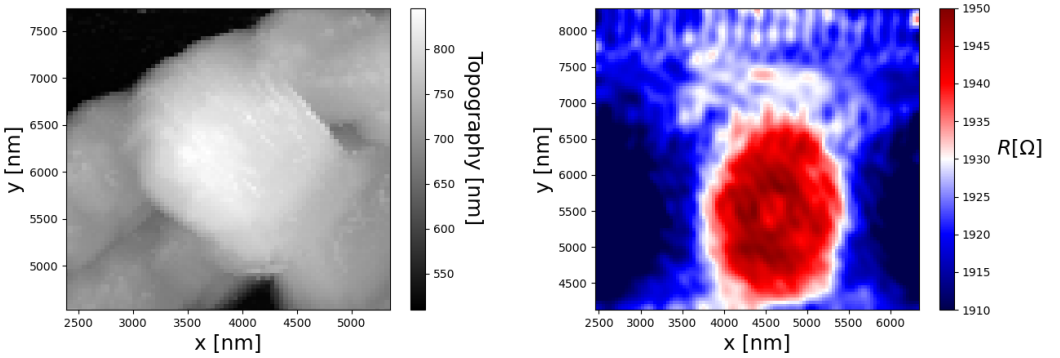

Figure 82: Normal state resistance modulation map of device SGM3 H4D2; left: reference AFM topography of the device; right: 100 pixels x 100 pixels normal resistance map as a function of the position of the tip; Gaussian filter with $\sigma = 1$ pixel has been performed to suppress background noise. $V_{tip} = -10\,V$, $V_G = 1.5\,V$.

7

CONCLUSIONS AND OUTLOOK

Within this thesis work, we have studied InSb nanoflag-based superconducting weak links in both conventional electronic transport and scanning probe experiments. First of all, complete characterization of the low temperature (300 mK) behaviour of said devices has been performed, leading to the following original results:

- the first observation of Weak Anti-Localization in NEST-fabricated devices, resulting in the measurement of the Rashba spin orbit coupling parameter $\alpha \approx 0.17$ eVÅ;
- the first observation at 300 mK at NEST of fully developed side lobes in the Fraunhofer pattern of an InSb nanoflag-based Josephson junction (SGM1 D8D2) (Fig. 47);
- the observation of a record-high, but fully gate tunable, switching current of $I_{sw} \approx 700$ nA in device SGM3 H5D1 (Fig. 55).
- in the same device, the observation of a proximity-induced superconducting gap $\Delta^\star \approx 0.47$ eV, corresponding to a Cooper pair breaking parameter $\gamma_B \approx 3.4$, ultimately demonstrating that using pure Nb electrodes leads to greater superconductor-InSb interface transparency with respect to previous Nb/Ti designs.

All of these results mark the recent advancements made in device fabrication and rise novel questions to be addressed in future experiments, e.g., concerning the nature of critical current fluctuations (Fig. 45) and that of the magnetic field-induced differential conductance oscillations observed in proximity to the Fraunhofer side lobes (Fig. 47).
Secondly, we have performed the first low temperature scanning probe experiments on InSb nanoflag-based devices including:

- the demonstration of sub-100 nm resolution AFM topography maps in ideal tip conditions while preserving device integrity;
- the first normal state Scanning Gate Microscpy measurements on InSb nanoflag-based Josephson junctions, unveiling the possibility of using SGM as a diagnostic technique to identify disorder-induced defects;
- the first Scanning Gate Microscopy critical current modulation maps on superconducting weaks links.

This last achievement is a proof of principle that will set a novel path for future experiments to characterise and manipulate the superconducting behaviour of hybrid systems at a local level.
In order to understand the next steps to take it is necessary to review the main issues that we have experienced in this Master's thesis work. To begin with, the

reported SGM maps lack in spatial resolution due to both poor AFM tip quality and a large sample-to-tip distance. In fact, taking into account the Nb electrode thickness (160 nm) and the selected safety distance (100 nm), an effective sample-to-tip distance in the order of 300 nm is obtained. For geometrical reasons, this corresponds approximately to the width of the tip-induced depletion spot, which is not negligible with respect to the lateral dimensions of the studied junctions. Furthermore, the tip-to-sample capacitive coupling decreases with increasing sample-to-tip distance, limiting the experiment signal to noise ratio.

Therefore, it is of pivotal importance for the future development of the technique to find ways of reducing such distance. The main limitation to this lies in the extreme fragility of the systems under study to electrostatic perturbations: as reported in the section dedicated to SGM at 77 K, even the slightest electrical contact between either the metallic leads or the semiconducting region and the charged tip is detrimental to the experiment and to device integrity. Even at the chosen safety distance of 100 nm, most of the studied devices have exploded due to electrostatic shocks, highlighting the need for better electrical insulation between the system and the tip. This can be achieved by depositing over the region of interest a few-nm thick layer of high performance dielectric (e.g. HfO_2) by atomic layer deposition. This will allow to perform Scanning Gate Microscopy with the polarised tip placed directly in contact with the dielectric layer while at the same time preventing the creation of electrical discharges and increasing the tip-to-sample capacitance.

At the same time, signal to noise ratio can be increased by studying devices with higher supercurrent densities, like SGM3 H5D1[1]; as stated in [33], the tip-induced critical current suppression is predicted to scale linearly with the critical current density in the junction: the observed increase by an order of magnitude in the critical current should reflect in an increase in the tip-modulation signal of the same factor (from few nA to few 10 nA). Given the ever-increasing device quality, we do not doubt that SGM experiments on similar devices will be performed in the near future.

Once all of these developments come into play, there will be the possibility of acquiring well-resolved critical current modulation maps opening up a way to perform supercurrent flow imaging, to better understand the physics of superconducting weak links.

Finally, it is worth mentioning that our study opens up a promising way of investigating and manipulating via SGM topological phases at a local level, a necessary step in the path to engineering devices suitable to perform fault-tolerant quantum computation. In fact, the presence of the polarized tip can be used to locally deplete a topological device, inducing a local topological phase transitions and leading to the formation of Majorana zero modes. Scanning the charged tip over multi-terminal topological devices [128] could result in a promising way to displace such Majorana Zero Modes to implement braiding operations.

1 There has been no occasion of performing SGM experiments on device SGM3 H5D1 since it was located in a region of the sample that was impossible to reach with the tip.

BIBLIOGRAPHY

1. Braginski, A. I. Superconductor Electronics: Status and Outlook. *J. Supercond. Nov. Magn.* **32,** 23–44. https://link.springer.com/article/10.1007/s10948-018-4884-4 (2019).
2. Krantz, P. *et al.* A quantum engineer's guide to superconducting qubits. *Appl. Phys. Rev.* **6.** https://doi.org/10.1063/1.5089550 (2019).
3. Likharev, K. K. Superconducting weak links. *Reviews of Modern Physics* **51.** https://doi.org/10.1103/RevModPhys.51.101 (1979).
4. Topinka, M. *et al.* Coherent branched flow in a two-dimensional electron gas. *Nature,* 183–186. https://doi.org/10.1038/35065553 (2001).
5. Salimian, S. *et al.* Gate-controlled supercurrent in ballistic InSb nanoflag Josephson junctions. *Applied Physics Letters* **119,** 214004. https://doi.org/10.1063/5.0071218 (2021).
6. Tinkham, M. *Introduction to superconductivity 2nd ed.* (Dover Publications, 2004).
7. Lee, G. & Lee, H. Proximity coupling in superconductor-graphene heterostructures. *Reports on Progress in Physics.* https://iopscience.iop.org/article/10.1088/1361-6633/aaafe1 (2018).
8. Schaepers, T. *Superconductor / semiconductor junctions* (Springer, 2001).
9. De Gennes, P. G. *Superconductivity of metals and alloys* (Westview press, 1969).
10. Ginzburg, V. L. & Landau, L. D. in *Collected Papers of L.D. Landau* (ed ter Haar, D.) 546–568 (Pergamon, 1965). https://www.sciencedirect.com/science/article/pii/B978008010586450078X.
11. Bardeen, J., Cooper, L. N. & Schrieffer, J. R. Theory of Superconductivity. *Phys. Rev.* **108,** 1175–1204. https://link.aps.org/doi/10.1103/PhysRev.108.1175 (5 1957).
12. Gor'kov, L. P. Microscopic Derivation of the Ginzburg-Landau Equations in the Theory of Superconductivity. *Soviet Physics JETP* **36,** 1364–1367 (1959).
13. Larsen, T. W. *et al.* Semiconductor-Nanowire-Based Superconducting Qubit. *Phys. Rev. Lett.* **115.** https://link.aps.org/doi/10.1103/PhysRevLett.115.127001 (2015).
14. De Lange, G. *et al.* Realization of Microwave Quantum Circuits Using Hybrid Superconducting-Semiconducting Nanowire Josephson Elements. *Phys. Rev. Lett.* **115.** https://link.aps.org/doi/10.1103/PhysRevLett.115.127002 (2015).
15. Ren, H. *et al.* Topological superconductivity in a phase-controlled Josephson junction. *Nature* **569,** 93–98. https://doi.org/10.1038/s41586-019-1148-9 (2019).

16. Fornieri, A. *et al.* Evidence of topological superconductivity in planar Josephson junctions. *Nature* **569,** 89–92. https://doi.org/10.1038/s41586-019-1068-8 (2019).

17. Lesser, O. *et al.* Phase-induced topological superconductivity in a planar heterostructure. *Proceedings of the National Academy of Sciences* **118,** e2107377118. https://www.pnas.org/doi/abs/10.1073/pnas.2107377118 (2021).

18. Pientka, F. *et al.* Topological Superconductivity in a Planar Josephson Junction. *Phys. Rev. X* **7,** 021032. https://link.aps.org/doi/10.1103/PhysRevX.7.021032 (2017).

19. Hays, M. & et al. Coherent manipulation of an Andreev spin qubit. *Science* **373,** 430–433. https://www.science.org/doi/10.1126/science.abf0345 (2021).

20. Pita-Vidal, M. *et al.* Direct manipulation of a superconducting spin qubit strongly coupled to a transmon qubit. *Nat. Phys.* **19,** 1110–1115. https://doi.org/10.1038/s41567-023-02071-x (2023).

21. Beenakker, C. W. J. & van Houten, H. The Superconducting Quantum Point Contact. *Nanostructures and Mesoscopic Systems.* https://doi.org/10.1016/B978-0-12-409660-8.50051-1 (1992).

22. Blonder, G. E., Tinkham, M. & Klapwijk, T. M. Transition from metallic to tunneling regimes in superconducting microconstrictions: Excess current, charge imbalance, and supercurrent conversion. *Phys. Rev. B* **25,** 4515–4532. https://link.aps.org/doi/10.1103/PhysRevB.25.4515 (1982).

23. Tang, H. X., Wang, Z. D. & Zhang, Y. Normal reflection effect on the critical current in a clean-limit superconductor-normal-metal-superconductor junction. *Zeitschrift fur Physik B Condensed Matter.* https://doi.org/10.1007/s002570050220 (1997).

24. Beenakker, C. W. J. Universal limit of critical-current fluctuations in mesoscopic Josephson junctions. *Phys. Rev. Lett.* **67,** 3836–3839. https://link.aps.org/doi/10.1103/PhysRevLett.67.3836 (1991).

25. Kulik, I. O. & Omel'yanchuk, A. N. Properties of superconducting microbridges in the pure limit. *Sov. J. Low Temp. Phys.,* 459–462. https://doi.org/10.1063/10.0029534 (1977).

26. Guel, O. *et al.* Hard Superconducting Gap in InSb Nanowires. *Nano Letters* **17,** 2690–2696. https://doi.org/10.1021/acs.nanolett.7b00540 (2017).

27. Aminov, B. A., Golubov, A. A. & Kupriyanov, M. Y. Quasiparticle current in ballistic constrictions with finite transparencies of interfaces. *Phys. Rev. B* **53,** 365–373. https://link.aps.org/doi/10.1103/PhysRevB.53.365 (1996).

28. Kjaergaard, M. *et al.* Transparent Semiconductor-Superconductor Interface and Induced Gap in an Epitaxial Heterostructure Josephson Junction. *Phys. Rev. Appl.* **7,** 034029. https://link.aps.org/doi/10.1103/PhysRevApplied.7.034029 (2017).

29. Octavio, M. *et al.* Subharmonic energy-gap structure in superconducting constrictions. *Phys. Rev. B* **27,** 6739–6746. https://link.aps.org/doi/10.1103/PhysRevB.27.6739 (1983).

30. Flensberg, K., Hansen, J. B. & Octavio, M. Subharmonic energy-gap structure in superconducting weak links. *Phys. Rev. B* **38,** 8707–8711. https://link.aps.org/doi/10.1103/PhysRevB.38.8707 (1988).

31. Bardas, A. & Averin, D. V. Electron transport in mesoscopic disordered superconductor–normal-metal–superconductor junctions. *Phys. Rev. B* **56,** R8518–R8521. https://link.aps.org/doi/10.1103/PhysRevB.56.R8518 (1997).

32. Yan, S. *et al.* Supercurrent, Multiple Andreev Reflections and Shapiro Steps in InAs Nanosheet Josephson Junctions. *Nano Letters* **23,** 6497–6503. https://doi.org/10.1021/acs.nanolett.3c01450 (2023).

33. Kaperek, K. *et al.* Theory of scanning gate microscopy imaging of the supercurrent distribution in a planar Josephson junction. *Phys. Rev. B* **106,** 035432. https://link.aps.org/doi/10.1103/PhysRevB.106.035432 (2022).

34. Dynes, R. C. & Fulton, T. A. Supercurrent Density Distribution in Josephson Junctions. *Phys. Rev. B* **3,** 3015–3023. https://link.aps.org/doi/10.1103/PhysRevB.3.3015 (1971).

35. Chen, S. *et al.* Current induced hidden states in Josephson junctions. *Nature Communications* **15.** https://doi.org/10.1038/s41467-024-52271-z (2024).

36. Hui, H.-Y. *et al.* Proximity-induced superconductivity and Josephson critical current in quantum spin Hall systems. *Phys. Rev. B* **90,** 224517. https://link.aps.org/doi/10.1103/PhysRevB.90.224517 (2014).

37. Li, S. *et al.* Coherent Charge Transport inBallistic InSb Nanowire Josephson-Junctions. *Scientific Reports.* https://www.nature.com/articles/srep24822 (2016).

38. Verma, I. *et al.* High-Mobility Free-Standing InSb Nanoflags Grown on InP Nanowire Stems for Quantum Devices. *ACS Applied Nano Materials* **4,** 5825–5833. https://doi.org/10.1021/acsanm.1c00734 (2021).

39. Verma, I. *et al.* Morphology control of single-crystal InSb nanostructures by tuning the growth parameters. *Nanotechnology* **31.** https://iopscience.iop.org/article/10.1088/1361-6528/ab9aee (2020).

40. Csonka, S., Geresdi, A. & Sorba, L. Ballistic transport in InSb nanowires as measured by quantized conductance plateaux. *tech. rep.* https://www.andqc.eu/upload/files/D1_3_Ballistic_InSb_nanowires_final.pdf (2021).

41. Xue, J. *et al.* Gate defined quantum dot realized in a single crystalline InSb nanosheet. *Applied Physics Letters* **114,** 023108. https://doi.org/10.1063/1.5064368 (2019).

42. Zhi, J. *et al.* Coexistence of induced superconductivity and quantum Hall states in InSb nanosheets. *Phys. Rev. B* **99,** 245302. https://link.aps.org/doi/10.1103/PhysRevB.99.245302 (2019).

43. Bett, A. W. *et al.* III-V compounds for solar cell applications. *Appl. Phys. A* **69,** 119–129. https://doi.org/10.1007/s003390050983 (1999).

44. Eds Madelung, O., Roessler, U. & Schulz, M. *Indium antimonide (InSb), lattice parameter, thermal expansion: Datasheet from Landolt Boernstein - Group III Condensed Matter · Volume 41A1beta: Group IV Elements, IV-IV and I-V Compounds. Part b - Electronic, Transport, Optical and Other Properties* (SpringerMaterials).

45. Qu, F. *et al.* Quantized Conductance and Large g-Factor Anisotropy in InSb Quantum Point Contacts. *Nano Letters* **16,** 7509–7513. https://doi.org/10.1021/acs.nanolett.6b03297 (2016).

46. Moehle, C. M. *et al.* InSbAs Two-Dimensional Electron Gases as a Platform for Topological Superconductivity. *Nano Letters* **21,** 9990–9996. https://doi.org/10.1021/acs.nanolett.1c03520 (2021).

47. Chen, Y. *et al.* A double quantum dot defined by top gates in a single crystalline InSb nanosheet. *Chinese Phys. B* **30.** https://doi.org/10.1088/1674-1056/abff2e (2021).

48. Xiong, Z. *et al.* Van der Waals Epitaxial Growth of Ultrathin Indium Antimonide on Arbitrary Substrates through Low-Thermal Budget. *Adv. Mater.* **36,** 2402435. https://onlinelibrary.wiley.com/doi/10.1002/adma.202402435 (2024).

49. Topocondmat.org: web course on topology in condensed matter.

50. Stern, A. & Lindner, N. H. Topological Quantum Computatin: From Basic Concepts to First Experiments. *Science* **339,** 1179–1184. https://www.science.org/doi/abs/10.1126/science.1231473 (2013).

51. Fabian, J. *et al.* Semiconductor spintronics. *Acta Physica Slovaca. Reviews and Tutorials* **57.** http://dx.doi.org/10.2478/v10155-010-0086-8 (2007).

52. Sladek, R. J. Effective Masses of Electrons in Indium Arsenide and Indium Antimonide. *Phys. Rev.* **105,** 460–464. https://link.aps.org/doi/10.1103/PhysRev.105.460 (1957).

53. Vurgaftman, I., Meyer, J. R. & Ram-Mohan, L. R. Band parameters for III-V compound semiconductors and their alloys. *Journal of Applied Physics* **89,** 5815–5875. https://doi.org/10.1063/1.1368156 (2001).

54. Litvinenko, K. L. *et al.* Temperature dependence of the electron Landé g factor in InSb and GaAs. *Phys. Rev. B* **77,** 033204. https://link.aps.org/doi/10.1103/PhysRevB.77.033204 (2008).

55. Dresselhaus, G. Spin-Orbit Coupling Effects in Zinc Blende Structures. *Phys. Rev.* **100,** 580–586. https://link.aps.org/doi/10.1103/PhysRev.100.580 (1955).

56. Rashba, E. Properties of semiconductors with an extremum loop. I. Cyclotron and combinational resonance in a magnetic field perpendicular to the plane of the loop. *Sov. Phys.-Solid State 2, 1109* (1960).

57. Winfried Moench. *Semiconductor Surfaces and Interfaces* (Springer, 2001).

58. King, P. D. C. *et al.* Surface electronic properties of clean and S-terminated InSb(001) and (111)B. *Journal of Applied Physics* **104,** 083709. https://doi.org/10.1063/1.3000567 (2008).

59. Gobeli, G. W. & Allen, F. G. Photoelectric Properties of Cleaved GaAs, GaSb, InAs, and InSb Surfaces; Comparison with Si and Ge. *Phys. Rev.* **137,** A245–A254. https://link.aps.org/doi/10.1103/PhysRev.137.A245 (1965).

60. Lei, Z. *et al.* Quantum transport in high-quality shallow InSb quantum wells. *Applied Physics Letters* **115,** 012101. https://doi.org/10.1063/1.5098294 (2019).

61. Orr, J. M. S. *et al.* Electronic transport in modulation-doped InSb quantum well heterostructures. *Phys. Rev. B* **77,** 165334. https://link.aps.org/doi/10.1103/PhysRevB.77.165334 (2008).

62. Khodaparast, G. A. *et al.* Spectroscopy of Rashba spin splitting in InSb quantum wells. *Phys. Rev. B* **70,** 155322. https://link.aps.org/doi/10.1103/PhysRevB.70.155322 (2004).

63. Goldammer, K. J. *et al.* High-mobility electron systems in remotely-doped InSb quantum wells. *Journal of Crystal Growth* **201-202,** 753–756. https://www.sciencedirect.com/science/article/pii/S0022024898015267 (1999).

64. Ke, C. T. *et al.* Ballistic superconductivity and tunable pi-junctions in InSb quantum wells. *Nature Communications* **10.** https://doi.org/10.1038/s41467-019-11742-4 (2019).

65. Guiducci, S. *et al.* Full electrostatic control of quantum interference in an extended trenched Josephson junction. *Phys. Rev. B* **99,** 235419. https://link.aps.org/doi/10.1103/PhysRevB.99.235419 (2019).

66. Moehle, C. M. *et al.* Controlling Andreev Bound States with the Magnetic Vector Potential. *Nano Letters* **22,** 8601–8607. https://doi.org/10.1021/acs.nanolett.2c03130 (2022).

67. Ten Haaf, S. L. D. *et al.* A two-site Kitaev chain in a two-dimensional electron gas. *Nature* **630,** 329–334. https://doi.org/10.1038/s41586-024-07434-9 (2024).

68. Prada, E. *et al.* From Andreev to Majorana bound states in hybrid superconductor-semiconductor nanowires. *Nature Review Physics,* 575–594. https://doi.org/10.1038/s42254-020-0228-y (2020).

69. Bordin, A. *et al.* Crossed Andreev Reflection and Elastic Cotunneling in Three Quantum Dots Coupled by Superconductors. *Phys. Rev. Lett.* **132,** 056602. https://link.aps.org/doi/10.1103/PhysRevLett.132.056602 (2024).

70. Zatelli, F. *et al.* Robust poor man's Majorana zero modes using Yu-Shiba-Rusinov states. *Nature Communications* **15.** https://doi.org/10.1038/s41467-024-52066-2 (2024).

71. Prosko, C. G. *et al.* Flux-tunable Josephson effect in a four-terminal junction. *Phys. Rev. B* **110,** 064518. https://link.aps.org/doi/10.1103/PhysRevB.110.064518 (2024).

72. De la Mata, M. *et al.* Twin-Induced InSb Nanosails: A Convenient High Mobility Quantum System. *Nano Letters* **16,** 825–833. https://doi.org/10.1021/acs.nanolett.5b05125 (2016).

73. Pan, D. *et al.* Free-Standing Two-Dimensional Single-Crystalline InSb Nanosheets. *Nano Letters* **16,** 834–841. https://doi.org/10.1021/acs.nanolett.5b04845 (2016).

74. Gazibegovic, S. *et al.* Bottom-Up Grown 2D InSb Nanostructures. *Advanced Materials* **31,** 1808181. https://onlinelibrary.wiley.com/doi/abs/10.1002/adma.201808181 (2019).

75. Rossi, M. *et al.* Merging Nanowires and Formation Dynamics of Bottom-Up Grown InSb Nanoflakes. *Advanced Functional Materials* **33,** 2212029. https://onlinelibrary.wiley.com/doi/abs/10.1002/adfm.202212029 (2023).

76. De Vries, F. K. *et al.* Crossed Andreev reflection in InSb flake Josephson junctions. *Phys. Rev. Res.* **1,** 032031. https://link.aps.org/doi/10.1103/PhysRevResearch.1.032031 (2019).

77. Kang, N. *et al.* Two-Dimensional Quantum Transport in Free-Standing InSb Nanosheets. *Nano Letters* **19,** 561–569. https://doi.org/10.1021/acs.nanolett.8b04556 (2019).

78. Chen, Y. *et al.* Strong and tunable spin-orbit interaction in a single crystalline InSb nanosheet. *npj 2D Mater Appl* **5.** https://doi.org/10.1038/s41699-020-00184-y (2021).

79. Turini, B. *et al.* Josephson Diode Effect in High-Mobility InSb Nanoflags. *Nano Letters* **22,** 8502–8508. https://doi.org/10.1021/acs.nanolett.2c02899 (2022).

80. Iorio, A. *et al.* Half-integer Shapiro steps in highly transmissive InSb nanoflag Josephson junctions. *Phys. Rev. Res.* **5,** 033015. https://link.aps.org/doi/10.1103/PhysRevResearch.5.033015 (2023).

81. Binnig, G. & Rohrer, H. Scanning tunneling microscopy—from birth to adolescence. *Rev. Mod. Phys.* **59,** 615–625. https://link.aps.org/doi/10.1103/RevModPhys.59.615 (1987).

82. Binnig, G., Quate, C. F. & Gerber, C. Atomic Force Microscope. *Phys. Rev. Lett.* **56,** 930–933. https://link.aps.org/doi/10.1103/PhysRevLett.56.930 (1986).

83. Nowak, D. B. *The Design of a Novel Tip Enhanced Near-field Scanning Probe Microscope for Ultra-High Resolution Optical Imaging* PhD thesis (Portland State University, 2010).

84. Eriksson, M. A. *et al.* Cryogenic scanning probe characterization of semiconductor nanostructures. *Applied Physics Letters* **69,** 671–673. https://doi.org/10.1063/1.117801 (1996).

85. LeRoy, B. J. *Imaging Coherent Electron Flow Through SemiconductorNanostructures.* PhD thesis (Harvard University, 2003).

86. M. A. Topinka, e. a. Imaging Coherent Electron Flow from a Quantum Point Contact. *Science,* 2323–2326. https://www.science.org/doi/10.1126/science.289.5488.2323 (2000).

87. Jura, M. P. *et al.* Unexpected features of branched flow through high-mobility two-dimensional electron gases. *Nature Physics* **3,** 841–845. https://doi.org/10.1038/nphys756 (2007).

88. LeRoy, B. J. *et al.* Imaging electron density in a two-dimensional electron gas. *Applied Physics Letter*, 4431–4433. https://doi.org/10.1063/1.1484548 (2002).

89. Percebois, G. J. *et al.* Reconstructing the potential configuration in a high-mobility semiconductor heterostructure with scanning gate microscopy. *SciPost Phys.* **15.** https://scipost.org/10.21468/SciPostPhys.15.6.242 (2023).

90. Jura, M. P. *et al.* Electron interferometer formed with a scanning probe tip and quantum point contact. *PHYSICAL REVIEW B* **80.** https://journals.aps.org/prb/abstract/10.1103/PhysRevB.80.041303 (2009).

91. Gold, C. *et al.* Local signatures of electron-electron scattering in an electronic cavity. *Phys. Rev. Research* **3.** https://journals.aps.org/prresearch/abstract/10.1103/PhysRevResearch.3.013287 (2021).

92. Aidala, K. E. *et al.* Imaging magnetic focusing of coherent electron waves. *Nature Physics* **3,** 464–468. https://doi.org/10.1038/nphys628 (2007).

93. Paradiso, N. *et al.* Imaging Fractional Incompressible Stripes in Integer Quantum Hall Systems. *Phys. Rev. Lett.* **108,** 246801. https://link.aps.org/doi/10.1103/PhysRevLett.108.246801 (2012).

94. Paradiso, N. *et al.* Imaging backscattering through impurity-induced antidots in quantum Hall constrictions. *Phys. Rev. B* **86,** 085326. https://link.aps.org/doi/10.1103/PhysRevB.86.085326 (2012).

95. Paradiso, N. *et al.* Selective control of edge-channel trajectories by scanning gate microscopy. *Physica E: Low-dimensional Systems and Nanostructures* **42,** 1038–1041. https://www.sciencedirect.com/science/article/pii/S1386947709005827 (2010).

96. Tomimatsu, T. *et al.* Probing the breakdown of topological protection: Filling-factor-dependent evolution of robust quantum Hall incompressible phases. *Phys. Rev. Research* **2.** https://doi.org/10.1103/PhysRevResearch.2.013128 (2020).

97. Braem, B. A. *et al.* Investigating energy scales of fractional quantum Hall states using scanning gate microscopy. *Phys. Rev. B* **93.** https://doi.org/10.1103/PhysRevB.93.115442 (2016).

98. Bours, L. *et al.* Manipulating quantum Hall edge channels in graphene through scanning gate microscopy. *Phys. Rev. B* **96.** https://doi.org/10.1103/PhysRevB.96.195423 (2017).

99. Aharon-Steinberg, A. *et al.* Long-range nontopological edge currents in charge-neutral graphene. *Nature* **593,** 528–534. https://doi.org/10.1038/s41586-021-03501-7 (2021).

100. Gold, C. *et al.* Scanning gate microscopy of localized states in a gate-defined bilayer graphene channel. *Phys. Rev. Research* **2.** https://doi.org/10.1103/PhysRevResearch.2.043380 (2020).

101. Marguerite, A. *et al.* Imaging work and dissipation in the quantum Hall state in graphene. *Nature* **575,** 628–633. https://doi.org/10.1038/s41586-019-1704-3 (2019).

102. Dou, Z. *et al.* Imaging Bulk and Edge Transport near the Dirac Point in Graphene Moiré Superlattices. *Nano. Lett.* **18,** 2530–2537. https://pubs.acs.org/doi/10.1021/acs.nanolett.8b00228 (2018).

103. Sakanashi, K. *et al.* Investigation of laser-induced-metal phase of MoTe2 and its contact property via scanning gate microscopy. *Nanotechnology* **31.** https://iopscience.iop.org/article/10.1088/1361-6528/ab71b8 (2020).

104. Bachtold, A. *et al.* Scanned Probe Microscopy of Electronic Transport in Carbon Nanotubes. *Phys. Rev. Lett.* **84,** 6082–6085. https://link.aps.org/doi/10.1103/PhysRevLett.84.6082 (2000).

105. Freitag, M. *et al.* Role of Single Defects in Electronic Transport through Carbon Nanotube Field-Effect Transistors. *Phys. Rev. Lett.* **89,** 216801. https://link.aps.org/doi/10.1103/PhysRevLett.89.216801 (2002).

106. Bozovic, D. *et al.* Plastic deformations in mechanically strained single-walled carbon nanotubes. *Phys. Rev. B* **67,** 033407. https://link.aps.org/doi/10.1103/PhysRevB.67.033407 (2003).

107. Denisov, A. O. *et al.* Microwave-Frequency Scanning Gate Microscopy of a Si/SiGeDouble Quantum Dot. *Nano Lett.* **22,** 4807–4813. https://doi.org/10.1021/acs.nanolett.2c01098 (2022).

108. Gildemeister, A. E. *et al.* Imaging a coupled quantum dot-quantum point contact system. *Journal of Applied Physics* **102,** 083703. https://doi.org/10.1063/1.2787163 (2007).

109. Huefner, M. *et al.* Spatial mapping and manipulation of two tunnel-coupled quantum dots. *Phys. Rev. B* **83,** 235326. https://link.aps.org/doi/10.1103/PhysRevB.83.235326 (2011).

110. Martins, F. *et al.* Imaging Electron Wave Functions Inside Open Quantum Rings. *Phys. Rev. Lett.* **99,** 136807. https://link.aps.org/doi/10.1103/PhysRevLett.99.136807 (2007).

111. Fan, Y. *et al.* Electric-field control of spin–orbit torque in a magnetically doped topological insulator. *Nature Nanotechnology* **11,** 352–359. https://doi.org/10.1038/nnano.2015.294 (2016).

112. Huefner, M. *et al.* Scanning gate microscopy measurements on a superconducting single-electron transistor. *Phys. Rev. B* **79,** 134530. https://link.aps.org/doi/10.1103/PhysRevB.79.134530 (2009).

113. Bhandari, S. *et al.* Imaging Andreev Reflection in Graphene. *Nano. Lett.* **20,** 4890–4894. https://doi.org/10.1021/acs.nanolett.0c00903 (2020).

114. Hegedues, M. & et al. In-situ scanning gate imaging of individual two-level material defects in live superconducting quantum circuits. *arXiv:2408.16660.* https://doi.org/10.48550/arXiv.2408.16660 (2024).

115. Paradiso, N. *Tomography and manipulation of quantum Hall edgechannels* PhD thesis (Scuola Normale Superiore, 2012).

116. Karrai, K. & Tiemann, I. Interfacial shear force microscopy. *Phys. Rev. B* **62,** 13174–13181. https://link.aps.org/doi/10.1103/PhysRevB.62.13174 (2000).

117. Guiducci, S. *Electron transport and Scanning Gate Microscopy studies on ballistic hybrid SNS junctions* MA thesis (University of Pisa, 2014).

118. N. H. Balshaw, Practical Cryogenics, Oxford Instruments, 2001.

119. Zhang, L. *et al.* Fabrication and characterization of InSb nanosheet/hBN/-graphite heterostructure devices. *Nanotechnology* **33.** https://iopscience.iop.org/article/10.1088/1361-6528/ac6c34 (2022).

120. Van Weperen, I. *et al.* Spin-orbit interaction in InSb nanowires. *Phys. Rev. B* **91,** 201413. https://link.aps.org/doi/10.1103/PhysRevB.91.201413 (2015).

121. Hikami, S., Larkin, A. I. & Nagaoka, Y. Spin-Orbit Interaction and Magnetoresistance in the Two Dimensional Random System. *Progress of Theoretical Physics* **63,** 707–710. https://doi.org/10.1143/PTP.63.707 (1980).

122. Iorio, A. *et al.* Vectorial Control of the Spin–Orbit Interaction in Suspended InAs Nanowires. *Nano Letters* **19,** 652–657. https://doi.org/10.1021/acs.nanolett.8b02828 (2019).

123. Turini, B. *Josephson Diode Effectin High-Mobility InSb Nanoflags* MA thesis (University of Pisa, 2022).

124. Maxfield, B. W. & McLean, W. L. Superconducting Penetration Depth of Niobium. *Phys. Rev.* **139,** A1515–A1522. https://link.aps.org/doi/10.1103/PhysRev.139.A1515 (1965).

125. Heida, J. P. *et al.* Nonlocal supercurrent in mesoscopic Josephson junctions. *Phys. Rev. B* **57,** R5618–R5621. https://link.aps.org/doi/10.1103/PhysRevB.57.R5618 (10 1998).

126. Bleszynski, A. C. *et al.* Scanned Probe Imaging of Quantum Dots inside InAs Nanowires. *Nano Letters* **7,** 2559–2562. https://doi.org/10.1021/nl0621037 (2007).

127. Grabert, H., Devoret, M. H. & Kastner, M. A. Single Charge Tunneling: Coulomb Blockade Phenomena in Nanostructures. *Physics Today* **46,** 62–63. https://api.semanticscholar.org/CorpusID:120624836 (1993).

128. Pankratova, N. *et al.* Multiterminal Josephson Effect. *Phys. Rev. X* **10,** 031051. https://link.aps.org/doi/10.1103/PhysRevX.10.031051 (3 2020).